Tidal Influence on the Fraser River Plume

by

Shumin Li

B.Sc., Xiamen University, 2019

A THESIS SUBMITTED IN PARTIAL FULFILLMENT OF
THE REQUIREMENTS FOR THE DEGREE OF

MASTER OF SCIENCE

in

The Faculty of Graduate and Postdoctral Studies

(Oceanography)

THE UNIVERSITY OF BRITISH COLUMBIA

(Vancouver)

April 2022

The following individuals certify that they have read, and recommend to the Faculty of Graduate and Postdoctoral Studies for acceptance, the thesis entitled:

Tidal Influence on the Fraser River Plume

submitted by **Shumin Li** in partial fulfillment of the requirements for the degree of **Master of Science** in **Oceanography**.

Examining Committee:
Rich Pawlowicz, Professor, Earth, Ocean and Atmospheric Sciences, UBC
Supervisor
Susan Allen, Professor, Earth, Ocean and Atmospheric Sciences, UBC
Supervisory Committee Member
Phil Austin, Associate Professor, Earth, Ocean and Atmospheric Sciences, UBC
Additional Examiner

Abstract

The Fraser River plume in the Strait of Georgia, BC, is significantly influenced by the tide. Here we use 17 years of daily MODIS observations of suspended particulate matter to understand the tidal variability of the plume. Our results show a consistent negative correlation between the Fraser River plume area and the tidal elevation with a phase lag at about one hour from two independent methods. The plume area routinely increases/decreases by about 20% during the ebb/flood tides, and a lower river flowrate typically leads to a more dramatic tidal variation in the plume area. A tidal harmonic analysis is performed on the HF-radar derived surface currents, and the difference between the extents of diurnally and semi-diurnally driven river influence suggests two distinct dynamical regions in the horizontal plume structure. A simple analytical model based on the volume conservation and salinity balance equations is built to analyze the mechanism of the tidal variability in the plume size. The observed tidal patterns of the plume area variation are partly reproduced using tidally modulated plume salinity (observed from instrumented ferries) and river flowrate (from numerical model outputs). These new findings will improve our understanding of the short-term dynamics of the Fraser River plume.

Lay Summary

River plumes are the light and fresh water mass coming from a river and floating on the ocean. They usually carry a great mount of silt and sediments which makes them to stand out in satellite pictures. In this study, satellite images taken above the Strait of Georgia for the past 17 years are examined to investigate how the tide influences the Fraser River plume size. Our results show that the plume area decreases by about 20% as the water level rises up (flood tides) in the Strait, and increases about the same amount as water level goes down (ebb tides). This tide-plume correspondence mainly comes from a tidal variation on the freshwater input at the Fraser mouth, which pushes more water into the plume during ebb tides, and less water into the plume during flood tides.

Preface

This thesis is original, unpublished, independent work by the author, S. Li, with the advice of his supervisor, R. Pawlowicz, who will be a co-author of a journal article published out of this study. The SPM images used for this thesis are downloaded and pre-processed using the SeaDas software (Sec. 2.1) by research assistant K. Stankov, and all the further image processing procedures (Sec. 2.2) are done by the author. Fig. 1.1 is used with permission from A. Horner-Devine, and Fig. 2.1 is used with permission from R. Pawlowicz.

Table of Contents

List of Tables

List of Figures

List of Symbols

A: Plume area

D: Plume depth at the Fraser River mouth (deepest plume depth)

$\bar{D}$: Average plume depth

D_{T}: Time derivative of tidal elevation at Pt. Atkinson

F_{f}: The rate of plume water loss at its front.

k: Entrainment coefficient

S_{w}: Surface SPM concentration

Q: River flowrate[1]

R: Correlation coefficient

R_{AF}: Normalized plume area, defined as the ratio of satellite observed plume area to the area estimated by the linear regression to the river flowrate.

R_{C}: Percentage of plume area change per hour between same-day image pairs.

r^2: Coefficient of determination (R squared)

r_{rs}: Water-leaving reflectance

$S_{\mathrm{e}}w_{\mathrm{e}}$: salt flux at the bottom of the plume

S_{f}: Ferry-measured plume salinity

S_{max}: Maximum salinity along a ferry track

S_{min}: Minimum salinity along a ferry track

S_{o}: Ambient ocean salinity

S_{offset}: Salinity offset

S_{p}: Overall plume salinity

S_{ref}: Reference salinity

[1] In this thesis, adding (t) after a parameter (e.g., $Q(t)$) refers to the hourly or minute-by-minute-resolution ("minutely") variation of this parameter, in which tidal variability is important. When an overline bar is added on top of a parameter (e.g., $\bar{Q}$), it refers to the daily average of this parameter. In this case, it may still show seasonal variations, but no tidal variation is considered. If not particularly specified (e.g., Q), it can refer to either tidal or subtidal variations, or it means that tide is irrelevant. The same notation is applied to other parameters, e.g., A, $w_{\mathrm{e}}A$, S_{p}, S_{o} ...

ST_{abs}: Absolute salinity threshold

ST_{rel}: Relative salinity threshold

$\mathbf{U}$: Surface velocity

$|\mathbf{U}|$: Depth-averaged surface velocity

w_{e}: Upward entrainment velocity

$w_{\text{e}}A$: Rate of upward entrainment at the bottom of the plume

$\frac{dS_{\text{f}}}{dt}$: Time derivative of ferry-measured plume salinity

$\frac{dS_{\text{p}}}{dt}$: Time derivative of overall plume salinity

γ: Correction factor to adjust S_{f} for S_{p}

η: Tidal elevation at Pt. Atkinson

ρ_{w}: Subsurface reflectance

List of Abbreviations

BC: British Columbia
CODAR: Brand name for HF radar systems sold by CODAR Ocean Sensors (Mountain View, California)
CTD: An oceanography instrument used to measure the electrical conductivity, temperature, and pressure of seawater
FVCOM: Unstructured Grid Finite Volume Community Ocean Mode
HF-radar: High-frequency radar
l.f.s: left hand side
MODIS: Moderate Resolution Imaging Spectroradiometer
M/V: Motor vessel
NW: Northwesterly (wind)
ONC: Ocean Networks Canada
PST: Pacific Standard Time
Pt. Atkinson: Point Atkinson
RMSE: Root mean square error
ROFI: Region of freshwater influence
r.h.s: right hand side
SE: Southeasterly (wind)
SoG: Strait of Georgia
SPM: Suspended particulate matter

Acknowledgements

I would first like to express my greatest gratitude to my supervisor, Professor Rich Pawlowicz, thank you for your time, patience, and support throughout my master's journey. You witnessed every single step of my progress in research, and provided me with tremendous help and encouragements. It is an honour of my life to be a student of yours.

I would like to thank my committee member, Professor Susan Allen, for your time, enthusiasm, and helpful suggestions throughout my whole master program. Thank you to Professor Phil Austin for examining my thesis and providing resource for future applications of my work. I would also like to thank Metro Vancouver for funding my master's research.

At last, I would like to thank all my friends in UBC EOAS, I am truly lucky to have you all in my life. Thank you for all the good time we share - Connor Henderson, Ed Mason, Nicole McEwan, Sam Stevens, Becca Beutel, Birgit Rogalla, and Yuanji Sun.

Chapter 1

Introduction

River plumes are critical links between the land and ocean, and are important to the coastal environment and local productivity. They are highly dynamic, and their variability depends on multiple intrinsic and extrinsic factors. Among these factors, the high-frequency dependencies (i.e., tidal influence) of the river plumes are important components of the plume dynamics, but they are less understood because of the lack of good observations with sufficient temporal and spatial resolution. This thesis is aimed at addressing this problem, by providing an in-depth analysis on the tidal influence on the Fraser River plume.

The first chapter of this thesis starts with an overview of background knowledge about river plumes, including their definition, importance, basic structures, and dependencies. Then, local environmental settings of the Fraser River and the Strait of Georgia are introduced, with a summary of earlier findings about the Fraser River plume variation under different wind, tide, and river discharge conditions. Important characteristics of the tide in the Strait are described in the third part of this chapter, in particular, tidal patterns in daily, fortnightly, seasonal and decadal cycles are thoroughly discussed. Last, the study objectives are proposed and a series of research questions are listed.

1.1 River Plumes

A river plume, or a region of freshwater influence (ROFI), is the name given to the buoyant water mass discharged from a river into the coastal ocean. Although the exact definition of these terms may vary slightly as used by different researchers (and in different stages of their studies), it is commonly agreed that the river plumes can be highly dynamic, time dependent, and have critical impact on the coastal ecosystem (e.g., Chant, 2012; Warrick and Farnsworth, 2017; Hetland and Hsu, 2013; Horner-Devine, 2009; Hetland, 2005). Major river plumes usually carry a great amount of terrigenous sediments and anthropogenic nutrients, which makes them a significant carbon source to some coastal

oceans, contribute one-half of all oceanic carbon burial, and dominate the local productivity and environmental quality (Fennel et al., 2011; Hetland and Hsu, 2013; Hetland, 2005; Hedges and Keil, 1995). For example, a large hypoxic area (or called "dead zone") is found underneath the Mississippi River plume, where the bottom oxygen is consumed by the decomposing organics while the vertical ventilation is prevented by the strong stratification (Rabalais et al., 2002), and toxic dinoflagellate bloom events are found to be associated with the variation of Kennebec River plume in the Gulf of Maine (Franks and Anderson, 1992).

Other than being a critical link between terrestrial and coastal ecosystems, river plumes also play an important role in social and economic activities. For example, they are habitats for many commercial fisheries (Able et al., 1998), provide open water for tourism and recreation (Chant, 2012), serve as pathways for commercial container ships and passenger cruises, and support oil drilling platforms. Because of their importance in ecosystem maintenance and social activities, a good understanding of the behaviour and variation of river plumes is crucial to the welfare of marine environment and economic production.

However, it is not easy to fully understand the dynamics of river plumes. Their dynamics can be fully non-linear and strongly influenced by multiple factors, such as tide, wind, river discharge, ambient currents, coastal bathymetry, earth's rotation, and internal waves (Chant, 2012; Horner-Devine et al., 2015; O'Donnell, 2010; Hetland and Hsu, 2013; Warrick and Farnsworth, 2017). In the past decades, hundreds of research papers have been dedicated to explore the dependence of river plumes worldwide on these intrinsic and extrinsic factors through analytical solutions (e.g., Yankovsky and Chapman, 1997; Garvine, 1995), observational approaches (e.g., Chen et al., 2017; Warrick et al., 2007; Kastner et al., 2018; Warrick and Farnsworth, 2017), and numerical models (e.g., Chen, 2014; Hetland, 2005; Schiller et al., 2011; Li and Rong, 2012).

Although the size, shape and variability of different plume systems are not identical, their horizontal structures can usually be described as being composed of three dynamical regions: a jet-like near-field plume, a recirculating mid-field plume (bulge), and an alongshore directed far-field plume (see Fig. 1.1) (Chant, 2012; Horner-Devine et al., 2015; Hetland and Hsu, 2013; O'Donnell, 2010). Each of these have very different characteristics.

The near-field plume is generally considered as the region where the river water shoots out into the ocean with a speed higher than the intrinsic internal wave propagation speed (Hetland and Hsu, 2013), which usually triggers shear instabilities and vertical mixing. In some studies, e.g., Horner-Devine et al. (2009), a near-field plume is also referred to as a

tidal plume, because it can be greatly affected by tide. A tidal pumping mechanism was first proposed by Stommel and Farmer (1952), in which the plume under ebb tide is viewed as a jet with a near rectangular shape while the flood tide draws water back to the estuary from a semi-circular region in the coastal ocean. The asymmetry of this estuarine outflow suggests a potential pair of "dipole eddies" at the river mouth, and an enhanced exchange rate between the estuary and coastal ocean. Another important mechanism in this region is related to the initial radial spreading of the plume as it empties into the coastal ocean, which increases shear instabilities and also increases the area over which mixing occurs (Horner-Devine et al., 2015).

As the inertial momentum from the near-field plume starts to dissipate, a transitional region of recirculating water may occur. This recirculating bulge, or mid-field plume, is often found in numerical models (e.g., Chen, 2014; Hetland, 2005; Nehama and Reason, 2015) but has only been observed in the real ocean in a few recent studies under sufficiently low winds and small ambient currents (e.g., Chen, 2014). When present, the mid-field bulge can grow continuously in time and accumulate between 25 % and 75 % of the freshwater discharge in about 7 days and cause a corresponding reduction in the transport of plume water to form coastal currents (Fong and Geyer, 2002). However, as wind stress and ambient currents become stronger, the bulge formation will be significantly disrupted.

The third major dynamical region is the far-field plume. It is the region beyond the mid-field in which the plume no longer has the initial momentum of the river discharge. Earth's rotation, buoyancy, wind stress, and sometimes bottom stress are the primarily governing forces (Horner-Devine et al., 2015). The far-field plume may extend hundreds of kilometers from the river mouth and form a geostrophic coastal current that transports the diluted river water to the right side of the estuary in the northern hemisphere and left side in the southern hemisphere (Fig. 1.1). The structures, dynamics and propagation speed of this coastal current are determined by the shelf slope and whether or not it is attached to the bottom (Yankovsky and Chapman, 1997).

This prototypical plume structure consisting of three dynamical regions is well studied and widely recognised, however, it is important to note that the exact shape and dynamics of a river plume is not steady, and it can vary significantly throughout time by wind, tide and river discharge. For example, the Delaware River plume is bottom attached (far-field plume being predominant) mostly through the year, but in the spring, when the river discharge greatly increases, it can form a surface advected plume (all dynamical regions are present) at the peak river discharge (Münchow and Garvine, 1993). Coastal upwelling and

downwelling winds can completely reshape the plume and significantly influence the mixing and dynamics in mid-field and far-field regions (Horner-Devine et al., 2009; Warrick and Farnsworth, 2017; Hetland, 2005; Gan et al., 2009; Fofonova et al., 2015). More importantly for this thesis, tide can significantly impact the momentum balance, internal friction and stratification in the near-field plume (McCabe et al., 2009). Fortnightly spring/neap cycles in the salinity stratification and vertical stability are also found in a few river plume systems (e.g., Simpson, 1997).

However, investigations into the role of tide in the dynamics of coastal plumes has mostly focused on the mixing and entrainment of plume water into sea water in numerical simulations (e.g., Chen, 2014; Fofonova et al., 2015) and short-term observational studies (e.g., Horner-Devine et al., 2009). For example, in Rijnsburger et al. (2018); Kilcher and Nash (2010), X-band radar images are used to investigate the influence of tide on the propagation of river plume fronts. Similarly in Kastner et al. (2018), a drifter-based observational study is used to characterize the spreading and mixing of the Fraser River plume under ebbing tides in winter. These short-term studies nicely observed the tidal evolution of a plume system at the studied time, but the question of the adaptability of their conclusions to other times still remains.

For a longer period of time, observations of plumes usually rely on moorings (e.g., Simpson, 1997) or instrumented ferry tracks (e.g., Halverson and Pawlowicz, 2008, 2011), which only focus on a small portion of the plume. These observations are good at providing consistent records of the some plume properties at a high temporal resolution, but they don't treat the plume body as a whole and they can't directly describe how the plume develops in structure and shape.

To fully understand the tidal impacts on a plume system, temporal and spatial coverage of the observations are equally important. This requirement is particularly true in the case of the Fraser River, which is known anecdotally to have very strong tidal and seasonal variations.

1.2 Strait of Georgia and Fraser River Plume

The Fraser River is the second largest river by discharge on the west coast of North America (Pawlowicz et al., 2017). It drains an area over 230, 000 km^2 in the southeast Canada (Kastner et al., 2018) and flows into the Strait of Georgia (hereafter SoG or "the Strait"). The Strait of Georgia is a semi-enclosed, fjord-like coastal basin between mainland British

Columbia and Vancouver Island (Fig. 1.2). It connects to the Pacific Ocean through Juan de Fuca Strait in the south and through several narrow but relatively long channels in the north. Overall, the Strait is about 220 km long (NW to SE) and 30 km wide, with an averaged depth of about 150 m and a maximum depth of 420 m (Thomson, 1981). In the vicinity of the plume, the Strait is 100-300 m deep (Fig. 1.2).

Before entering the southern Strait, the Fraser River splits into 4 channels, namely the Main Arm (receiving about 75% to 87% of total discharge), the North Arm (carrying most of the remainder) and two other small channels (Crean et al., 1988; Thomson, 1981). The Main Arm is the deepest and widest channel, which extends 9 km offshore from Steveston to Sand Heads Lightstation through a region of mudflats (Fig. 1.2). Since these shallow mudflats are partially uncovered during low tide, Sand Heads is sometimes considered as the mouth of Fraser River (e.g., in Pawlowicz et al., 2017).

As the Fraser River enters the SoG, the buoyant freshwater detaches from the river channel and bottom, and forms the Fraser River plume. This fresh and turbid water mass is found to have an averaged area of 450 km^2(Pawlowicz et al., 2017) and can span across the Strait to its southwest boundary under certain conditions (Halverson and Pawlowicz, 2011; Pawlowicz et al., 2017). The plume water contributes 65% to 85% of the particulate matter (Johannessen et al., 2003) and 65% of the fresh water (Halverson et al., 2017) to the Strait, which consequently affects the local light attenuation, contaminant dispersion and primary productivity (Pawlowicz et al., 2017).

Because of the topography surrounding of the Strait, local winds are usually found to be either southeasterly or northwesterly. These along-shore winds have a significant impact on the plume location and shape. For example, Pawlowicz et al. (2017) show that, under high river flowrates, the Fraser River plume has a northern boundary near Sand Heads and a southern boundary all the way towards Georgina Point under strong NW winds. However, under strong SE winds, the southern boundary of the plume can barely reach south of Tsawwassen Ferry Terminal and its northern boundary can extend far deeper into the Strait. Although the wind speed and direction are found to be almost completely uncorrelated with the overall plume area by Pawlowicz et al. (2017), the mixing, spreading and thickness of the plume during ebbing tides can be affect by NW/SE winds under low river flow conditions (Kastner et al., 2018).

Another important factor controlling plume variation comes from the seasonal cycle of the Fraser River discharge. Free from any dams along its path, the Fraser River discharge is a pure reflection of the local weather and seasonal forcing (Halverson and Pawlowicz,

2011). It usually has a freshet flow peaking in June ($\sim$ 10,000 m^3 s^{-1}) and a typically low runoff in fall and winter ($\sim$ 1,000 m^3 s^{-1}) with occasional flow pulses after storms (Fig. 1.3). The plume size is then found to be linearly correlated with the river flowrate (Pawlowicz et al., 2017), changing by a factor of 10 between winter and summer. Plume salinity decreases quasi-linearly with the increasing river discharge at 1.4 psu per 1000 m^3 s^{-1}, however, the plume freshwater residence time[2] is found to be about 1 day, and the flushing time[3] is found to be around 2.2 days, both of which are nearly independent of river discharge (Halverson and Pawlowicz, 2011).

However, the role of tide in the variation of Fraser River plume is less known. Although freshwater flux at the lower Fraser mouth and the plume salinities are shown to be tidally modulated through earlier investigations from measurements on regular ferry transects (Halverson and Pawlowicz, 2008), no apparent correlation between plume area and tidal height was found by Pawlowicz et al. (2017). In theory, as freshwater pulses into the Strait during ebbing tides, the plume area is expected to expand to accommodate this inflow of water. However, a subset of satellite observation with a temporal resolution of about one image every five days (i.e., in Pawlowicz et al., 2017) makes it difficult to exhibit this plume variation in a few hours. In addition, as shown later in this thesis, the coincidence of linked seasonal cycles of river discharge, cloud coverage and the phase of tide results in a hidden bias in the satellite images (that are captured at about a fixed time in a day), and this bias adds an extra layer of difficulty in showing the tide-plume correlation. To reveal this subtle impact of tide on the Fraser River plume, a deeper understanding in the nature of tide in the Strait is needed.

1.3 Tide in the Strait

The tide progresses as a wave northwestwards along the coastline of the northeastern Pacific (Thomson, 1981). As this waves enters the SoG, the raised water is reflected from the northern end of the channel. This southward reflected portion of tidal wave is then combined with the inward portion of the tide to produce a standing wave in the Strait (Thomson, 1981). Thus, unlike a typical coastal Kelvin wave, the entire water level in the Strait moves up and down almost simultaneously with a maximum outflow tidal current at

[2] the average time it takes for a water parcel to exit a system

[3] similar to residence time, but based on a simple bulk estimation of salinity balance between plume and non-plume waters

the mid-point of an ebbing tide. Because of this concurrent tidal behaviour, the difference in time between identical stages of tide almost never exceeds 30 minutes between any two places within the Strait (Thomson, 1981)[4]. Thus, it is safe to use the tidal elevation at one representative location to show the stage of tide for the whole Strait[5].

In this thesis, following earlier studies (e.g., Halverson and Pawlowicz, 2011; Pawlowicz et al., 2017), tidal elevation are derived at Point Atkinson to represent the stage of tide for the Fraser River plume. Point Atkinson is located 25 km north of Fraser mouth (Fig. 1.2), which is not affected by the river stage (Halverson and Pawlowicz, 2008, 2016; Halverson et al., 2017). What's more, the tidal record at Point Atkinson is more than 100 years long. Based on this well-maintained historical data, the tidal predictions from this site are usually considered to be the most reliable.

Tides observed at Pt. Atkinson are mixed semi-diurnal. In a common daily tidal cycle of about 24 h 50 min, two high tides and two low tides are expected (Fig. 1.4a). In order to describe the time of these maximum/minimum tidal elevation, the relative time after the minimum sea level (lower-low tide) of the day is defined as tide lag hours (h). Then, these elevation peaks are named correspondingly as lower-high (h $\sim$ -7), lower-low (h = 0), higher-high (h $\sim$ 7) and higher-low (h $\sim$ 13) tides (Fig. 1.4a). The most dramatic elevation change of the day is usually found around the lower-low tide between h = -7 to h = 7, which refers to the big ebb followed by the big flood (namely the "big ebb" cycle hereafter). For the other half of the daily cycle, tidal variation is relatively small, and is thus named the "small ebb" cycle.

In a fortnightly cycle (about 14.8 days), the daily tidal range routinely increases and decreases (Fig. 1.4b). When the daily tidal range is over 3.25 m or the lower-low tide is below 1.22 m, it is considered to be a spring tide, otherwise it is under a neap tide[6]. During spring tides, there is a strong diurnal pattern of a dominant "big ebb" followed by a weak "small ebb". While in the neap tide periods, tidal signals are more semi-diurnal and the difference between daily "big ebb" and "small ebb" is much smaller.

The time in the day when the daily lower-low tide occurs is not random, instead, it

[4]except that the tide gets quite delayed going up the Fraser

[5]excluding the Fraser River channels

[6]spring/neap usually refers to tidal effects arising from the alignment of the sun and moon. However, the largest fortnightly effects in the SoG arise from the height of the moon above the equator, which means that it is (in a precise term) a "tropic/equatorial" cycle. Although in this thesis, we still use the term "spring/neap" as a representative of the bi-weekly tidal variation of the "bigger/smaller" daily elevation range, readers should be aware that this term only refers to the stages in a fortnightly cycle rather than implying the relative position of the sun, earth and moon.

follows a unique pattern with a seasonal cycle (Fig. 1.5). For example, daily lower-lows in January are usually around midnight (20:00 to 2:00) while in June are usually in the middle of the day (8:00 to 14:00). In a year, all daily low tides are distributed inside a diagonally aligned "band" in Fig. 1.5a, which contains about 2 dozen "strings" which run across the band. Each "string" contains 13 to 15 "points" of daily lows, which form a fortnightly cycle (Fig. 1.5a).

Starting with each string (fortnightly cycle), the daily low tide occurs about 38 to 52 minutes later than the day before. Within each string, the daily lows always start with a relatively higher elevation (red dots in Fig. 1.5), gradually go lower (green and blue dots) and then increase again. This pattern indicates that a fortnightly cycle usually starts from neap tide, gradually develops into spring tide and goes back again.

The neap-spring-neap pattern in each fortnightly cycle is always observable, but the elevation of the daily lows in spring tides are quite different in different months of the year. For examples, daily low tides with an elevation below 0.5 m (blue dots in Fig. 1.5) can only be found around noon in summer and around midnight in winter. In spring and fall, such as March and September, the spring tides are never as strong as their winter/summer counterparts. Also, in April and May, spring tide appears early in the fortnightly cycle, while in August it shows up much later, near the end of the cycle.

Over a decadal scale, the seasonal shift of daily tidal phase still holds. Inter-annual variation of the tidal cycle is found to be small, which means that tidal patterns and seasonal variations can be applied to multiple years. Thus, it is safe to use multiple years data of observation without worrying too much about the potential inter-annual variability.

Not only does the tide vary in rather predictable ways, but it's likely that it will also affect the plume in predictable ways that are not random from day to day, but rather are highly structured in time. Understanding the seasonal cycle of the tidal phase shift is then also very important to understand the inherent bias from satellite observations, which often occur at fixed times of the day. For example, since the optical images from these space based instruments can only be captured during day time, all summer images are then taken within the "big ebb" cycles of the day while all winter images are fallen into the "small tide" periods. Because the river discharge is usually high in summer and low in winter, satellite observed tidal features around the "big ebb" are then "falsely enhanced" by the summer freshet. More details of this bias and the corrections applied will be further discussed in Sec. 3.2 and 3.3.

1.4 Study Objective and Research Questions

Fraser River plume is important to the local environment and ecosystem in the Strait of Georgia. However, the dynamics, especially tidal forcing of this buoyant plume are not fully understood. This study aims to reveal the tidal influence on the Fraser River plume. Specifically, this study aims to answer the following research questions:

1. What is the relationship between tidal elevation and the Fraser River plume area in the Strait of Georgia?
2. How does the plume reshape and relocate with a short period of time under flooding/ebbing tides?
3. What is the general pattern of the Fraser River plume during a tidal day?
4. Is the correlation between tide and plume area the same under different river discharge conditions?
5. What is the mechanism of the plume area variation through a tidal cycle?

To answer these questions, a 17-year satellite data set of the concentration of suspended particulate matters in the Strait of Georgia is carefully examined. Correlations between the tidal stage and the plume area are established, and the mechanism behind this tidal modulation is investigated. In the following Data and Methods chapter, introduction will be made to the primary dataset (satellite imagery) and other supplementary datasets. The image processing procedure will also be described in detail. The next two chapters will be focused on the observational results of the tidal variations on multiple aspects of the plume, and a simple quasi-analytical diagnostic model that is constructed to reproduce the tidal variability in the observations. In addition, the consistency of this tide-plume correlation will be examined under different river discharge conditions, and the mechanism of this correlation will be investigated by linking to the tidal cycle of the freshwater input at the river mouth and the tidal variation in the plume salinity. The implication of the results to the upward entrainment at the bottom of the plume will be discussed in detail.

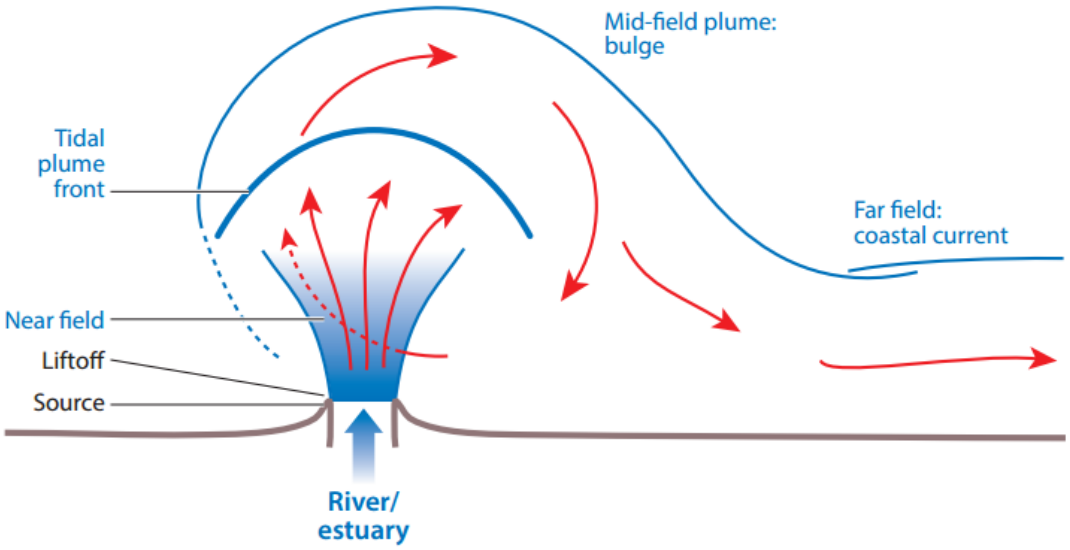

Figure 1.1: Schematic representation of the prototypical plume comprising all dynamical regions. Fig. 2 from Horner-Devine et al. (2015). Reproduced with permission of A. Horner-Devine.

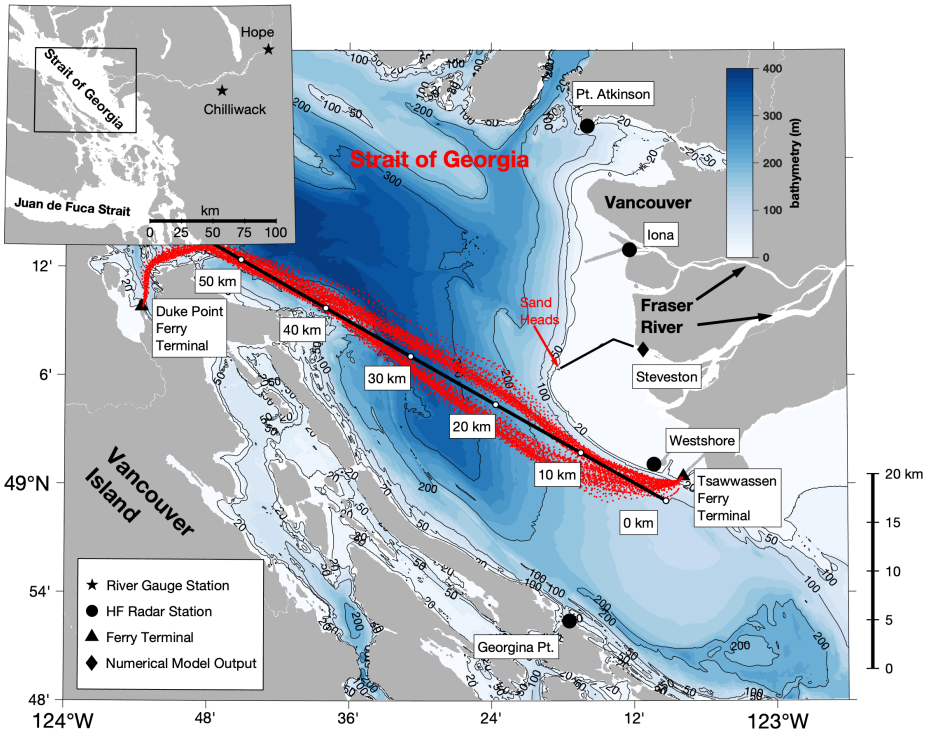

Figure 1.2: The geographical map of the Strait of Georgia and Fraser River.

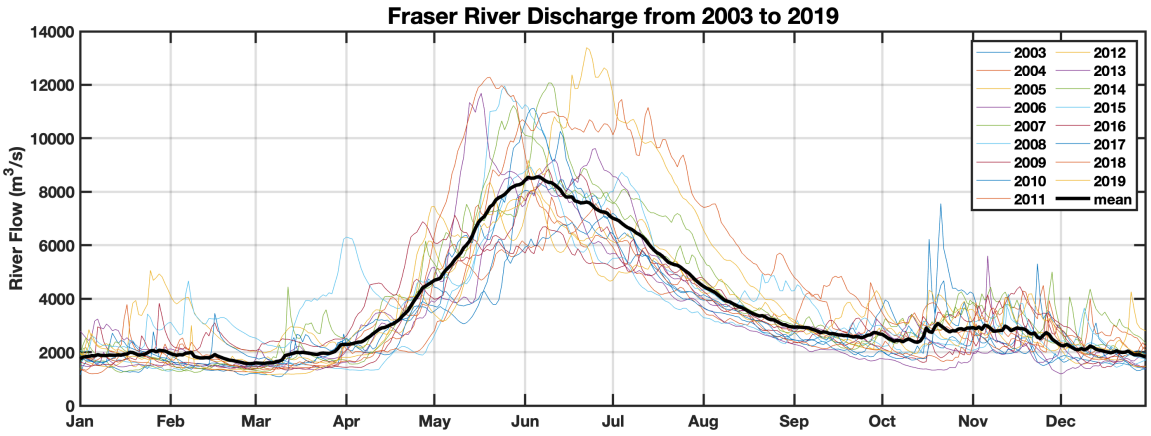

Figure 1.3: Calculated Fraser River discharge from gauge station at Hope and Chilliwack, 2003 - 2019. Thick black curve shows the averaged daily river flowrate.

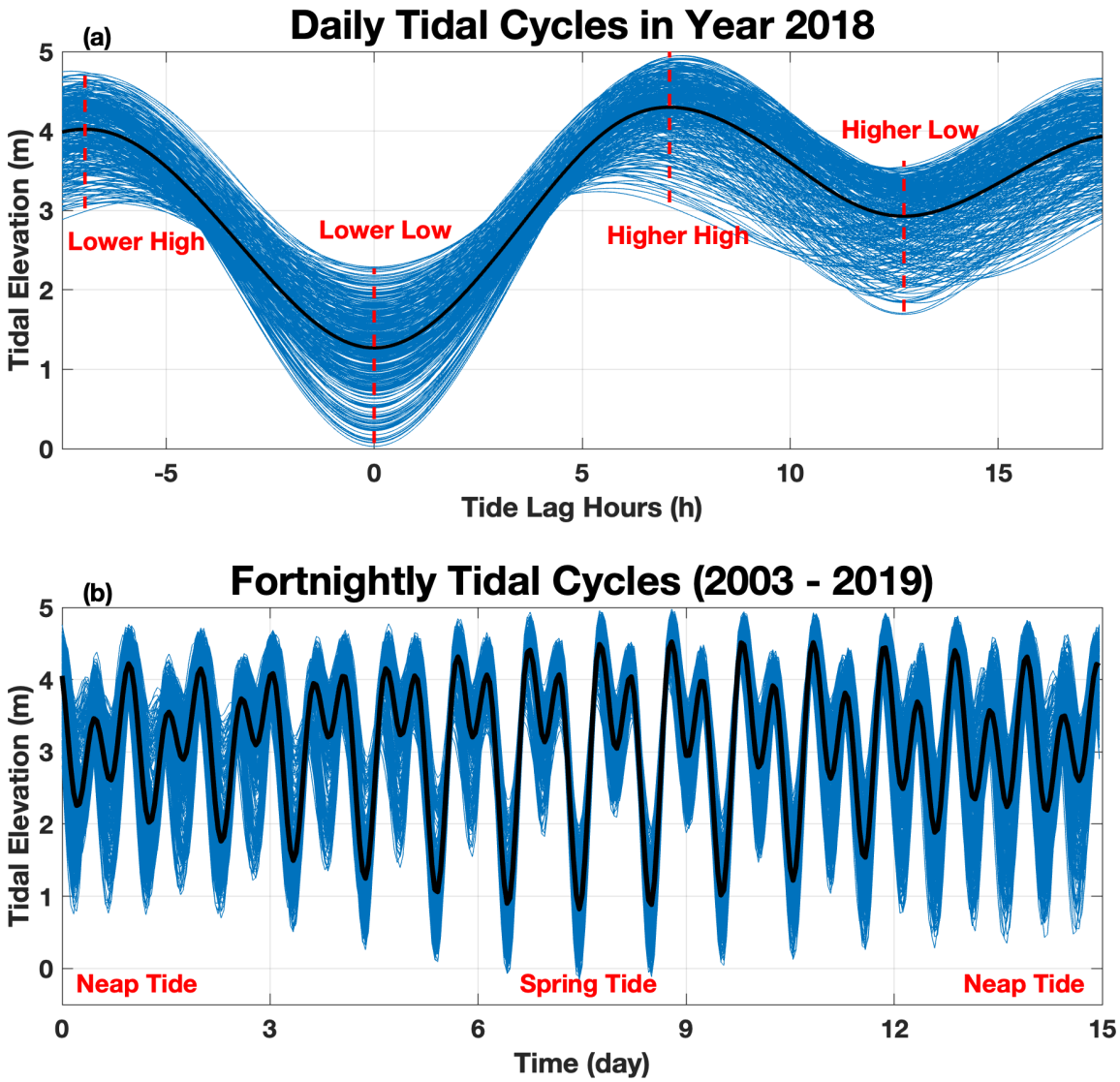

Figure 1.4: (a) Daily tidal cycle pattern at Point Atkinson, with h = 0 to be the lower-low tide of the day. Blue curves are the tidal elevation predicted for each day in 2018, aligned by the time of lower-low tide, while the thick black curve shows the mean value of all blue curves (b) Fortnightly tidal pattern for years 2003 to 2019, the lowest elevation in each cycle is aligned at day 7.5.

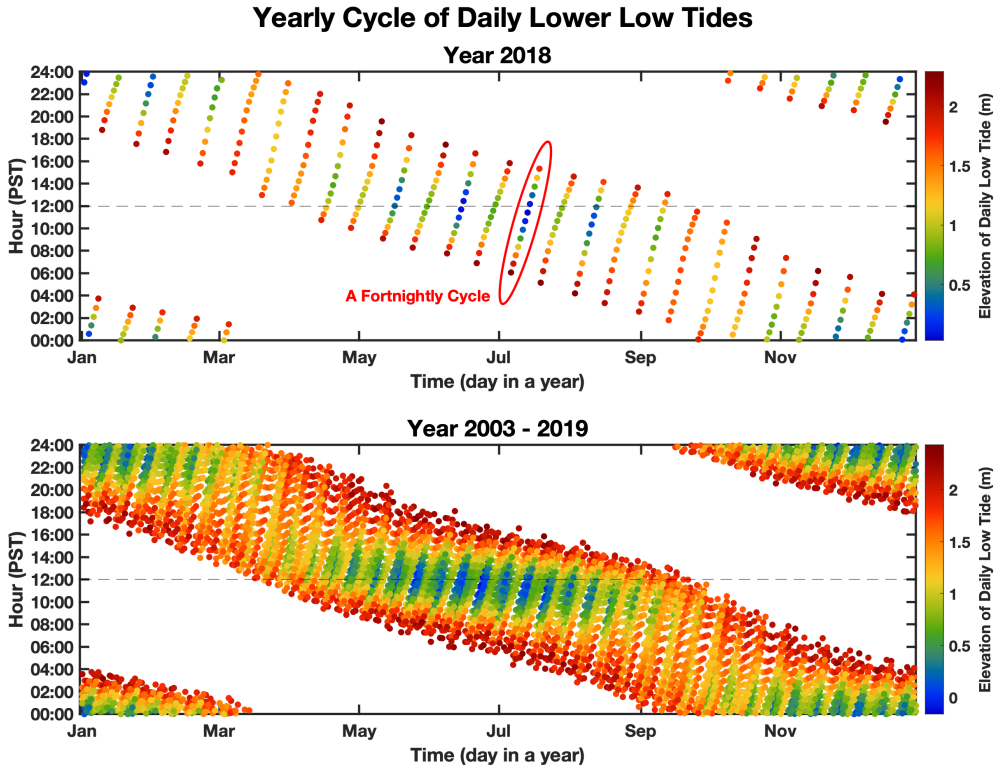

Figure 1.5: Distribution of the low-tide time in a day throughout the year. Horizontal axis shows the time in the year when each daily low tide occurs, while the vertical axis shows its time in a day in PST. The corresponding elevation of the low tide is coloured. Upper panel only shows data from one year (2018) while the lower panel plots data over 17 years (2003 - 2019).

Chapter 2

Data and Methods

In the first part of this chapter, the primary dataset used for this study is described. The primary dataset is derived from satellite imagery, but using this source of daily data to investigate tidal variations of the Fraser River plume requires some care. In the second part of this chapter, the processing and evaluation aspects of this dataset are considered at length. In addition to this satellite imagery, some supplementary datasets are helpful to understand the environment settings of the plume. In the third part of this chapter, these supplementary datasets are introduced and described.

2.1 Satellite Imagery of Suspended Particulate Matter (SPM)

The primary dataset used for this thesis consists of high-resolution ($\sim$ 250 m) images from the Moderate Resolution Imaging Spectroradiometer (MODIS) instruments onboard the Aqua and Terra spacecrafts. With a wide swath ($\sim$ 2330 km) and broad spectral range (36 spectral bands ranging in wavelength from 0.4 μm to 14.4 μm), MODIS has been used to provide high quality surface observation images of Earth's land, ocean and atmosphere for the past two decades (Khlopenkov and Trishchenko, 2008). From year 2003 to 2019, over 10,000 such images covering the southern Strait of Georgia region are available for examination.

With a higher concentration of suspended sediments against the rest of the Strait, Fraser River plume is usually clearly visible in these MODIS images (e.g., Fig. 2.1a). However, it is difficult to define the boundary of the plume region based on true-colour images. Instead, further processing of these images is required to perform quantitative analysis. Commonly, information from band 1 (wavelengths of 620-670 nm, centred at 645 nm) is used to assess suspended particulate matter (SPM) concentration (e.g., Chen et al. (2007); Doxaran et al. (2009); Lahet and Stramski (2010); Miller and McKee (2004); Petus

et al. (2010); Wang et al. (2009)).Then, a threshold of this concentration can be established to define the expanse of the plume (e.g., Pawlowicz et al., 2017).

The method for calculating SPM concentration is well-articulated in Pawlowicz et al. (2017). In short, first, the high-resolution 250 m L2 QKM files are generated from SeaDAS 6.4 software. Then, these L2 files are used to derive SPM concentration from band 1 reflectance. The subsurface reflectance ρ_{w} is first calculated from water-leaving reflectance r_{rs}:

$$\rho_{\mathrm{w}} = \pi R r_{\mathrm{rs}} \tag{2.1}$$

where R describes the effects of reflection and refraction by the surface (Morel and Gentili, 1996). Then, the surface SPM S_{w} (grams per cubic metre) can be estimated based on ρ_{w} according to the following semi-empirical relationship:

$$S_{\mathrm{w}} = \frac{A^{\rho}\rho_{\mathrm{w}}}{1 - \rho_{\mathrm{w}}/C^{\rho}} + B^{\rho} \tag{2.2}$$

where the parameters $A^{\rho} = 258.85$, $B^{\rho} = 0$ g m^{-3}, and $C^{\rho} = 0.1641$ are the coefficients specific to the MODIS high-resolution 645 nm channel, matching in situ calibration samples described in Nechad et al. (2010).

In order to prevent some inappropriately triggered cloud and sea-ice masks onto the centre of the plume close to the river mouth, a nominal threshold of 0.027 for cloud albedo was increased to 0.4 in SeaDAS processing. However, this threshold increase also results in abnormally high reflectances in regions of known low SPM concentration because of clouds or other bright targets.

In Pawlowicz et al. (2017), 904 images (about 70 images a year) were used for the analysis. However, to study the influence of a relatively high frequency oceanographical phenomena (i.e., tidal influence), temporal resolution of the dataset is very important. To increase the number of images available and to the improve temporal resolution, the following improvements are made to image selection procedures:

(1) Increase data time span

In this study, the time span of the satellite data was increased from 13 years (2003 - 2015 in Pawlowicz et al., 2017) to 17 years (2003 - 2019). The extra 4 years of data increased the number of images by 30 percent.

(2) Include images from Terra mission.

The Terra satellite was launched in December 1999, and it was designed to image the earth with its MODIS instrument on a descending orbit that crosses the equator at 10:30 am local time. The Aqua satellite was launched in May 2002, it carries an identical MODIS instrument but follows an ascending orbit that crosses the equator at 1:30 p.m.. Both spacecrafts are in orbits with a period of about 100 minutes, inclined at about 98°, and at an altitude of 705 km.

In Pawlowicz et al. (2017), only images from the Aqua mission were used to investigate the Fraser River plume variation. Ideally, including all Terra images would double the number of images available. However, the same processing applied to Terra images does not yield a comparable image set. After a careful examination of Terra images from January 2016 to January 2019, the number of usable images from Terra is found to be about 6 times smaller than that from Aqua.

The Terra images with the 250-m resolution at the 645 nm frequency are usually as good as those from Aqua, but some other bands in the 500-m resolution (e.g., 1240 nm, 1640 nm, and 2130 nm) miss significant coverage over the SoG. Some of these frequencies are crucial for the atmospheric corrections, and are therefore important for deriving correct SPM concentrations. The reason for this poor performance of Terra observation at these specific frequencies over the Strait is still unknown. It may relate to a tendency for an descending satellite (i.e., Terra) to suffer more sun-glint at the time when it passes over SoG (averaged at 11:22 a.m. in PST). Assuming that this poor quality of Terra observations of the Fraser River plume would also occur earlier than 2016, and considering the small number of extra images obtained from the intensive work of the individual image evaluation, no processing of Terra images was carried out for earlier years.

(3) Use of Same-day Image Pairs

As Aqua and Terra travel along their orbits, the on-board MODIS instrument circles the Earth 14 to 15 times a day with a fixed 2330 km swath. This design ensures that most of the Earth's surface can be monitored at least once a day, but also provides the possibility that two or more images may be created when a region is located inside the overlap of consecutive scan paths of the same satellite (which can happen at mid to high latitude regions). Because the orbital period of the satellite is about 100 minutes, the second image is usually 100 minutes later than the first one, which provides an opportunity to study the plume variation over a short period of time. The two-image-a-day feature, which is called same-day pairs in this study, is found nearly every other day in the Strait of Georgia (same-day pairs appear in 47.2 % of days). Within all 3300 same-day pairs found in the

17 years, 247 of which can be used to investigate the short-term plume variation. These same-day pairs were then carefully examined to reveal the plume variation feature under the tidal frequency (Sec. 3.4).

(4) Additional image processing: cleaning, interpolation, and image combining

After a visual examination of each single SPM image, it is found that at least one thousand flawed images actually contain useful information of the plume, and can be fixed by applying individual cleaning and interpolations. After including these previously discarded images, the number of images in our collection is increased to 2466. A step-by-step explanation of this additional image process is described in the following section.

2.2 Image Processing

In Pawlowicz et al. (2017), a manual evaluation of the image collection resulted in a set of 904 images over the 13 years of data used. As described above, multiple procedures were carried out to increase the number of images available. The dataset used here includes 2466 images over 17 years (although this number includes 247 days where 2 different images, spaced about 100 minutes apart). Detailed image processing procedure is described in the following sections.

2.2.1 Image Quality Indexing

Over 1500 previously discarded SPM images can actually be fixed with proper cleaning and interpolation. Also, even with the previously selected good images, some common problems still exist. First, some high reflected cloud patches are recognized as river plume, which needs to be removed (e.g., Fig. 2.2 c1, c4 and c5); second, some regions at the centre of the plume jet and near the coastline are inappropriately masked and need to be interpolated (e.g., Fig. 2.2c2, c3); third, high reflectance from other river plumes or mudflats (e.g., Squamish River plume, boundary bay mudflat, water channels among Gulf Islands) should be removed (e.g., Fig. 2.2b2, c4). To both include more images into the collection, and improve the image quality, the following procedures are applied.

In the first step, the 11,258 individual SPM images are visually examined, and are each assigned a quality index (0, 1, 2, or 3). The classification rubric is set up as follows:

0: To be discarded

Empty files, mostly cloudy images, or almost no useful information from these images. These images should be discarded (Fig. 2.2a1-a5).

1: Very good images

Almost no missing data in the plume region, plume boundary is clear. In other words, images given with index 1 can be used without further processing, or just need a mask to excluded data outside of Strait of Georgia. (Fig. 2.2 b1-b5)

2: To be processed

The plume area is recognizable, but with some common problems (Fig. 2.2c1-c5), which include (1) some gaps in the plume region or on the mudflat, (2) some abnormally high values outside of plume region (e.g., clouds) and some abnormally low values inside the plume.

3: Others

These images may show some features of the plume, but a significant portion is bad or missing. These images could still be used in determining the averaged plume structures under specific conditions, but the plume areas can not be easily calculated. (Fig. 2.2d1-d5)

After this visual inspection, 7677 (68.2%) images have index 0, 205 (1.8%) images have index 1, 2261 (20.1%) have index 2, and 1114 (9.9%) have index 3. Among all 11,258 images, 2466 (145 images per year) with index 1 and 2 can be used for this study.

2.2.2 Image Processing and Plume Area Calculation

In this step, all 2466 manually selected images with quality index 1 and 2 are further processed. The noise in the data are cleaned, and necessary interpolations are made to calculate the plume areas. For each image, the following steps are applied:

1. All negative and zero values in the image are deleted.
2. Masks are applied for the SoG, and data outside of the masks are deleted.
3. Approximate plume boundaries are manually drawn around the plume in each image, and abnormally high values (SPM > 2 g m^{-3}) outside of this contoured region are deleted.
4. Small contours inside the plume regions are manually drawn to delete abnormally low values (SPM < 2 g m^{-3} inside the plume.)
5. Missing data inside the contoured plume region (especially the near-shore regions over the mudflat) are interpolated.

6. Images of the SoG that are separated into different files along the flight track are combined. (e.g., Fig. 2.5)

Plume area is then calculated for each processed image. First, the number of image pixels are counted in which the SPM concentration is over 2 g m^{-3}, which is a threshold well-demonstrated in Pawlowicz et al. (2017) to identify the Fraser River plume boundary from MODIS SPM images. Then, the areas of these highlighted pixels are added to get the area of the plume.

In a common winter scenario (e.g., Fig. 2.3), clouds above the SoG are usually not properly masked, which results in an overestimation of the plume area. The individual plume mask that is applied to each image helps to reduce these cloud effects. On the other hand, in summer (e.g., Fig. 2.4), the high-reflectance plume centre is often mistakenly identified as clouds and is therefore inappropriately masked. The interpolation inside the plume region helps to solve the underestimation of plume area due to this reason.

Satellite data along a swath are broken up into files of a certain size, and sometimes the break between files happens over the Strait of Georgia. Combining these files helps to contribute about 40 images into the image collection (e.g., Fig. 2.5).

Following the same technique, 247 pairs of same-day images are processed as well. However, it is important to note that the plume area changes between these paired images are sensitive to the manually drawn plume boundary masks. Therefore, the same outer/inner plume masks are applied to both images in order to reduce the inconsistency in some special cases.

2.3 Supplementary Data

Some additional observation data and numerical model outputs were also used in this study. These data may serve to reveal the intrinsic bias of the selected image samples, validate and visualize the plume variation, and test the hypotheses made to explain the principle mechanism of the observed phenomena. A brief description of these supplementary data is in the following sections.

2.3.1 Fraser River Discharge

As discussed in Sec. 1.1,1.2 and 3.1, river discharge is one of the key factors that affects the size, structure and dynamics of a river plume. However, it is not easy to accurately

quantify the flowrate at the Fraser River mouth because of the strong tidal modulation and complex dynamics in the estuary. For a limited period of time between 1983 to 1993, Water Survey of Canada provided model outputs of daily river discharge for the gauging station at Port Mann (ID 08MH126), which is located 35 km upstream of the mouth and just before the river splits into different arms (Halverson and Pawlowicz, 2008). This historical record of Fraser River discharge is usually considered as the best representation of the freshwater flux in to the Strait.

Unfortunately, the daily discharge data from Port Mann is no longer available. The nearest active station monitoring the Fraser discharge is the gauging station at Hope (08MF005). Hope lies 120 km upstream of the mouth and it does not experience tidal fluctuations. However, unable to include a few important tributaries downstream, discharge at Hope is found to be about 17 % less than Port Mann in summer, and nearly 50 % less in winter (Pawlowicz et al., 2007). Especially after some high precipitation events (e.g., storms in the BC lower mainland in late falls and early winters), the majority of the Fraser discharge at the mouth may come from these downstream tributaries. In these cases, the Fraser River plume may quickly expand to be several times larger, while no significant increase in the flowrate at station Hope is observed.

In order to better estimate the river discharge at mouth, a few earlier studies attempted to estimate the flowrate at Port Mann by combining data from station Hope with some other stations downstream. For example, in Halverson and Pawlowicz (2008), a regression equation was established using data from gauging stations at Hope, Harrison River (08MG013) and Chehalis River (08MG001). However, in Pawlowicz et al. (2017), only the Chilliwach River gauge was used to account for downstream inflows. The regression in the second example is given by:

$$Q_{\text{Port Mann}} = Q_{\text{Hope}} + 5.61\ Q_{\text{Chilliwack}} + 481\ \text{m}^3\ \text{s}^{-1} \tag{2.3}$$

($r^2 = 0.97$, standard error $\pm$ 405 $\text{m}^3\ \text{s}^{-1}$, regressed to the historical Port Mann record) where an additional half-day delay was added to Chilliwack River record to account for runoff effects.

Since the Harrison River (used in Halverson and Pawlowicz (2008)) is no longer gauged, in this study, the method given in Pawlowicz et al. (2017) (i.e., Eq. (2.3)) is applied to estimated the river flowrate at the mouth using data from gauging stations at Hope and Chilliwack (available online from Water Survey of Canada at `https://wateroffice.ec.`

gc.ca/index_e.html). The seasonal pattern of river discharge based on this estimated Fraser flowrate at its mouth can be found in Fig. 1.3.

In addition to the daily river discharge, we are also interested in the hourly fluctuation of the Fraser flux, which helps to understand the tidal modulation of the freshwater supply to the plume. However, there is almost no observation of the hourly discharge along the Fraser River. Therefore, in this study, the results from a numerical model are used to represent the hourly variation of the flowrate at the Fraser mouth.

The model used here is obtained from a configuration of the Unstructured Grid Finite Volume Community Ocean Model (FVCOM), described by Wu et al. (2022), which employs a wet/dry treatment to simulate flooding/drying process in tidal flats (Wu et al., 2022). The model runs under three river flow conditions (low: 1,000 m^3 s^{-1}, medium: 5,000 m^3 s^{-1}, and high: 11,000 m^3 s^{-1}) for a one-month period of time with an hourly temporal resolution. From the model outputs at Steveston (Fig. 1.2), time series of depth-averaged eastward velocity is multiplied by the meridional transect area of the Fraser River to derive the river flowrate at the mouth. Compared to the tidal elevations at Pt. Atkinson from the same model, the river flowrate has a good correlation with the time derivative of tide with a phase lag of about 2 hours (Fig. 2.6a).

2.3.2 Surface Winds

Another important factor that affects the plume structure is the surface wind. Considering both location and duration, the best meteorological data for the Fraser River plume is from the Sand Heads lighthouse station, Environment Canada Climate ID # 1107010, which is positioned at the end of the jetty extending from Steveston to the edge of the mudflats (Fig. 1.2). Two-minute averaged hourly wind direction and speed data at 11 m can be downloaded from Environment Canada (https://climate.weather.gc.ca/historical_data/search_historic_data_e.html).

Data coverage from Sand Heads is good for the period of time in this study. For all 2466 selected SPM images, 2407 (97.6%) have an available, valid wind record ± 1 h from the time when these images are taken. As discussed in Sec. 1.2, winds in the Strait are generally either northwesterly or southeasterly, aligned with the long axis of the Strait. Southeasterly winds appear more often than the northwesterly winds throughout the year (Fig. 2.7), especially in winter seasons. This wind data will mainly be used in revealing the bias of SPM images to a preference to the northwesterly wind.

2.3.3 HF-radar Derived Surface Currents

High-Frequency (HF) radars have been used to monitor the surface currents along coastal oceans in the past decades. In the Strait of Georgia, Ocean Networks Canada (ONC) (https://data.oceannetworks.ca/home) maintains four CODAR Ocean Sensors Inc. SeaSonde units in the southern Strait of Georgia at the Westshore coal port (deployed in Dec 2011), Iona outfall (deployed Aug 2012), Georgina Point (deployed May 2016), and Point Atkinson (deployed January 2017) (Fig. 1.2). These direction-finding HF radar systems are sensitive to currents in the upper 50 cm of the water column, and they operate at a nominal frequency of 25 MHz. All stations produce hourly radial current maps by combining seven 10-minute averages that are gridded to range bins of 0.5 km and bearing bins of 5° (Pawlowicz et al., 2020; Halverson and Pawlowicz, 2016). Total current vectors are produced by stepping through all points on a regular 1 km × 1 km grid and combining all radial data within a 1 km search radius of each grid point with the vendor's software.

The advantages of CODAR data are that they have a very good spatial and temporal resolution, years of good records can be used, and they work well both day and night without being restricted by the weather conditions. However, a few drawbacks of this derived surface current data limit its application to this study.

First of all, only after the third station (at Georgina Point) was set up, did the surface current field start to cover the majority of the plume area, which means that only 3.5 years (mid-2016 to 2019) out of 17 years of satellite observation can be fully examined together with this HF-radar derived surface current field.

Secondly, both working range and accuracy of this HF-radar data are found to be sensitive to the surface conductivity (i.e., salinity). For example, in Halverson et al. (2017), the working range of HF-radar is found to be negatively and near-linearly correlated with surface conductivity with a decrease from 37.4 km at 3.5 S m^{-1} to 19.4 km at 0.9 S m^{-1}. In Halverson et al. (2018), a comparison with drifting buoy velocities finds that the HF-radar derived surface currents in the SoG underestimated the actual surface currents by 0 to 5 cm/s with RMSE ranging from 11.3 to 17.2 cm/s, but this underestimation can be as high as 30 to 50 cm/s in the Fraser outflow. Fraser River plume is characterized with the low surface salinity (i.e., low conductivity), which may not be accurately-observed by the HF-radar.

What's more, the percentage of valid HF-radar coverage is relatively low in summer (Fig. 2.8), at which time the majority of the satellite images are taken. This mismatch in

time would result in an even smaller subset of data in which both satellite and HF-radar observation are good in quality.

In spite of these disadvantages, HF-radar derived surface currents are still helpful to us in understanding the dynamics of the surface ocean in the Strait. As supplementary data, these surface currents will be used to support the short-term variation of the plume within same-day SPM image pairs, reveal the extent of diurnal and semi-diurnal influence of the river, and help to understand the dynamical structures of the plume.

2.3.4 Data along Ferry Track

In this study, the ferry track data are mainly used to estimate the surface salinity inside and outside the plume. The data were acquired from sensors on-board the British Columbia Ferry Services Inc. vessel M/V Queen of New Westminster (2003 to 2006) and Queen of Alberni (2012 onward). Specifically in this study, one year of record is good enough to evaluate the overall tidal influence on the plume salinity. Therefore, the following description about this ship-board measurements is purely based on the situation in 2018 from M/V Queen of Alberni.

For the study period, the vessel passes over the Fraser River plume up to eight times per day with the first sailing departing Tsawwassen at 5:15 in the local morning, and the last sailing departing Duke Point at 22:45 (Fig. 1.2). A complete transect takes about 2 hours and covers over 60 km across the Strait. Salinity, temperature, chlorophyll-a and dissolved oxygen, and turbidity data are measured at a 1-minute interval using water samples drawn through a 12.7-mm pipe with a length of 1.5 m(Wang et al., 2019). The water intake is known to be located 2 m below the surface with a variation up to 40 cm depending on the payload, but some uncertainty about the depth of the actual water being sampled still remains. For example, Hinatsu et al. (2003) shows that the effective sampling depth for such system can be shallower than the water intake depth as the surface water being subducted underneath the travelling vessel. A similar study on the previous sampling system in the SoG (2003 to 2006) also shows the sampled water is from about 1.5-m depth despite the intake being at 3.5-m depth (Halverson and Pawlowicz, 2011). Although there is no specific conclusion on the effective water sampling depth for the new system, in this study, the depth of 1 m is considered to be a close estimation to represent the layer of surface water being measured.

Analysis from earlier ferry datasets suggested that the Fraser River plume could be

easily identified along the Tsawwassen/Nanaimo route from the surface sea salinity (e.g., Halverson and Pawlowicz, 2008, 2011). However, the best method to automatically identify plume waters still remains a question. A new relative salinity threshold is developed to match with the SPM threshold at 2 g m^{-3}, and further details will be discussed in Sec. 3.5.

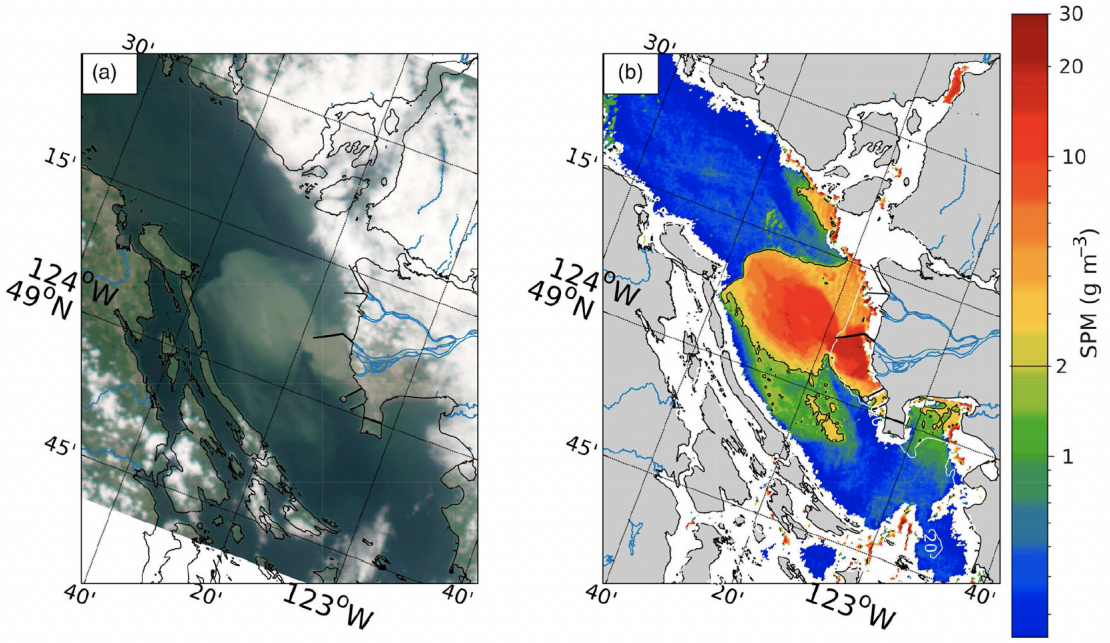

Figure 2.1: (a) "True Colour" image generated by merging RGB colour bands from the MODIS instrument for 10 June 2003 during a period of high river flow and southwesterly winds. (b) SPM derived from band 1 reflectance for the same date. (Fig. 2 from Pawlowicz et al. (2017)). Reproduced with permission from R. Pawlowicz.

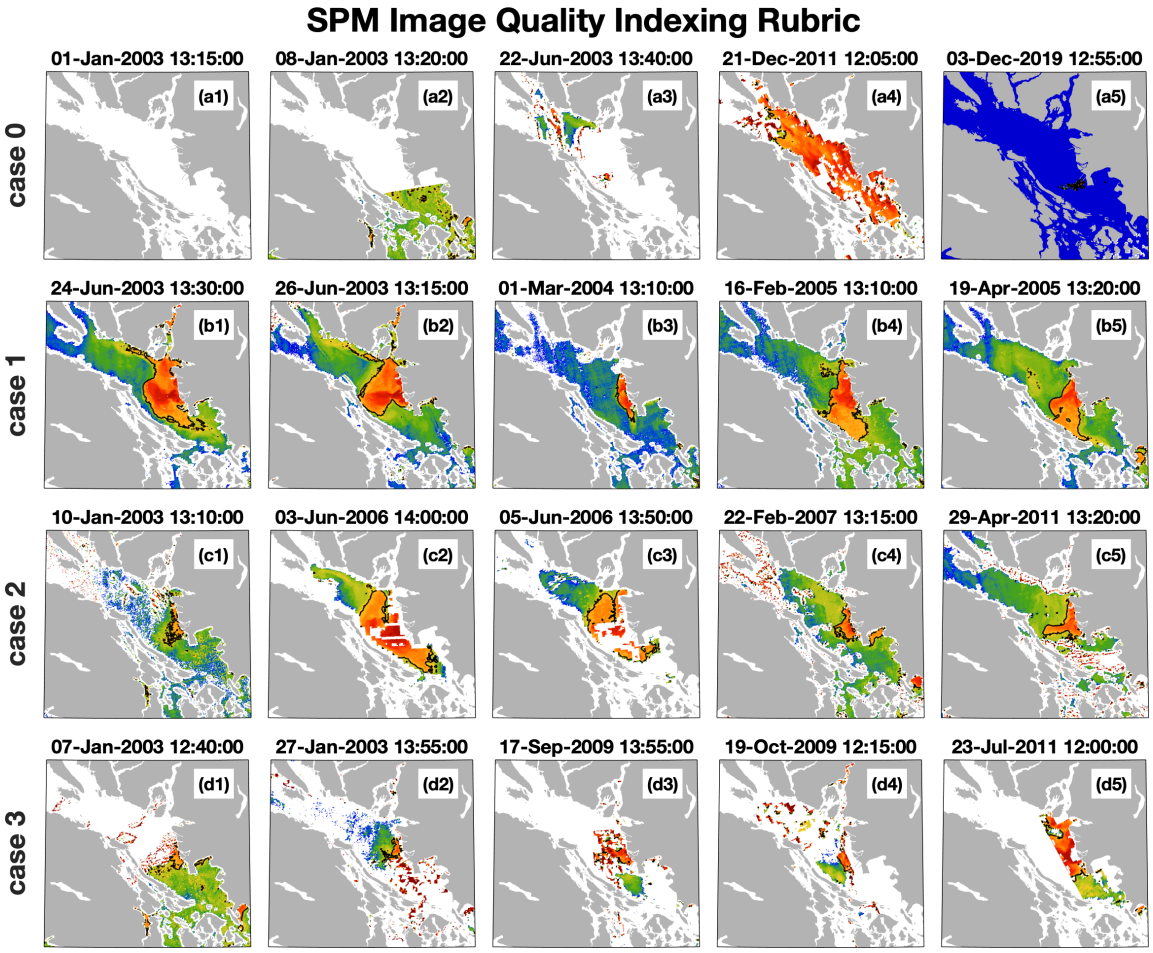

Figure 2.2: Examples of SPM images with different quality indices. (case 0: to be discarded, case 1: very good images, case 2: to be processed, case 3: others). All times are in PST. For geographical information, see Fig. 1.2.

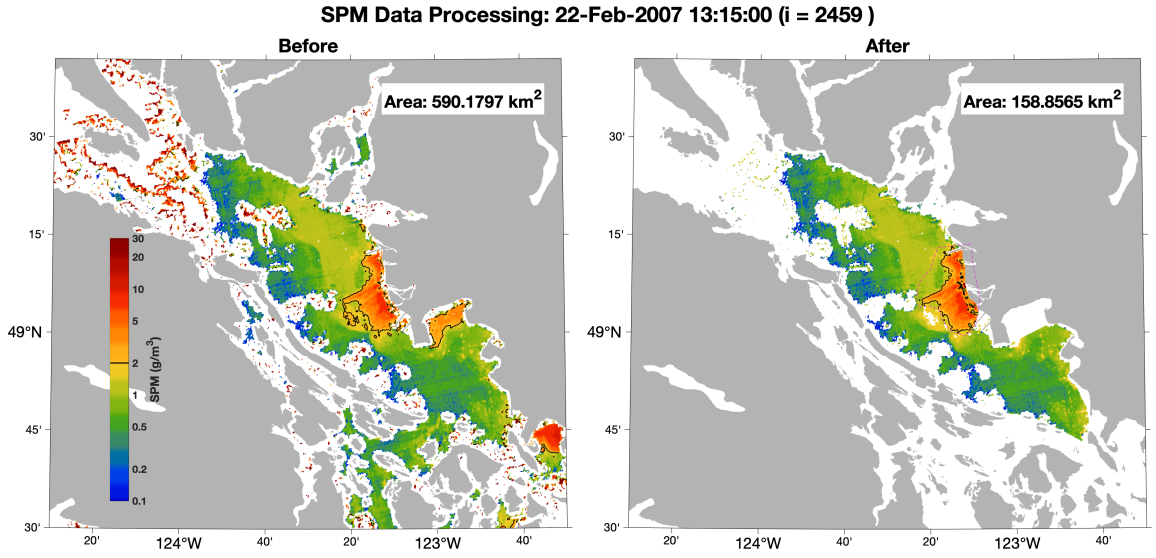

Figure 2.3: Example 1 of the SPM image before and after processing (a common winter case). i is the index of the image being processed. For geographical information, see Fig. 1.2.

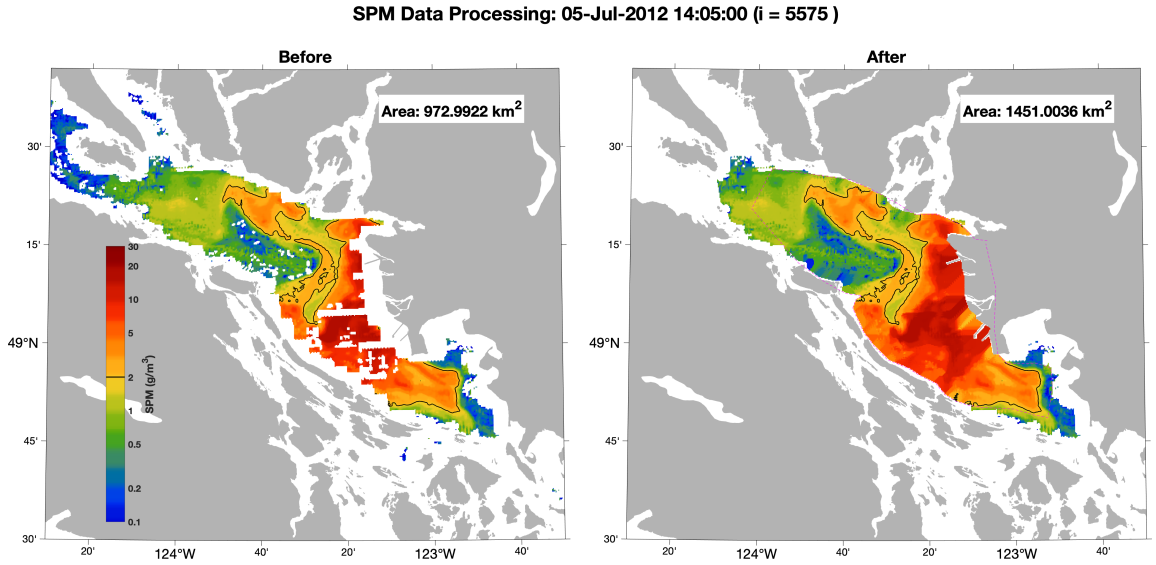

Figure 2.4: Example 2 of the SPM image before and after processing (a common summer case). i is the index of the image being processed. For geographical information, see Fig. 1.2.

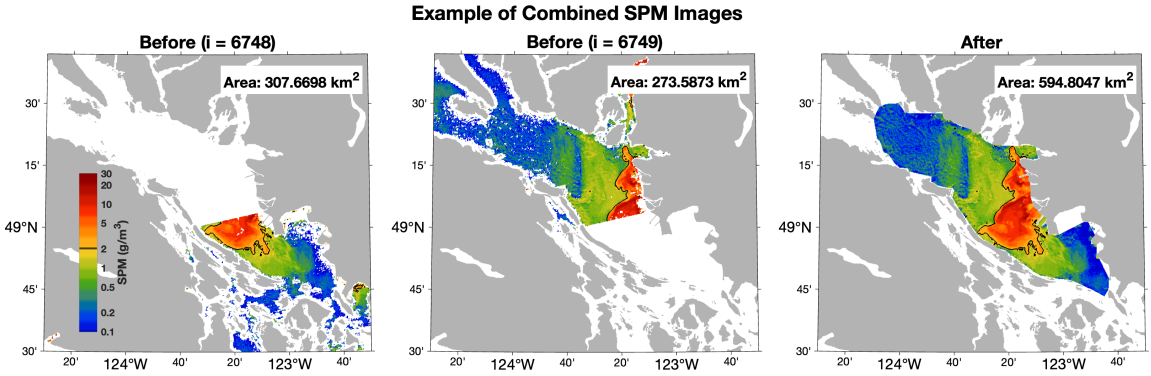

Figure 2.5: Example of combined SPM images. i is the index of the image being processed. i = 6748 was taken at 13:05 on July 28th, 2014, i = 6479 was taken at 13:10 on the same day. For geographical information, see Fig. 1.2.

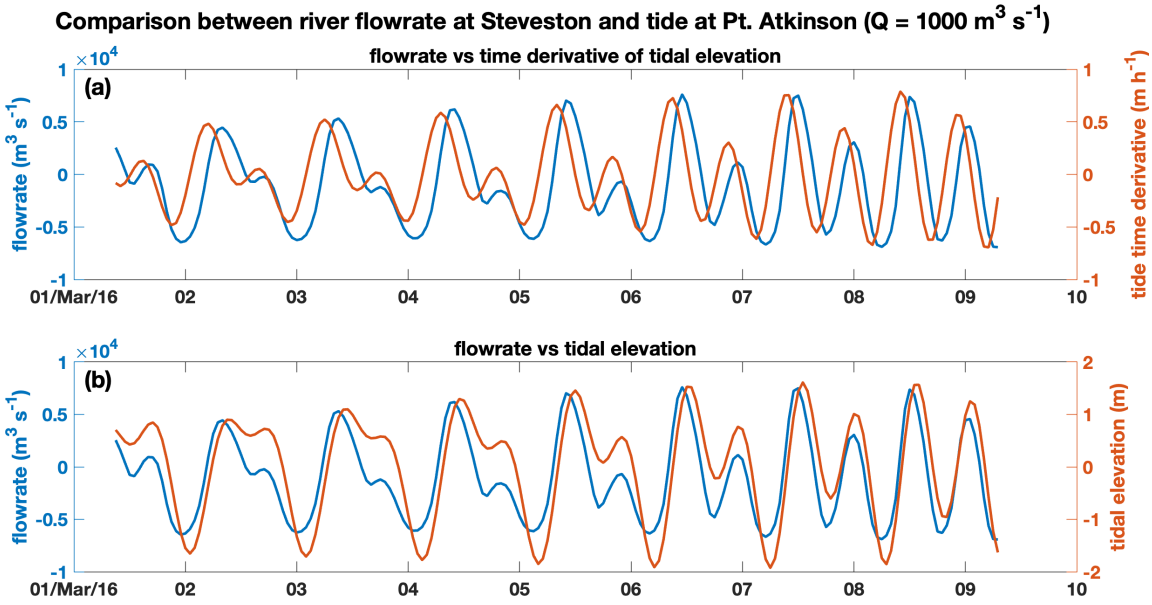

Figure 2.6: Example of hourly river flowrate at Steveston from FVCOM model output (blue curve) compared with (a) time derivative of tidal elevation at Pt. Atkinson, and (b) tidal elevation at Pt. Atkinson (red curves). In this example, the model runs under low river flow condition ($\bar{Q} = 1000$ m^3 s^{-1}), and the negative value of the river flowrate means that the fresh water discharges from the river into the ocean.

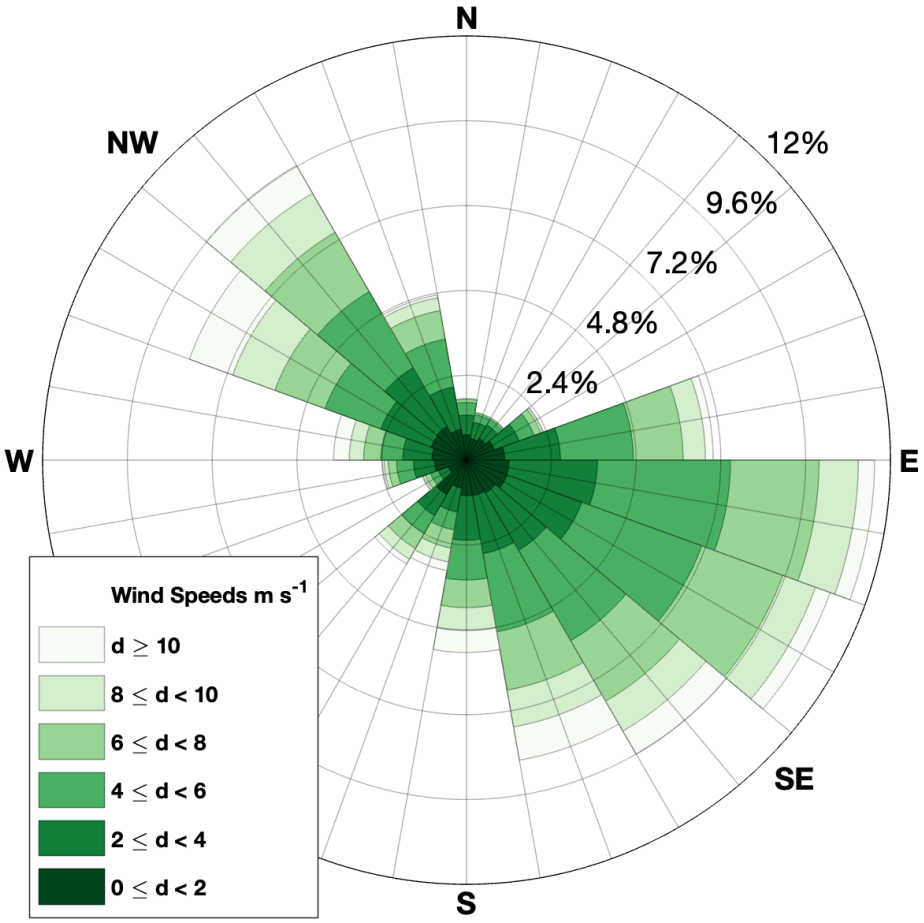

Figure 2.7: Wind rose for hourly wind speeds measured at the Sand Heads lighthouse station for the years 2003 to 2019. Note that the meteorological convention of using directions from which the wind originates is used.

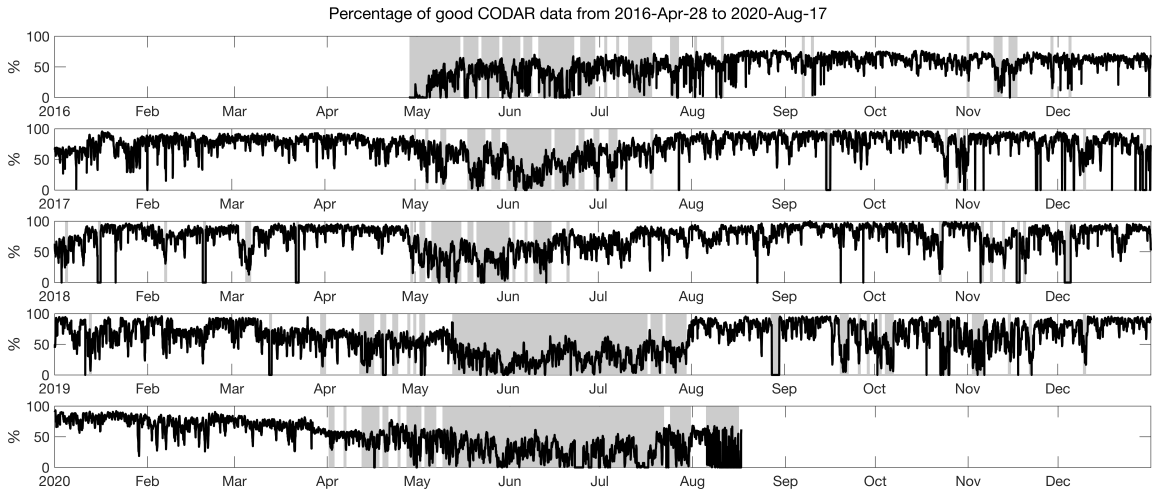

Figure 2.8: Percentage of good HF-radar (CODAR) data from 2016 to 2020. Bad days (days with an average coverage of less than 50% (i.e., 667 grid points)) are shaded in gray.

Chapter 3

Observational Results

This chapter consists of 6 sections of observational results and a brief summary. Specifically, the first section examines the subtidal variability in the plume area, and establishes a linear correlation between the plume area and the river flowrate. The second section points out a hidden bias in the SPM image collection, which is very important for extracting reliable tidal signals. Aware of this hidden bias, the third section carefully processes the data and finds a negative correlation between the tidal elevation and the plume area with an one-hour phase lag. Section 4 investigates the plume area changes between the same-day image pairs, and derives a very similar correlation between the tide and the plume area. In section 5, a salinity threshold for the ferry-measured surface salinity is established to best represent the SPM threshold used in the satellite observation, and the tidal variation in the plume salinity is investigated. In section 6, a tidal harmonic analysis of the HF-radar derived surface currents is made, and the horizontal plume structure is characterized by the difference in the extent of diurnal/semi-diurnal influence of the river. At last, the primary findings of the observational results are summarized.

3.1 Subtidal Variability of the Fraser River Plume Area

In this study, although over one thousand previously discarded "bad-quality" images (by Pawlowicz et al. (2017)) are included in our dataset, after a proper processing, the expanded image collection still shows a consistent correlation between the plume area and the river flowrate (Fig. 3.1). The only exception is found in August 2016, when an unprecedented coccolithophore bloom causes the water across much of the SoG to turn into a bright, almost fluorescent, green colour (Gower and King, 2016). This event affects 17 images (grey dots in Fig. 3.1), and these images are then excluded from further analysis.

In the earlier study, Fraser River plume area was found to be linearly correlated with the river flowrate with the following relationship (Pawlowicz et al., 2017) (black curve in Fig. 3.2):

$$A/\mathrm{km}^2 = 0.1244 Q_{\text{Port Mann}}(d)/(\mathrm{m}^3/\mathrm{s}) + 1.44 \tag{3.1}$$

($r^2 = 0.68$, standard error $\pm$ 190 km^2) where A is the plume surface area (km^2) and $Q_{\text{Port Mann}}(d)$ is the estimated river flowrate at Port Mann based on data from gauging stations at Hope and Chilliwack for the same day when SPM image is taken (more information about this calculation is provided in Sec. 2.3.1).

With the expanded image collection in this study, the relationship is found to be:

$$A/\mathrm{km}^2 = 0.1342 \;\; Q_{\text{Port Mann}}(d)/(\mathrm{m}^3/\mathrm{s}) - 14.06 \tag{3.2}$$

($r^2 = 0.705$, standard error $\pm$ 196 km^2, red curve in Fig. 3.2).

The new correlation agrees well with the existing equation with a small improvement in r^2 and a very minor increase in the standard error. As discussed in Sec. 2.2.2, without careful image processing and interpolation, summer images (with big plumes) tends to underestimate the plume ares because of the missing data at the centre of the plume, while winter images (with small plumes) usually overestimates the plume area due to cloud patches that are not properly masked. In this study, every single image is individual examined and processed, which partly solves the overestimation/underestimation in the winter/summer images, and results in a regression curve with a steeper slope. Although the intercept from this regression (- 14.06 km^2) seems to be near 10 times bigger than that from the previous study (1.44 km^2) in magnitude, this difference is actually fairly small compared to the range of the plume area ($\sim$ 2000 km^2).

However, this correlation relationship can be further improved. The observed peak of the plume area seems to occur slightly later than the peak of the river flowrate, especially after some high-precipitation events in fall and winters (Fig. 3.1). Theoretically, the plume needs time to grow after a massive feeding of freshwater, and the existing plume also needs time to dissipate when the river discharge decreases. This may indicate a better correlation of plume area with an earlier river discharge. After a cross-correlation analysis, the best correlation (maximum r^2 and minimum RSME) is found to use the river discharge that is 2 to 3 days earlier than the plume image (Table 3.1). This slight mismatch in time is similar to the Fraser River plume freshwater flushing time, which is estimated to be 2.2 days by Halverson and Pawlowicz (2011). Regression curve for the correlation using river flowrate 3 days ahead of satellite images is shown in green colour in Fig. 3.2, and this equation will be used for the further analysis:

D.A. (days)	-6	-5	-4	-3	-2	-1	0	1
Slope ($\frac{km^2 s}{m^3}$)	0.130	0.132	0.135	0.136	0.136	0.135	0.134	0.133
Y-intercept (km^2)	-10.4	-19.7	-27.7	-31.1	-29.2	-22.7	-14.1	-6.8
r^2	0.676	0.698	0.714	0.723	0.720	0.711	0.705	0.697
RMSE (km^2)	206	198	193	190	191	194	196	199

Table 3.1: Properties of linear regression (slope, intercept on the vertical axis, coefficient of determination (r^2), and root mean square error (RMSE) in km^2). D.A. (days after) stands for the time gaps between the datasets (river discharge and plume area) for the regression. For example, "D.A. = -3" means that river discharge three days ahead of the time when SPM images are taken was used for the linear regression.

$$A/\mathrm{km}^2 = 0.1361 \; Q_{\mathrm{Port\ Mann}}(d - 3\ \mathrm{day})/(\mathrm{m}^3/\mathrm{s}) - 31.1 \tag{3.3}$$

3.2 Temporal Biases in Satellite Imagery

As described in the previous chapter, 2466 satellite images are used to derive a time series of the Fraser River plume area (Sec. 2.2). However, this image collection is not evenly distributed and some hidden biases may significantly complicate our analyses.

The first intuitively-occurring bias comes from the seasonal cycle of the cloud coverage above the Strait. Since the plume can only be observed by the satellite under a clear sky, the cloud coverage determines the availability of useful images. Located in a moderate Mediterranean climate zone, the Strait of Georgia usually has dry summers and rainy winters, which results in a preference for images to occur during the clear skies in summer. From the image collection, nearly 70 % are between April and September (blue curve in Fig. 3.3b). At the same time, Fraser River discharge during its freshet is 6 to 10 times larger than it is in winter months, which results in much bigger plumes. Thus, more images are seen in summer with a big plume, and less images in winter with a small plume.

The second well-known bias of the image collection comes from a preference for northwesterly winds. According to hourly wind records from Sand Heads lighthouse, strong[7] southeasterly winds (purple curve in Fig. 3.3a) appear more often than strong northwesterly winds (orange curve) in almost all months. However, the number of useful SPM images under strong northwesterly winds is about 2.5 times larger than those under southeasterly

[7] In this thesis, strong winds refer to winds from any direction with a speed over 4 m/s.

winds. This bias reflects that winds from northwest tend to bring a clear sky and good weather to the Strait of Georgia.

Another important but less-known bias of the SPM images comes from the relative phase shift of the daily tidal cycles throughout the year. As introduced in Sec. 1.3, the daily lower-low tide in the Strait is mostly around the middle of the day from April to September, while mostly around midnight in the rest of the year (Fig. 1.5). Since the satellites scan over the Strait at about the same time in the local day (11:22 for Terra and 13:04 for Aqua), it implies that summer images are generally taken in the "big ebb" cycle (tide lag hour, h, from -7 to 7) in any day, while the winter images contribute only to the "small ebb" cycle (h $>$ 7). Given the fact that summer images usually contain large plumes, the averaged plume area over a tidal cycle is thus significantly manipulated by this seasonal cycle of tidal phase relocation.

As an illustrative example of this bias, scatter-plots of the plume area and the river discharge over a tidal and seasonal cycle are compared in Fig. 3.4a1 and b1. It is clear that tidal signals of the plume area variation are totally submerged in the strong seasonal cycles. Without removing this seasonal variation of the plume, a simple average of plume area (or river discharge) over a tidal cycle will lead to a completely false result.

More specifically, the river flowrates from Station Hope and Chilliwack, which are both far away from the river mouth, are known to be not impacted by the stage of tide. However, when this flowrate dateset (corresponding to the times when SPM images are taken) is averaged across tidal cycles, high flowrate in the spring and summer will only contribute to half of the tidal cycle (tide lag hour from -4 h to 8 h), which results in an unrealistic "high river discharge in the flooding tide" (Fig. 3.4b1, b2).

3.3 Plume Area Variation under a Tidal Cycle

In order to reveal the tidal impact on the Fraser River plume area, the first step is to reduce the bias and seasonal signals from the SPM image collection. Knowing that the largest effect on the plume size is the river flow (Sec. 3.1), a new variable R_{AF} (normalized plume area) is defined as an alternative to the plume area itself:

$$R_{\mathrm{AF}} = \frac{A_{\mathrm{actual}}}{A_{\mathrm{forecast}}} = \frac{A_{\mathrm{actual}}/\mathrm{km}^2}{0.1361 Q_{\mathrm{Port\ Mann}}(d - 3\ \mathrm{day})/(\mathrm{m}^3/\mathrm{s}) - 31.1} \tag{3.4}$$

where A_{actual} is the actual plume area observed by the satellite, and A_{forecast} is the plume area estimated from the regression to the river flowrate (Eq. (3.3) and Table 3.1). $Q_{\text{Port Mann}}$ is the derived plume flowrate from Station Hope and Chilliwack, and $(d-3 \text{ day})$ stands for a cross-correlation with the plume area being delayed by 3 days. Using plume area with a 3-day delay is to reduce the errors from the remaining big plumes after occasional water surges due to high precipitation events (Sec. 3.1). R_{AF} is then a unitless parameter which averages to about 1. In a tidal cycle, for example, $R_{\text{AF}} = 1.05$ means that the the plume area is 5% larger than its daily average at this stage.

However, there are still some seasonal signals that remain unexplained. A moving average of R_{AF} over a single year with an 1-day step size and a $\pm$ 10-day window size shows some high anomalies in April and November (Fig. 3.5a). These high values in April may relate to the relatively higher turbidity from the river input at this time. Since the plume area in this study is defined as the summation area of the image pixels whose SPM concentrations are above the 2 g m^{-3} threshold, a higher turbidity in the plume may yield a larger plume extent. Then, in November, high precipitation events in the lower-mainland may cause a surge in the Fraser discharge, which results in a rapidly growing plume. Although the river discharge data from Chilliwack was used to better reflect these special events, in some cases, the Fraser discharge at its mouth is still considerably underestimated, which inflates the resulting R_{AF}. This remaining seasonal variation may still affect the analysis of tidal variation.

To reduce this secondary seasonal variation, the original R_{AF} is divided by the ratio of its nearest daily moving average to its global mean. The new R_{AF} (Fig. 3.5b) then shows a moving average that nicely lies around the overall mean of R_{AF}. Additionally, data points that are larger than the 0.99 quantile ($R_{\text{AF}} = 2.09$) and smaller than the 0.01 quantile ($R_{\text{AF}} = 0.23$) are considered as outliers and are removed. Hereafter, if not specifically stressed, R_{AF} refers to this new version in which its remaining seasonal pattern is removed. Although the moving variance (standard deviation) also has a clear seasonal cycle with relatively low values from May to September and high values for the rest of the year, it may imply a more dramatic tidal modulation on the plume area in winter months. In order preserve this information, no further reductions are made to the data variance in winter months.

After removing the seasonal variation of the plume area, tidal signals start to emerge (Fig. 3.6). A clear transition from relatively larger plumes during low tides to relatively smaller plumes during high tides is found. Averaged across tidal cycles, normalized plume

area (R_{AF}) is found to be negatively correlated to the tidal elevation with a small phase lag. More specifically, the biggest plume is usually found about 1 hour later than the lower-low tide of the day, while the smallest plume is about half an hour later than the higher-high tide of the day (Fig. 3.7b). Unlike the unrealistically dramatic change of plume area of over 100% from the biased original data (Fig. 3.4a2 and 3.7a), R_{AF} tends to grow 18.5% during the big ebb period (tide lag hour from -7 to 1) followed by a decrease of 18.7% in the next 7-8 hours of flooding tide. Then, a similar increase of 17.2% and a decrease of 22.1% of the plume area occur during the rest of the tidal cycle (Fig. 3.7b, Table. 3.2).

Overall, using R_{AF} as an alternative representation of the plume area decreases the bias introduced from a series coincidence of tide, river discharge and satellite scanning time. However, the way of deriving this new variable may also introduce some artificial errors and uncertainties. For example, although the negative correlation between the tidal elevation and R_{AF} is generally consistent, the exact curve of mean R_{AF} over a tidal cycle and the magnitude of the plume resizing are slightly sensitive to the method of reducing secondary seasonal signals and the removal of outliers. To further substantiate the observed tidal variation is the plume area, a second independent analysis to this problem is applied.

3.4 Plume Area Variation under Same-day Image Pairs

To reveal the pure plume area variation over a short period of time, an analysis of the plume area change in the same-day image pairs becomes key. As introduced in Sec. 2.1, because of the design of satellite orbit and swath, the SoG is sometimes observed twice a day by the same satellite with a time gap of 1 hour and 40 minutes. This feature provides us with an opportunity to directly study the individual plume behaviour over short time intervals. From 2013 to 2019, there are 3300 days when two satellite images are available. However, only 247 of such image pairs have fully or near-fully identifiable plume boundaries in both images to estimate the plume area change.

The processing procedure of these paired images is similar to the processing of individual SPM images, but requires some more care. Unlike estimating the plume area from a single image, the amount of plume area change within each image pair ranges from a few km^2 to dozens of km^2, and it is much more sensitive to the design of plume boundary masks. In some cases, the individual optimal interpolation may introduce unexpected inconsistency and exaggerate the difference between the plume area purely from the different plume masks being applied.

In order to reduce the error, all 247 image pairs are additionally inspected. As an illustrative example, the same outer mask (magenta curves) and inner mask (cyan curves) are specifically designed for both pre-processed plume images (Fig. 3.8a1, b1). Then, the plume areas are calculated (a2, b2) and the plume contours are compared (red curves for the first image and blue curves for the second image in a3 and b3).

In this example, the river flowrate is $\sim$ 5100 m^3 s^{-1}, and moderate wind comes from the northwest. Two images are taken right before and after the lower-low tide of the day. The plume area has a small increase of 21 km^2 (3 %), mainly coming from a strong push of the cross-strait currents from the mouth of the Fraser to the southwest. The northern plume front expands slightly northward as the background southeastward currents from the northern Strait ceases. At the same time, in the southeast end of the plume, the front starts to disintegrate and retreat back to the plume centre (Fig. 3.8).

A time series of the area difference within all image pairs can then be generated. However, the value of the plume area increase/decrease is related to the size of the existing plume at a given time, and the precise time gap between two images could be a few minutes shorter or longer. Therefore, to keep the consistency of the data, a new variable is defined as the percentage of the plume area change per hour (R_C):

$$R_C = \frac{A_2 - A_1}{A_1(t_2 - t_1)} 100\% \tag{3.5}$$

where A_1 (in km^2) and t_1 (in hour) are the area and time for the first image in the pair, while A_2 and t_2 are for the second image. R_C that are above the 0.99 quantile or below the 0.01 quantile are considered as outliers and are removed.

As this rate is displayed over a tidal cycle, a tendency of increased plume area (red lines) during the ebb tides and decreased plume area (blue lines) during the flood tides shows up (Fig. 3.9a), which agrees with the earlier demonstrated negative correlation between the plume area and the tidal elevation in Sec. 3.3. This pattern is found to be consistent throughout the year from March to September (Fig. 3.9b).

Theoretically, R_C is an estimate of the time derivative of the plume area variation. Thus, instead of a correlation to the tidal elevation, the plume area change rate (R_C) is expected to be negatively correlated to the time derivative of the tidal elevation (D_T, in m h^{-1}):

$$D_T = \frac{d\eta}{dt} \tag{3.6}$$

where η is the tidal elevation at Pt. Atkinson. This negative correlation between R_C and D_T is observed in the results (Fig. 3.10b).

In order to directly compare the results from two different approaches, the time derivative of the R_{AF} curve is calculated. This time derivative of averaged R_{AF} (as percentage change per hour ($dR_{AF}/dt \times 100\%$), shown as dashed red curve in Fig. 3.10b) agrees well with the pattern of averaged R_C (blue curve in the same figure) for the most of the tidal cycle. Even a simplified regional linear representation of the R_{AF} variation (green curves) matches reasonably well with the magnitude of R_C. Integrating the R_C curve by segments, the accumulative plume area changes for the big flood (-18.8%), small ebb (+18.3), and small flood (-23.4%) period are remarkably similar to the overall R_{AF} change for the same periods (-18.7%, + 17.2%, and -22.1%, respectively) (Table. 3.2). The only exception is in the big flood of the day, at which period the accumulative area change from R_C (+35.3%) is noticeably higher than that from R_{AF} (+18.7%).

Other than the general agreement of the tidal patterns in the plume area variation from the two methods, some detailed phase lags observed in the earlier section area reconfirmed in the analysis of the same-day pairs. R_C at one hour after the lower-low tide of the day is found to be positive, which agrees with the short period of continued area increase after the lower-low tide in the pattern of R_{AF}. More specifically, a cross-correlation analysis between the normalized plume area (R_{AF}) and the tidal elevation (η) finds a best correlation of the two variables when the phase is shifted by 63 minutes (Fig. 3.11a, c). A similar analysis on R_C and D_T results in an almost identical phase shift at 62 minutes (Fig. 3.11b,d). The slope of the regression curve between R_{AF} and η is about -6.58×10^{-2}, which means that as the water level in the Strait goes up/down by 1 m, the plume area tends to decrease/increase by about 6.58% (Fig. 3.11a). The slope of the regression between R_C and D_T gives a similar but slightly larger rate of about 8% of plume area change per meter of sea level change.

Furthermore, the same approach and comparisons can be applied to observational data under different river flowrate conditions: medium-low flowrate condition ($\bar{Q} < 5000$ m^3 s^{-1}), and high flowrate condition ($\bar{Q} > 5000$ m^3 s^{-1}). When $\bar{Q}$ is relatively low, the satellite observed plume area variation (R_{AF} curve) shows a smooth transition throughout the tidal cycle, and nicely reflects the tidal patterns (Fig. 3.12a1). The magnitude of the plume area change for each tidal segment (big ebb, big flood ...) increases from about 19% on average to about 23% (Table 3.2). However, for the high river flowrate condition, there is no significant tidal variation found in the plume area (Fig. 3.12b1, b2).

To look at the transition of this tide-plume correlation under different river flowrates, we use a series of subsets of plume areas, staring from 0 m^3 s^{-1} < $\bar{Q}$ < 2000 m^3 s^{-1}, incrementing by 100 m^3 s^{-1}until approaching 10000 m^3 s^{-1}, and then generate a series of the correlation coefficients (R) and the slopes of the linear regression between tide (η, D_T) and plume area (R_{AF}, R_C) of these data subsets, with additional adjustment on the phase lag delays (Fig. 3.12c1). The results show the strongest linear correlation when the river flowrate is relatively low. Especially for $\bar{Q}$ < 3000 m^3 s^{-1}, the slopes of the linear regression between (R_{AF} and η) and (R_C and D_T) are found to be consistently at about 11 to 13 % m^{-1}, which are over 60% larger than those from a regression of all available observations.

As the river flow becomes stronger, the magnitudes of the correlation coefficient and the slope gradually decrease. When river flowrate is above 6000 m^3 s^{-1}, both R and the slope of the regression between R_{AF} and η approach to zero, which means no more correlation is found between η and R_{AF}. For the correlation between D_T and R_C, although R never reaches zero, the slope of the regression near-linearly decreases as the river flowrate increases (Fig. 3.12c2).

Comparing these two methods, the analysis based on R_{AF} makes full use of all available images. Although an uneven distribution with more data from summer months still exist, the number of winter images is sufficient to capture a relatively smooth transition during the small ebb cycle. However, using R_{AF} is an indirect measurement of the plume area, which contains more variance other than the pure area variation. Noise in the time series of R_{AF} is relatively large compared to the tidal signals, given a relatively poor correlation coefficient ($R \sim$ -0.22, Fig. 3.11a) for the linear regression between R_{AF} and tidal elevation (η) with adjusted phase lags.

On the contrary, the analysis of the same-day pairs uses a direct measurement of the plume area change over a short period of time. The correlation between R_C and D_T is much stronger ($R \sim$ -0.41, Fig. 3.11b) than that from the first method. However, the problem with the uneven data distribution is worse as the available same-day pair observations in winter (therefore, the small ebb cycle) are sparse. Only 13 image pairs are usable from November to January throughout all 17 years, and consequently, only 18 (7.3 %) samples falls in one third (before h = - 3.5 and after h = 13) of the tidal cycle. Especially for the period before h = -6 and after h = 16, only 4 of such observations are in use, which means the tidal pattern of R_C in the early-big-ebb period and the late-small-flood period is not very reliable. The noticeable mismatch between the two methods for these periods could

		Big Ebb	Big Flood	Small Ebb	Small Flood
Overall Plume Area Variation	R_{AF}	+18.5%	-18.7%	+17.2%	-22.1%
	R_C	+35.3%	-18.8%	+18.3%	-23.4%
Medium-Low Flowrate Condition	R_{AF}	+22.3%	-25.2%	+19.9%	-22.8%
	R_C	+41.4%	-21.4%	+18.7%	-23.4%

Table 3.2: Summary of the plume area variation under different stage of tide (i.e., the big ebb, big flood, small ebb, and small flood). R_{AF} and R_C refer to the results from two independent methods based on satellite observed SPM images (Sec. 3.3, 3.4). Results for the medium-low river flow condition is calculated based on a subset of all observations in which daily averaged river flowrate is below 5000 m^3 s^{-1} (Fig. 3.12).

also be partly explained by the lack of good observations in the same-day pairs.

Overall, these two independent methods complement each other well showing a tidal variation in plume area of near 20% on average, and consistently show a negative correlation between the tidal elevation and Fraser River plume area with a phase lag of about 1 hour. The magnitude of the daily averaged river flowrate has significant influence on the tide-plume correlations, and a relatively low daily river discharge usually leads to a bigger tidal variation in the plume area. In the next two sections, the tidal variability in the plume salinity and the extent of river influence on the surface currents will be further investigated to provide us a deeper understanding in the dynamic features of the tide-plume interactions.

3.5 Tidal Influence on the Fraser River Plume Salinity

As a mixture of river water and seawater, the salinity of the plume is a critical parameter that actively affects its volume and extent. Specifically for this study, the tidal variability in the Fraser River plume salinity is important to understanding the dynamics of the plume area variation over a tidal cycle. As introducted in Sec. 2.3.4, the instrumented ferry that routinely crosses the Strait provides a good record of the surface salinity at a relatively high spatial and temporal resolution. However, to estimate the plume salinity using this dataset, a clear definition of the plume water along the ferry tracks should be established. In other words, a good salinity threshold is needed to define the boundary between the plume waters and non-plume waters.

In Halverson and Pawlowicz (2008, 2011), this salinity threshold was defined as $S_{ref} - S_{offset}$, where S_{ref} (reference salinity) is the spatial mean of salinity between 45 and 50 km away from Tsawwassen Terminal, and S_{offset} (salinity offset) is a linear function of the

reference salinity. S_{offset} varied between 0.4 to 1.8 PSU with the highest value when the S_{ref} is the biggest. However, in the present, the plume boundary is defined as SPM = 2 g m^{-3} from the satellite imagery. Whether or not this salinity threshold definition used in this previous work is comparable to the SPM threshold is not clear.

To address this problem, 147 satellite images taken in 2018 are carefully examined and compared with the ferry tracks that are closest in time. Among all good satellite images in 2018, 121 of them are paired with a ferry track that is within ± 2 hours from the time when the image is taken, and 82 of them see an intersection between the ferry track and the plume contour at SPM = 2 g m^{-3}. In the other 39 images, the ferry track does not intersect the plume. This occurs either during low river flowrates (when the river turbidity is low and/or the plume is close to the river mouth), or under strong southeasterly winds when the plume is pushed northwards.

For the remaining 82 images, the SPM concentration is interpolated onto the ferry tracks, and a strong negative correlation is found between the SPM concentration and the surface salinity (Fig. 3.13b). As an illustrative example, such a comparison is made on July 5th, 2018, when the river flowrate is relatively high (Fig. 3.13). The correlation coefficient (R) between the SPM and the salinity is found to be about -0.98 (coefficient of determination, $r^2 \sim 0.96$), and the salinity threshold ($ST_{\text{abs}} \sim 19.4$ g/kg) is derived based on this linear regression at SPM = 2 g m^{-3}. As shown in Fig. 3.13c, this salinity threshold works well in finding the plume boundaries and nicely separates the plume water from the non-plume waters. Additionally, ferry measured surface turbidity is shown on top of the interpolated SPM concentrations to address the good alignment between the ferry and satellited based observations (Fig. 3.13d).

From the example above, $S_{\text{ref}} - ST_{\text{abs}} \sim 3.7$, which is already bigger than the higher bound of S_{offset} in Halverson and Pawlowicz (2008, 2011). On average, $S_{\text{ref}} - ST_{\text{abs}}$ from all 82 examples in 2018 is about 6.8 g/kg with a standard deviation of 3.2 g/kg. Therefore, the salinity threshold from Halverson and Pawlowicz (2008, 2011) tends to result in a plume boundary wider than the satellite observation, and thus, it is not used for this analysis. Instead, a relative salinity threshold (ST_{rel}) is found to be better choice (Fig. 3.14):

$$ST_{\text{rel}} = \frac{ST_{\text{abs}} - S_{\text{min}}}{S_{\text{max}} - S_{\text{min}}} \tag{3.7}$$

where ST_{abs} is the absolute salinity threshold derived from the regression between SPM concentration and salinity, S_{max} is the local maximum of the salinity west of 123.7 °W, and

$S_{\min}$ is the minimum salinity along the ferry track. From the example above, ST_{rel} is about 0.72, and according to Fig. 3.13c, using a ST_{rel} that is 0.1 higher/lower than 0.72 will only exclude/include one extra data point in the calculation of the plume salinity. Therefore, as long as the plume has a clear frontal structure, the use of ST_{rel} has good flexibility and error tolerance. To apply this relative salinity threshold from the 82 examples to all ferry tracks in year 2018, an empirical formula for ST_{rel} is developed based on the river flowrate (Fig. 3.14a):

$$ST_{\text{rel}} = \begin{cases} 6.5 \times 10^{-5}\, \bar{Q}/(\text{m}^3/\text{s}) + 0.30, & \bar{Q} < 6300\ \text{m}^3\,\text{s}^{-1}. \\ 0.71\ , & \bar{Q} > 6300\ \text{m}^3\,\text{s}^{-1}. \end{cases} \tag{3.8}$$

where $\bar{Q}$ is the daily averaged river flowrate. In year 2018, there are 2052 ferry tracks in total, however, 348 of them either show a salinity range ($S_{\max} - S_{\min}$) smaller than 5 g/kg, or see the plume with a width less than 5 km along the ferry track. Both of the conditions above may indicate that the ferry either does not go into the plume, or it just passes through the very edge of the plume. Therefore, these 348 data points are excluded.

For the remaining 1704 ferry tracks, the ambient ocean salinity (S_{o}) and ferry-measured plume salinity (S_{f}) are calculated. S_{o} is simply taken as an overall average of the salinities above ST_{abs}, however, the estimation of S_{f} requires more care. The plume is usually more fresh at its core and more salty at its edge. When the ferry passes over the plume core, the relatively fresh water accounts for asymptotically $\mathcal{O}(n^{-1})$ of the salinity along the ferry track, but it actually only occupies $\mathcal{O}(n^{-2})$ of the plume area. Therefore, a higher weight is given to the "saltier" waters in the plume, and a smaller weight is given the "fresher" plume waters:

$$S_{\text{f}} = \frac{\sum_{i=1}^{n} S_{\text{f}}(i)[i^2 - (i-1)^2]}{n^2} \tag{3.9}$$

where n is the number of salinity data points that are below ST_{abs}, and $S_{\text{f}}(i)$ refers to each individual data point that is sorted in an ascending order. The equation above assumes the the horizontal plume salinity distribution is composed of concentric rings, with the outer rings larger and more salty than the inner rings. Based on this formula, S_{f} is then a weighted average of these salinity records below the given salinity threshold.

Then, S_{o} and S_{f} are averaged across tidal cycles to show the tidal influence on the overall salinity variation inside and outside of the Fraser River plume (Fig. 3.15a1-a4,

b1-b4). Additionally, since there are up to 8 ferry tracks crossing the Strait a day, hourly plume salinity change can be derived from the 7-a-day consecutive ferry track pairs (Fig. 3.15c1-c4). Similar to the concept of the same-day image pairs (R_C in Sec. 3.4), calculating dS_f/dt based on the salinity change between consecutive ferry tracks is considered to be a more direct and accurate method rather than a simple derivative of the S_f curve over a tidal cycle.

Over all river flow conditions, S_o is consistently around 25.0 g/kg, with a slightly higher value (26.2 g/kg) and smaller scatter under low flowrate conditions, and a lower value (23.3 g/kg) with a relatively larger variance under high flowrate conditions. Tidal influence is found to be minimal in the variation of S_o. On the contrary, ferry-measured plume salinity (S_f) is significantly modulated by tide. On average, S_f routinely increases about 2.5 g/kg (15%) from its daily minimum (near the lower-low tide of the day) to its daily maximum (near the higher-high tide) (Fig. 3.15b1). Independently derived dS_f/dt over a tidal cycle also captures the general salinity increase (up to 0.64 g/kg per hour) during the big flood of the day (Fig. 3.15c1). This daily variation in S_f is found to be slightly higher in magnitude ($\sim$ 3.2 g/kg) when the river flowrate is relatively low, and slightly lower ($\sim$ 2 g/kg) when the river flowrate is high. However, since the daily averaged S_f is also controlled by $\bar{Q}$ ($\bar{S}_f$ = 20.8 g/kg, 16.8 g/kg, 12.8 g/kg at low, medium, and high river flowrate conditions), the percentage of daily S_f variation is found to be consistently around 15-16% independent of the river flowrate.

However, the degree to which S_f and dS_f/dt represent the salinity variation of the whole plume is still not clear. As introduced in Sec. 2.3.4, the ferry draws water at an intake depth of 2 m below its surface. However, because of the subduction of the surface water underneath the travelling vessel, the effective sampling depth is usually estimated at about half of this intake depth (e.g., in Halverson and Pawlowicz (2011)). For the purpose of this study, S_f is then roughly considered as the plume salinity at a depth of about 1 m.

In Halverson and Pawlowicz (2011), the Fraser River plume is approximated as a linearly stratified layer, which assumes the plume salinity linearly increases from the surface to its base ($\bar{D}$ for the overall plume depth) (e.g., Fig. 4.1). Following the same approach, the vertical dependence of the plume salinity can then be established based on the salinity at two known depths (S_f at $z \sim 1$ m and S_o at $z = \bar{D}$):

$$\frac{S(z) - S_o}{S_f - S_o} = \frac{z - \bar{D}}{z_0 - \bar{D}} \tag{3.10}$$

where $S(z)$ is the plume salinity at a certain depth (z), $\bar{D}$ is the average plume depth, and $z_0 = 1$ m is the effective sampling depth of the ferry. The equation above can be rearranged as:

$$S(z) = S_o - \frac{S_o - S_f}{\bar{D} - z_0}\bar{D} + \frac{S_o - S_f}{\bar{D} - z_0}z \tag{3.11}$$

and then, the overall plume salinity (S_p) can be estimated as:

$$S_p = \frac{1}{\bar{D}}\int_0^{\bar{D}} S(z)dz = S_o - \frac{\bar{D}}{2(\bar{D} - z_0)}(S_o - S_f) \tag{3.12}$$

For convenience purposes, a correction factor γ is used to replace $\bar{D}/[2(\bar{D} - z_0)]$, where $z_0 = 1$ m. Based on its definition, γ is a function of the average plume depth $\bar{D}$. In a recent study by Kastner et al. (2018), Fraser River plume depth (defined as the depth of the 21 psu isohaline) is found to be 2-4 m at the Fraser River mouth, which agrees with an earlier estimation of the plume depth at 3 m by Cordes et al. (1980) from CTD measurements. Both of these studies were carried out in winters, when the river flowrate is relatively low. On the other hand, in Halverson and Pawlowicz (2011), the plume depth is estimated to be 7 m, and a high degree of salinity variability can reach as deep as 10 m from CTD profiles near the river mouth. Although the exact value of $\bar{D}$ is still unknown, it is reasonable to assume that $\bar{D}$ varies between 2 m and 10 m, which corresponds to a γ ranging from 0.55 to 1.

Additionally, the magnitude of the time derivative of the plume salinity may also be overestimated by the ferry. Since the plume water is strongly stratified, the freshwater spread at the surface can rapidly change the surface salinity. However, the salinity at the bottom of the plume may not change as quickly and vigorously as the surface plume. Therefore, taking $dS_o/dt = 0$,the hourly plume salinity change in tidal cycles can be corrected by γ:

$$\frac{dS_p}{dt} = \gamma\frac{dS_f}{dt} \tag{3.13}$$

However, it is important to keep in mind that, in practice, the stratification of the plume salinity may not be fully linear, and the plume depth may also vary from the river mouth to the plume front. Therefore, although $\gamma = \bar{D}/[2(\bar{D} - z_0)]$ is a reasonable estimation, it may still need to be adjusted according the specific situations when it is applied.

3.6 Tidal Harmonic Analysis on the Surface Currents

Tidal modulation of the surface currents in the southern Strait is important to understanding the dynamical structure of the Fraser River plume. As introduced in Sec. 2.3.3, HF radar derived surface currents can be used for this analysis. In this study, data from year 2018 is found to have the best spatial and temporal coverage, and a tidal harmonic analysis is performed on a 366-day hourly velocity field from Jan 1st, 2018 to Jan 2nd, 2019.

In this procedure, least-squares fits are made to sinusoidal variations at a number of known frequencies which are related to the orbital dynamics of the earth/moon/sun system. Each sinusoidal variation with its unique frequency is called a "constituent". These constituents can then be plotted in terms of elliptical shapes that describe the cyclic rotation of velocity vectors at a particular location, with associated semi-major and semi-minor axes amplitudes which describe the degree to which tidal currents rotate or oscillate back and forth in a single direction given by the ellipse inclination.

In the SoG, tidal currents are found to be along the Strait in most regions. However, near the Fraser mouth, the sinusoidal river flux across the Strait acts on top of the existing tidal currents, which results in more rounded tidal ellipses (Halverson and Pawlowicz, 2016). In this study, an aspect ratio, defined as the ratio of semi-minor axes to the semi-major axes, is used to represent the river influence on the surface tidal currents. Based on the results from major diurnal tidal constituents (K_1, O_1, P_1, and S_1) and major semi-diurnal constituents (M_2, S_2, N_2, and K_2), diurnal tides generally show a much bigger river influence from the Sand Heads all the way across the Strait to the other side, while in the semi-diurnal frequencies, the region with high aspect ratios barely extends past the middle of the Strait (Fig. 3.16).

Therefore, the horizontal structure of the Fraser River plume can be characterized as two distinct dynamical regions: a semi-diurnally modulated "inner plume" which quickly responds to the freshwater input from the river mouth, and a diurnally controlled "outer plume" through which the stronger once-a-day river jet passes.

Recall from Sec. 3.5, the daily drop/jump in S_f around the big ebb/flood of the day is the most dominant feature in the tidal variation (Fig. 3.15). Halverson and Pawlowicz (2008) also find that the ratio of K_1/M_2 to be 2.89 in the plume salinity but only 0.94 in elevation. However, when the time series of S_f is separated into subsets, this big diurnal feature of the plume salinity variation is only found when the river flowrate is relatively low (Fig. 3.15b1, c1). When $\bar{Q}$ is greater than 2400 $m^3\ s^{-1}$, S_f during the small ebb cycle

shows a variation at a similar magnitude as the big ebb cycle (Fig. 3.15b2, c2).

This phenomenon can be partly explained by the proposed plume structure with different regions of diurnal/semi-diurnal influence. When the river flowrate is relatively low, the plume area is smaller. Since the ferry follows about the same route, as the plume size decreases, it is more likely for the ferry to see the feature of the "outer plume", which is more diurnally driven. When the river flowrate is higher (the plume size is bigger), the "inner plume" is a more significant part of the ferry track, and its semi-diurnal feature is then reflected in the observed salinity variation. In short, the diurnal effect of the stronger river jet (during the "big ebb") is more important to the plume section (which the ferry crosses over) when the daily river discharge is relatively low.

3.7 Summary

In this chapter, observational data have been carefully examined to investigate the tidal influence on multiple aspects of the Fraser River plume, from the plume area to the plume salinity and surface currents. First of all, the plume area is found to be negatively correlated to the tidal elevation in the Strait, with near 20% of area increase from low to high water. The daily maximum of the plume area is usually found to be about 1 hour later than the lower-low tide. River discharge has a significant influence on the tide-plume correlations. When the daily averaged river flowrate is relatively low (commonly in fall and winter), the plume area variation is larger over a tidal cycle, with a stronger correlation and a steeper slope in the regression to the tidal elevation. These findings are consistent in two independent methods of the satellite observation, one uses a normalized plume area (R_{AF}) to reduce bias and seasonal signals, and the other uses the plume area change between same-day captured image pairs. To the best of the author's knowledge, this is the first time that the plume area variation has been measured over a tidal cycle.

With a near 20% of area loss twice a day, nearly half of the plume water is mixed into the ambient ocean within a full tidal cycle. At this rate, salt, nutrients and sediments are actively exchanged between the river water and the ocean water. Periodical resizing of the region of high SPM concentration could also affect the local light attenuation, and subsequently, the local primary productivity. Especially when the river flowrate is relatively low (winter months), tidal influence is the dominant factor in the short-term plume variation, and tides control the mixing of the surface water out of the Fraser River mouth.

The plume salinity is found to vary 15-16% during tidal cycles. Although seasonal vari-

ations in the plume salinity have been investigated previously (Halverson and Pawlowicz, 2011), my results show the variability in tidal frequencies, which also indicates a vibrant exchange of salt between the plume water and seawater within short time intervals. Tidally modulated entrainments may play an important part in the dynamics of the plume body.

Unlike open-ocean plumes, the Fraser River plume is located in the semi-enclosed Strait of Georgia, which limits the development of the mid-field and far-field plumes that have been the subject of much previous work (e.g., Horner-Devine et al., 2015; Hetland and Hsu, 2013; Chant, 2012). Therefore, the conventional dynamical scheme for the horizontal structure of a plume may not apply in this area. However, tidal harmonic analysis on the surface currents in the Strait reveals a significant difference in the extent of diurnal/semi-diurnal driven river influence. This may offer us a new perspective in dividing the Fraser River plume into two distinct dynamical regions: a diurnally driven "outer plume" that is largely affected by the "big ebb" of the day, and a semi-diurnally driven "inner plume" where the "big ebb" and "small ebb" are equally important.

These new findings provide us a deeper understanding of the behaviour of Fraser River plume under tidal periods. However, the reason for this tidal modulation on the plume area is still not clear, and the dynamics of the tidal influence on the seawater entrainment in the Fraser River plume is still not known. In the next chapter, a simple semi-analytical diagnostic model is developed to further investigate the dynamics of the tidal influence on the Fraser River plume.

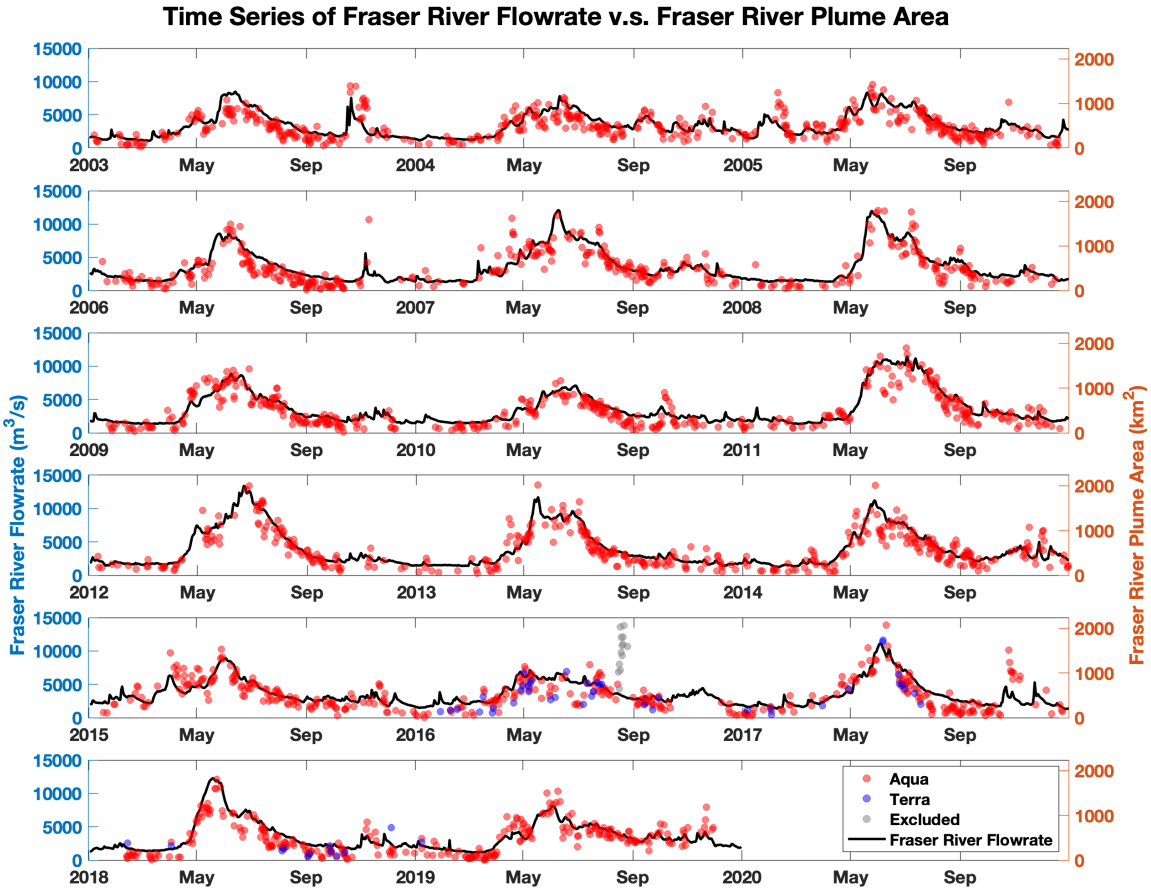

Figure 3.1: A time series of the Fraser River flowrate vs Fraser River plume area from 2003 to 2019. Red dots are the plume areas calculated from images aquired from Aqua mission, while blue dots are from Terra mission. Abnormally big plumes (grey dots in August 2016) are due to a rare coccolithophore bloom, and are excluded from further analysis.

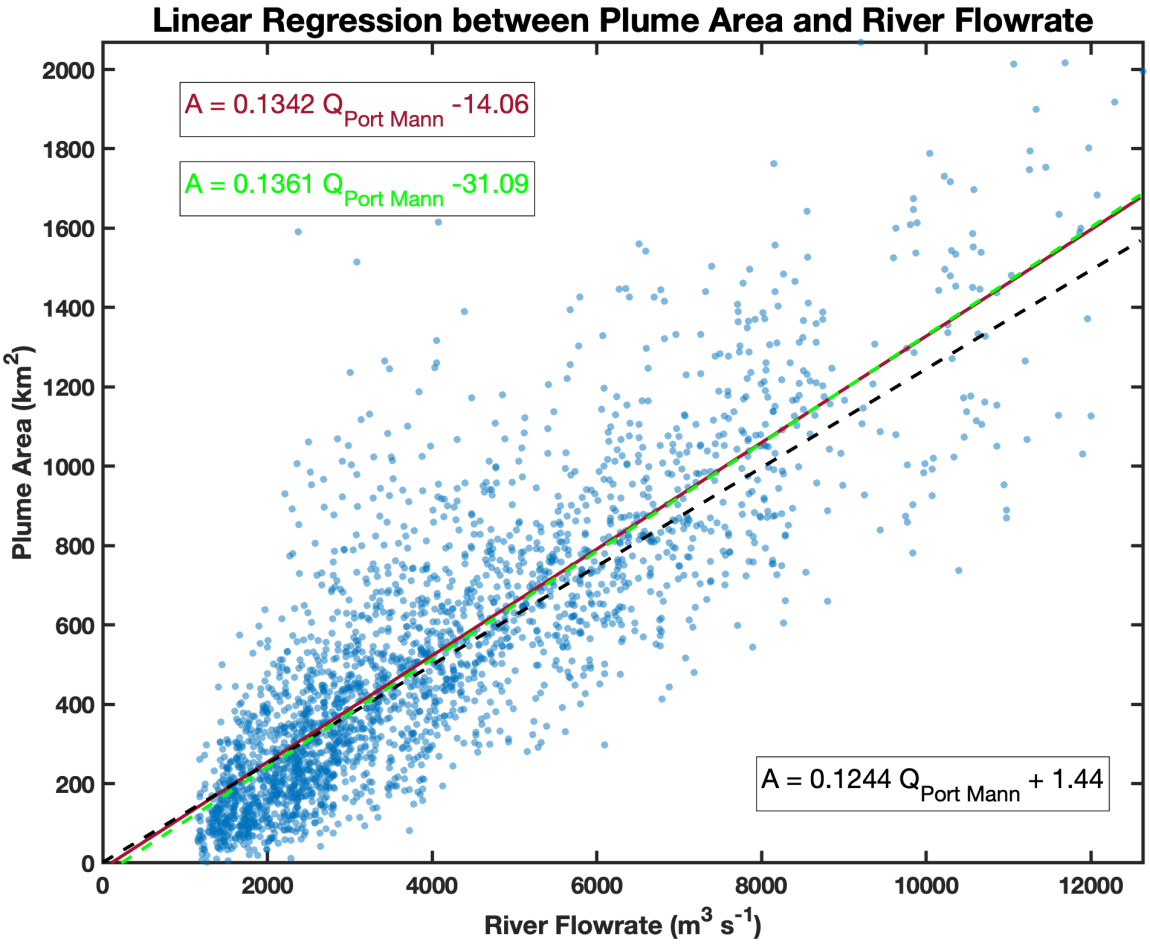

Figure 3.2: Linear regression (solid curve and equation in red) of the plume area and the Fraser River flowrate based on expanded image collection (scattered as blued dots). As a comparison, a similar equation from Pawlowicz et al. (2017) based on a smaller image collection is shown as dashed black curve, its equation is written in black colour underneath the curve. Based on a cross-correlation analysis of the two time series, a 3-day lag of plume area to the river flowrate is found to give the best regression result. This correlation relationship is then shown in green dashed curve and green equation in the figure.

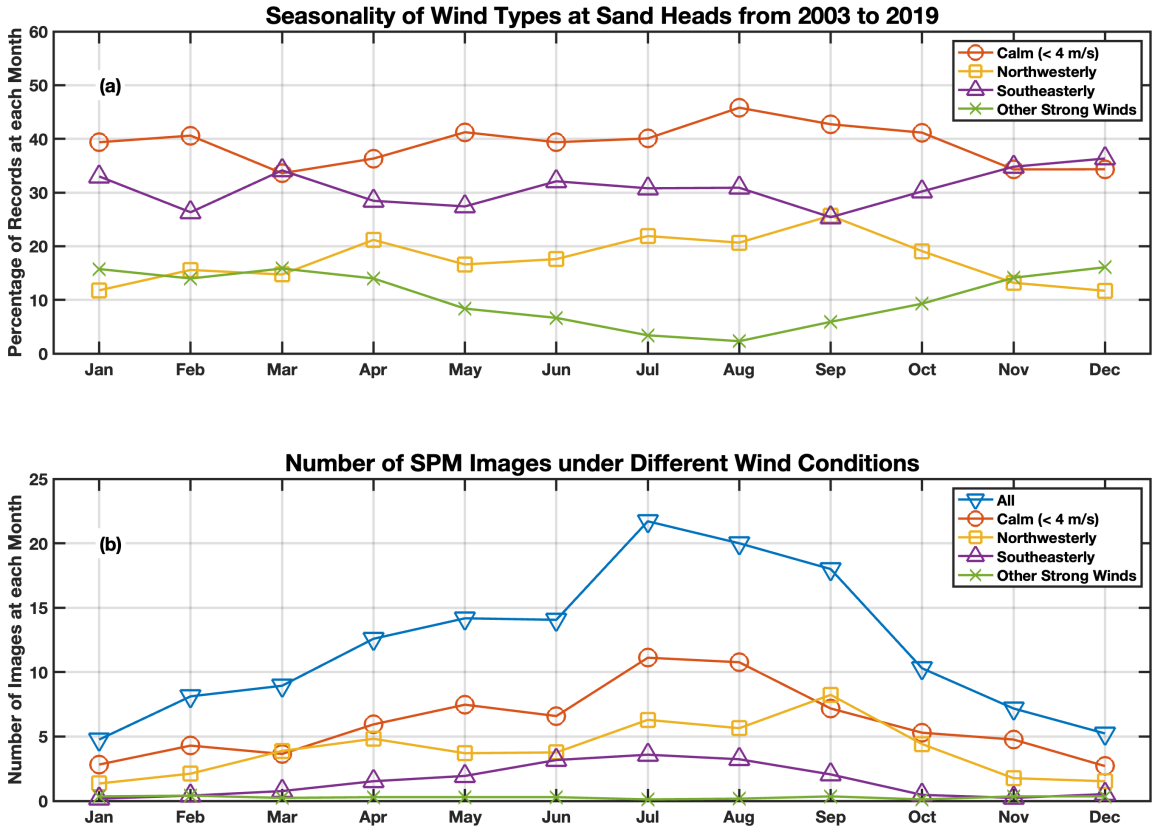

Figure 3.3: (a) Percentage of recorded wind data at each month under different wind conditions from Sand Heads, 2003 - 2019. (b) Monthly distribution of the number of selected SPM images under different wind conditions.

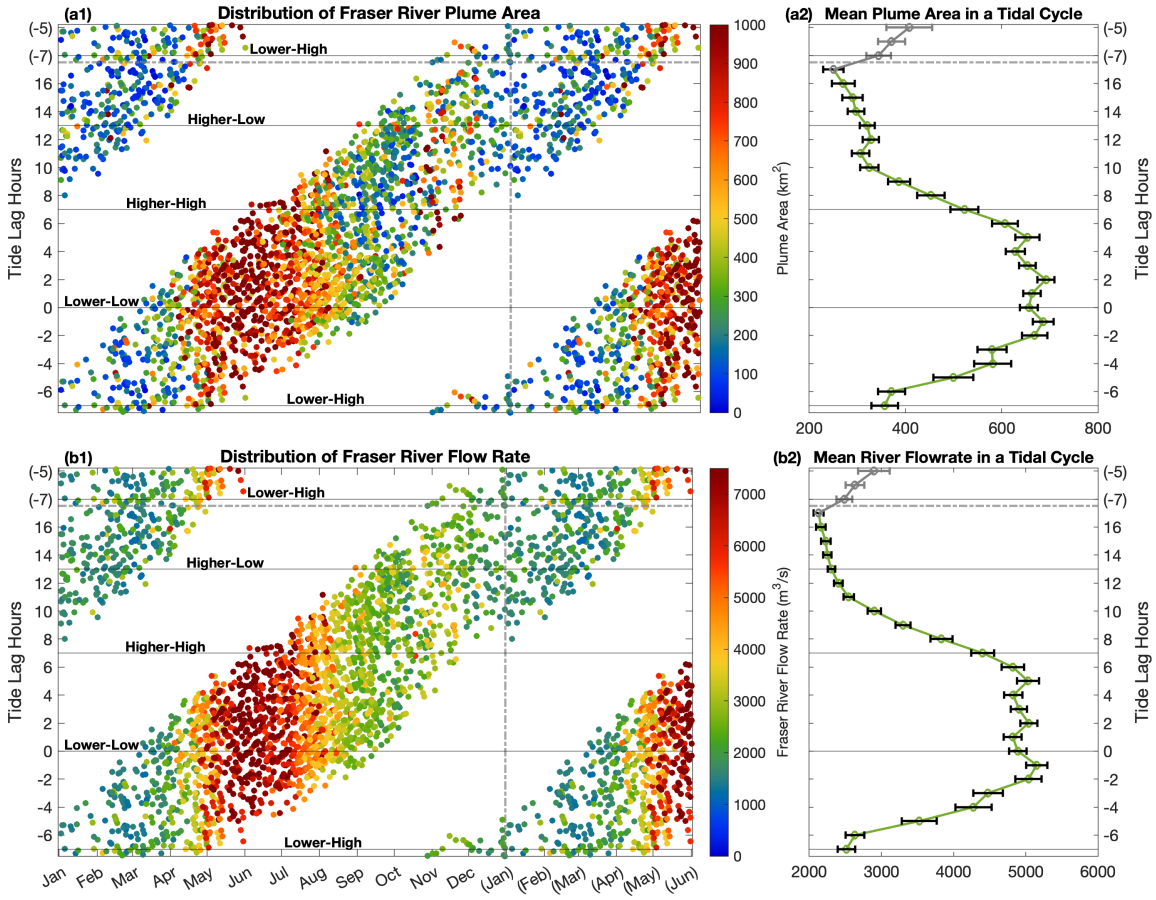

Figure 3.4: (a1) Scatter plot of the Fraser River plume area over tidal and seasonal cycles. Referential tide peaks (Tidal lag hour = -7 for lower-high tide, 0 for lower-low tide, 7 for higher-high tide, 13 for higher-low tide) are labelled with thin black lines. Dots right of or above the dashed grey lines are the duplicated data points to better visualize the winter transition of plume area over tidal cycles. The corresponding horizontal and vertical tick-labels for these duplicates points are marked with braces. (a2) mean plume area over a tidal cycle (green curve) with standard error of mean as error bars (duplicated data to the right of the dashed grey line in (a1) are excluded, while duplicated data above the dashed grey line are included and were averaged using grey curves with grey error bars). (b1) and (b2) are the same as (a1) and (a2), but for the river flowrate data. Note that the flowrate is upstream of tidal influence.

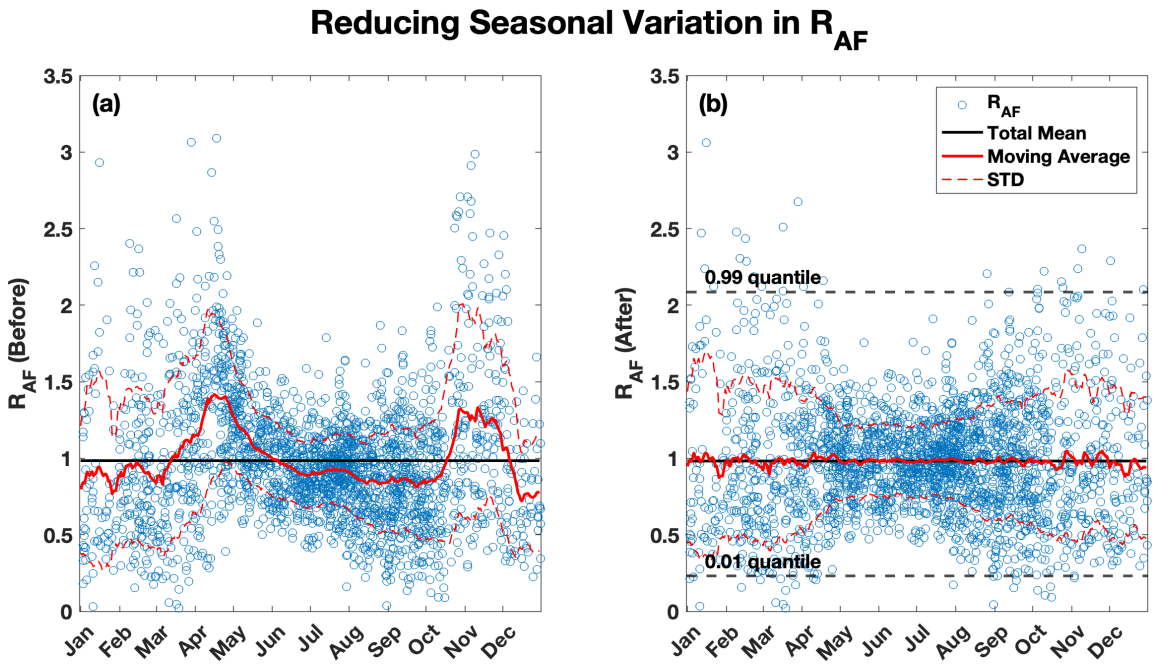

Figure 3.5: (a) moving averages of R_{AF} in a seasonal cycle with a 1-day step size and a $\pm$ 10-day window size. (b) similar to (a), but the original R_{AF} is divided by the ratio of its nearest daily moving average to its global mean to further reduce seasonal signals in the data. Data points that fall below the 0.01 percentile and above the 0.99 percentile are excluded from further analysis.

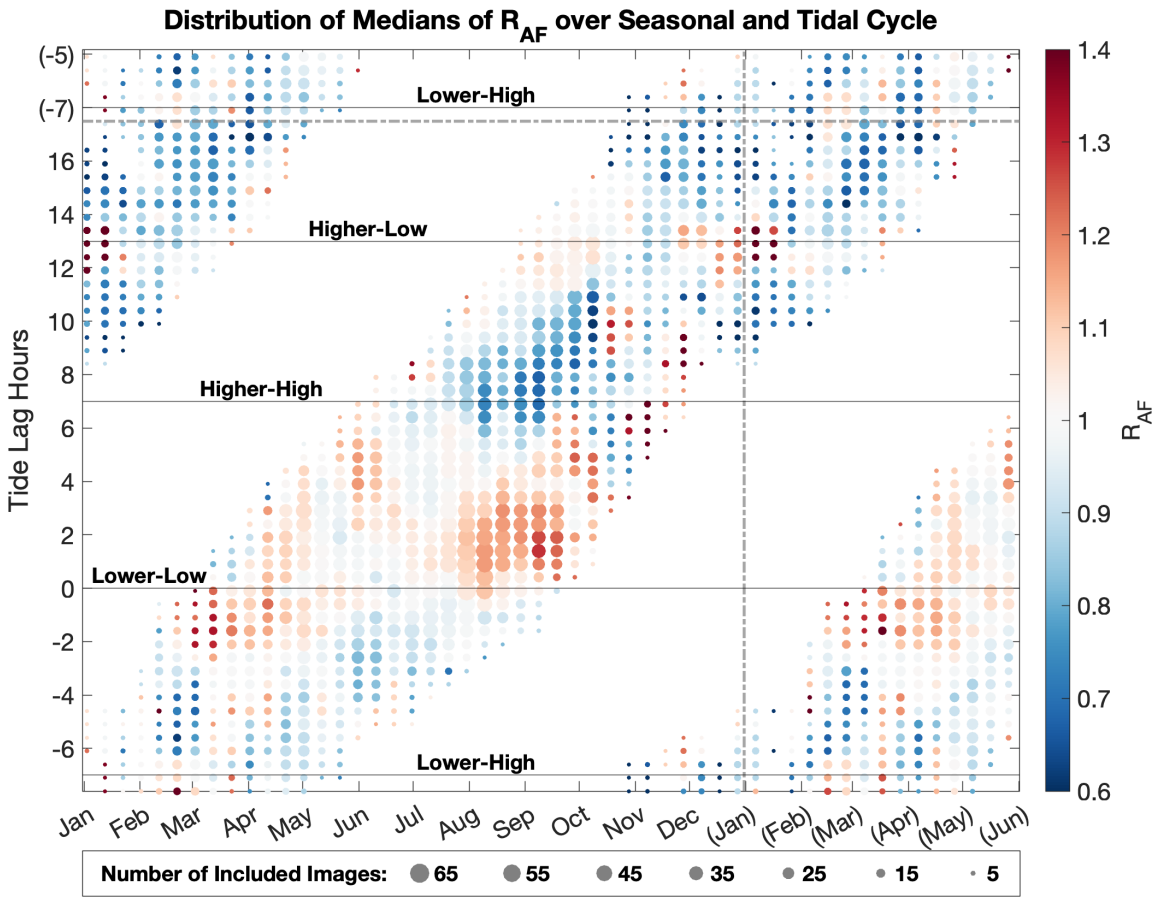

Figure 3.6: Regional medians of R_{AF} values are plotted onto a grid stepped by 10 days in the horizontal axis (seasonal cycle) and 0.5 hours in the vertical axis(tidal cycle). Colour of the dots shows the median value of the data points within $\pm$ the step size of each grid point, and the size of the dots represent the number of data points being averaged. Blue/red colour means that the plume area is smaller/larger than its daily average.

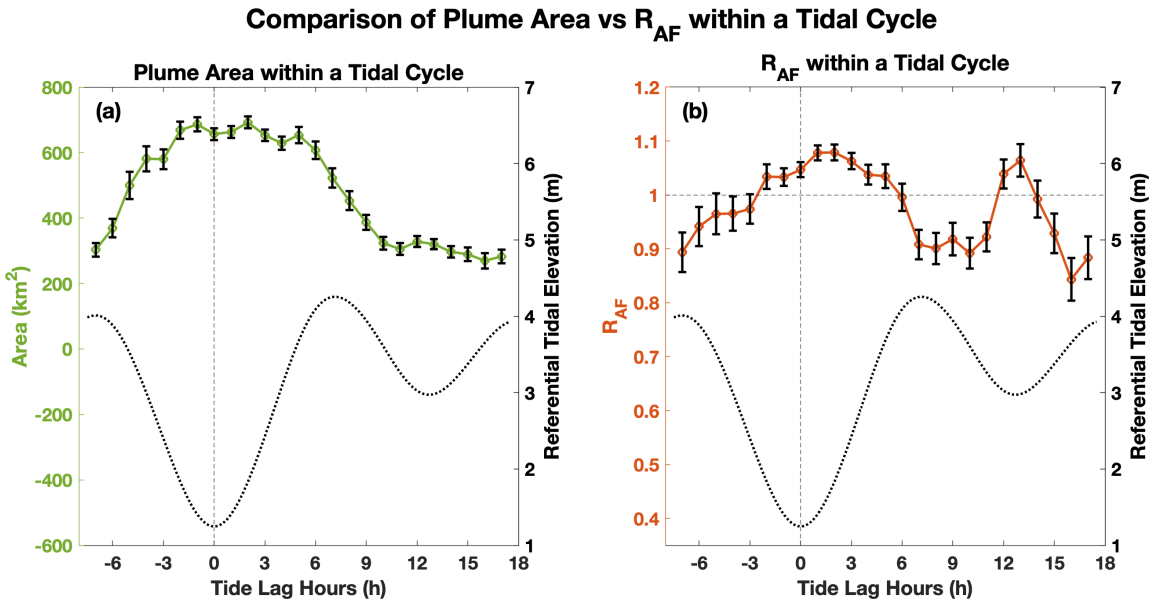

Figure 3.7: (a) Strongly biased result of the plume area over a tidal cycle (same information as in Fig. 3.4 (a2)). (b) Corrected result from R_{AF} over a tidal cycle. Standard error of mean is added as error bar on both subplots. Referential tidal elevation curve of the day is added at the bottom.

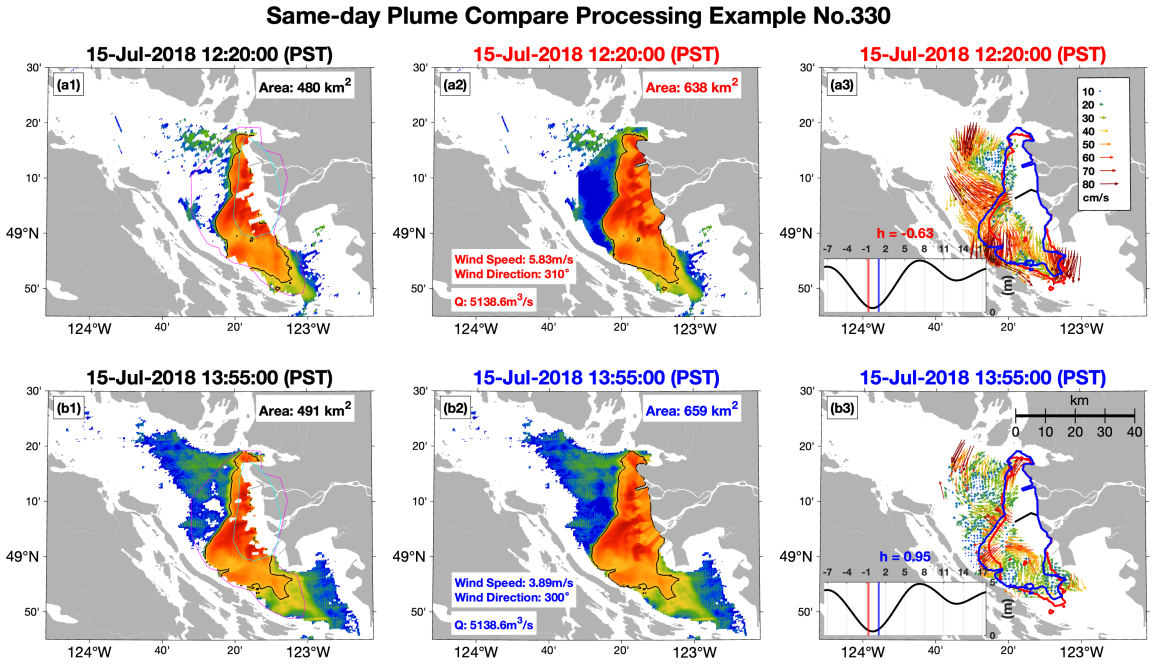

Figure 3.8: Example of image processing and data comparison for the same-day image pairs. Upper panels (a1 to a3) are for the first image of the pair (12:20 PST), while the lower panels (b1 to b3) are for the second image (13:35 PST), both images are taken in the same day on July 15th, 2018. Left panels (a1 and b1) are for the original SPM image before processing. Magenta contours are manually drawn to define the approximate outer boundary of the plume region, while the inner cyan contours are used for cleaning the abnormally low-reflectance small patches inside the plume. Note that the same outer and inner mask contours were applied to both images in this paired group. Middle panels (a2 and b2) show the images after cleaning and interpolation, together with information of plume area, wind and river flowrate (Q). Wind direction is defined as angle of the origin of the wind clockwise from the north. Right panels (a3 and b3) show a comparison between plume boundaries (red for the first image while blue for the second). HF-radar derived surface currents are added underneath the plume contours (surface currents at 12:00 PST are used for (a3) and at 14:00 are used for (b3)). Relative lag hours in a tidal cycle for the paired plume image are shown at the lower-left corner of the plots. Legend for the magnitude of surface current vectors is added on (a3) and the ruler for the length scale is added on (b3).

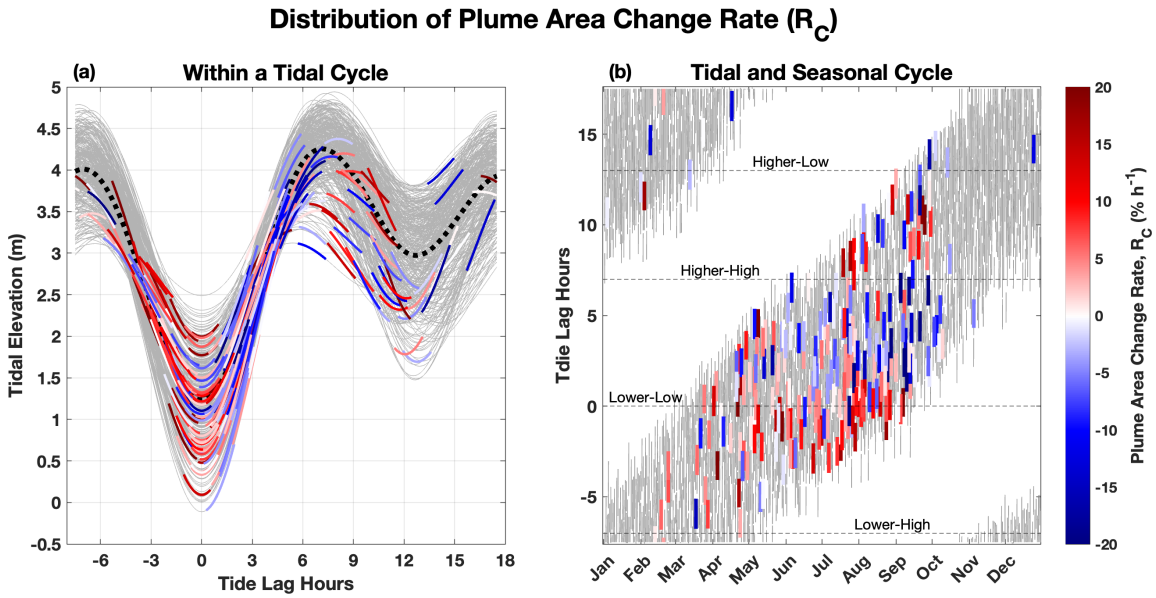

Figure 3.9: Distribution of the plume area resizing rate (R_C) within a tidal cycle (a) and in a tide-year 2-D distribution (b). In (a), daily tidal cycles are plotted in grey curves, with a mean tidal elevation in thick dashed black line. Short thick lines with colours in blue to red are for the percentage of area change per hour (R_C) between each grouped SPM image pairs. Same concept for (b), in which all 3300 potential same-day pairs are drawn in thin grey lines showing the start and end times for each pair, and 247 good pairs are used to calculate the area change rate and were plotted in thick lines with colour ranging from dark blue to dark red. Referential tidal peaks are added on (b), as in Fig. 3.4, 3.4 and 3.6

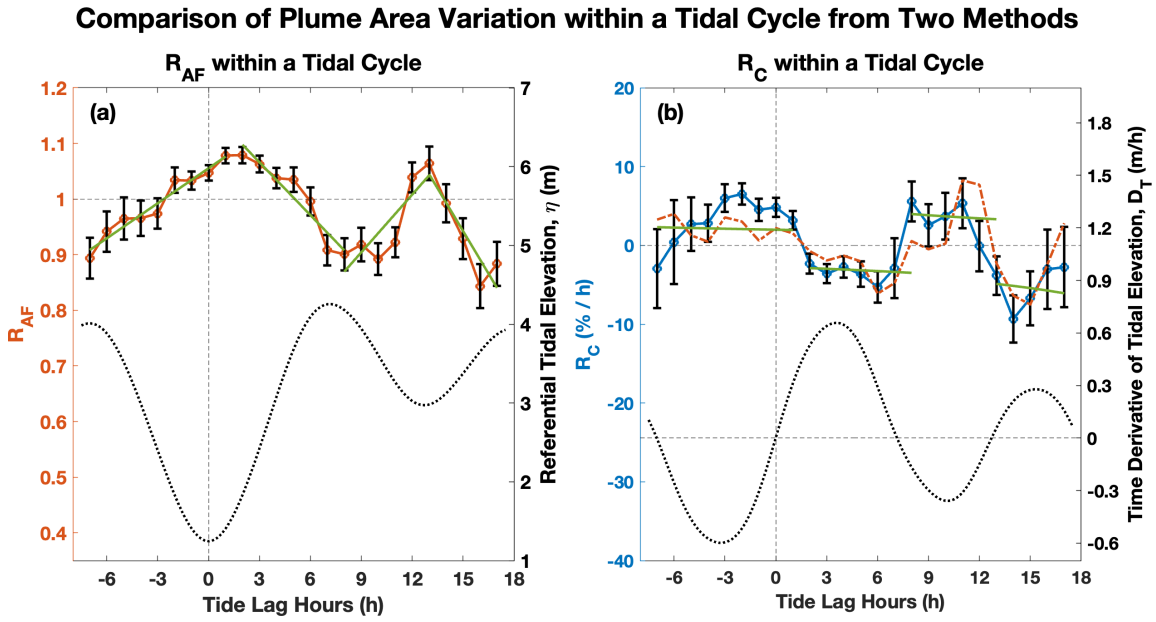

Figure 3.10: Comparison of the plume area variation from the mean R_{AF} among all SPM images (a) and the change rate (R_{C}) from same-day image pairs (b) in a tidal cycle. (a) is the same as shown in Fig. 3.7, with a approximated regional linear regression (green lines) on top of the pattern of R_{AF} variation within a tidal cycle. For (b), R_{C} in a tidal cycle is drawn in a blue curve with black errorbars showing the standard error of mean. Calculated percentage of hourly R_{AF} variation ($\frac{1}{R_{\mathrm{AF}}}\frac{dR_{\mathrm{AF}}}{dt}100\%$, i.e., the time derivative of the red and green curves divided by value from (a)) are shown in (b) with the same colour as in (a). Instead of a referential tidal elevation shown in (a), the time derivative of tidal elevation (D_{T}, m/h) is used as a reference to R_{C}.

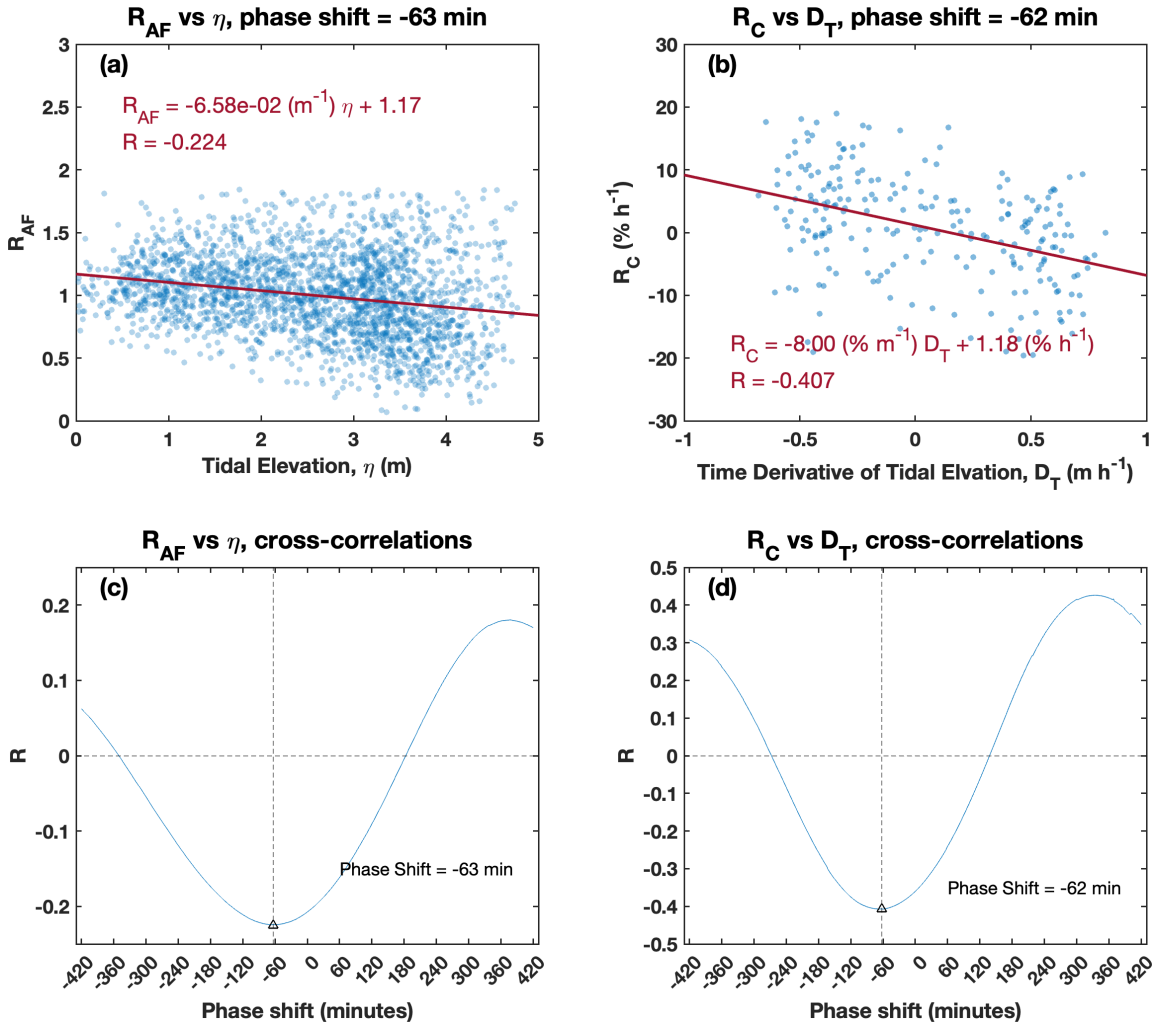

Figure 3.11: (c) Cross-correlations between the normalized plume area (R_{AF}) and tidal elevation at Pt. Atkinson (η), and (a) the linear regression at the minimum correlation coefficient (phase shift at - 63 minutes). Same concept in subplot (d) and (b) for the cross-correlation between the plume area change rate (R_{C}) and the time derivative of tidal elevation (D_{T}), with a best correlation at phase shift = - 62 minutes.

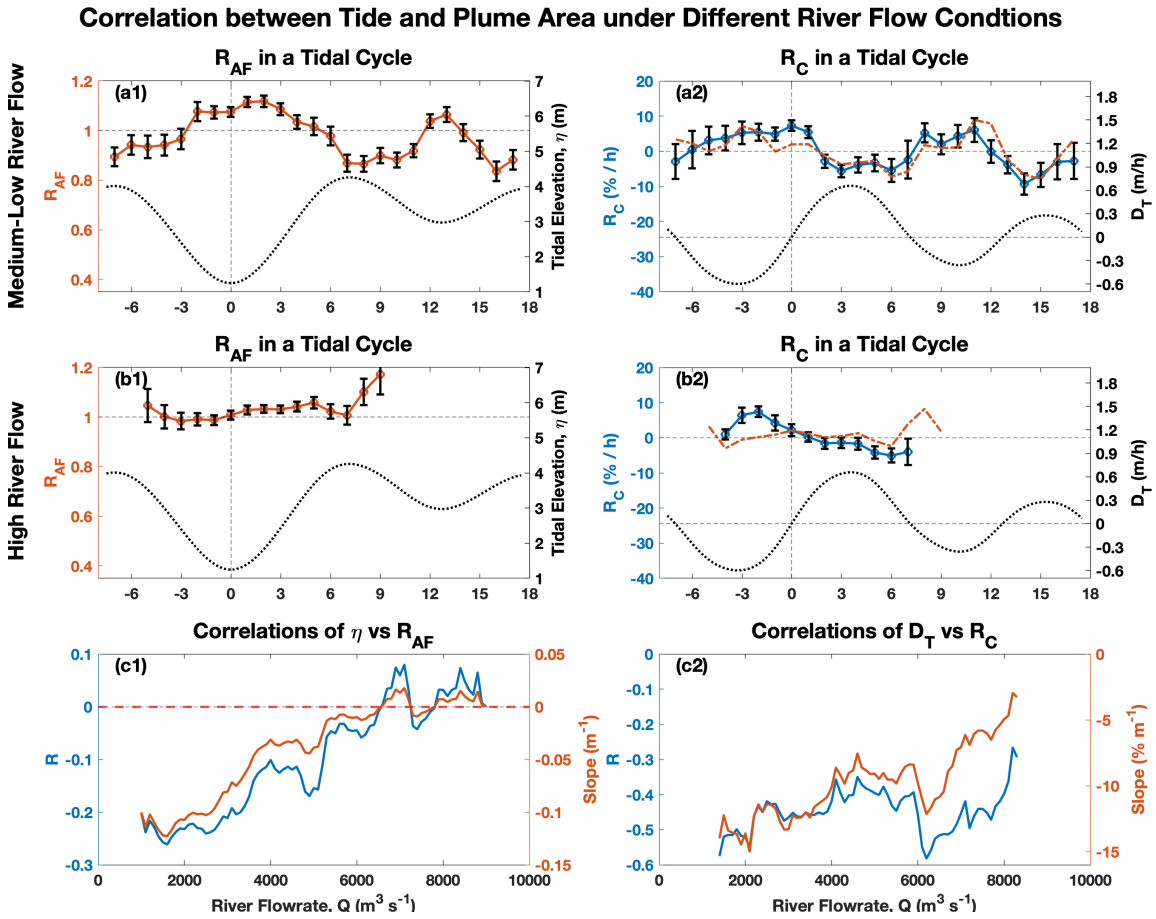

Figure 3.12: (a1) and (a2) are similar to Fig. 3.10, but for the medium-low river flow condition ($\bar{Q} < 5000$ m^3 s^{-1}). (b1) and (b2) apply the same approach for high river flow condition ($\bar{Q} > 5000$ m^3 s^{-1}). In (b1) and (b2), hourly R_{AF} with less than 10 valid SPM images and hourly R_{C} with less than 3 valid same-day pairs are not shown. (c1) Correlation coefficients (left axis) and slopes (right axis) for the linear regression between tidal elevation (η) and normalized plume area (R_{AF}) for continuous subsets of the SPM images with incremented river flowrate. (c2) correlation parameters for D_{T} and R_{C}.

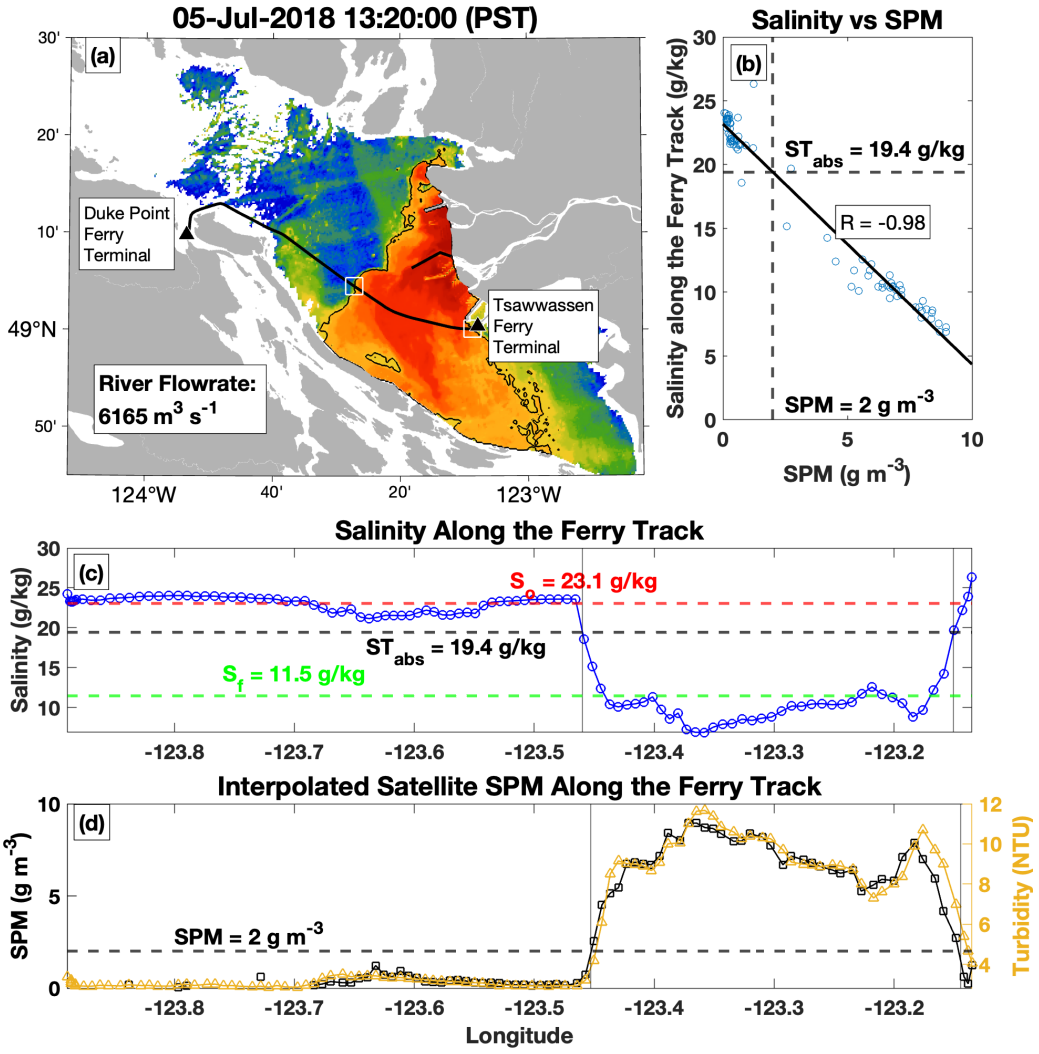

Figure 3.13: (a) SPM image at 13:20, July 5th, 2018 (PST), and its nearest ferry track in time (departed from Duke Point Terminal at 11:50 (PST) and arrived at Tsawwassen Terminal at 13:40 (PST)). White square boxes are drawn to show the intersection points between the ferry track and the plume boundary in the SPM image. (b) linear correlation between the satellite observed SPM concentration and the salinity measured along the ferry track with a correlation coefficient of -0.98. An absolute salinity threshold ($ST_{\text{abs}} \sim 19.4$ g/kg) is calculated at SPM $= 2$ g m^{-3}. (c) salinity along the ferry track, with the calculated salinity threshold (ST_{abs}), ambient ocean salinity (S_{o}), and the weighted ferry-measured plume salinity (S_{f}). Plume boundaries are shown as thin black lines at the intersections between ST_{abs} and the along-track salinities. (d) interpolated SPM concentration from the SPM image onto the ferry track (black curve with square markers). Intersections to the SPM $= 2$ g m^{-3} threshold is shown in thin black vertical lines (same locations at the white square boxes in (a)). To show the good match between satellite-based SPM concentration and the surface turbidity measured by the ferry, a yellow curve with triangle markers are added in this plot to show the ferry-measured turbidity values.

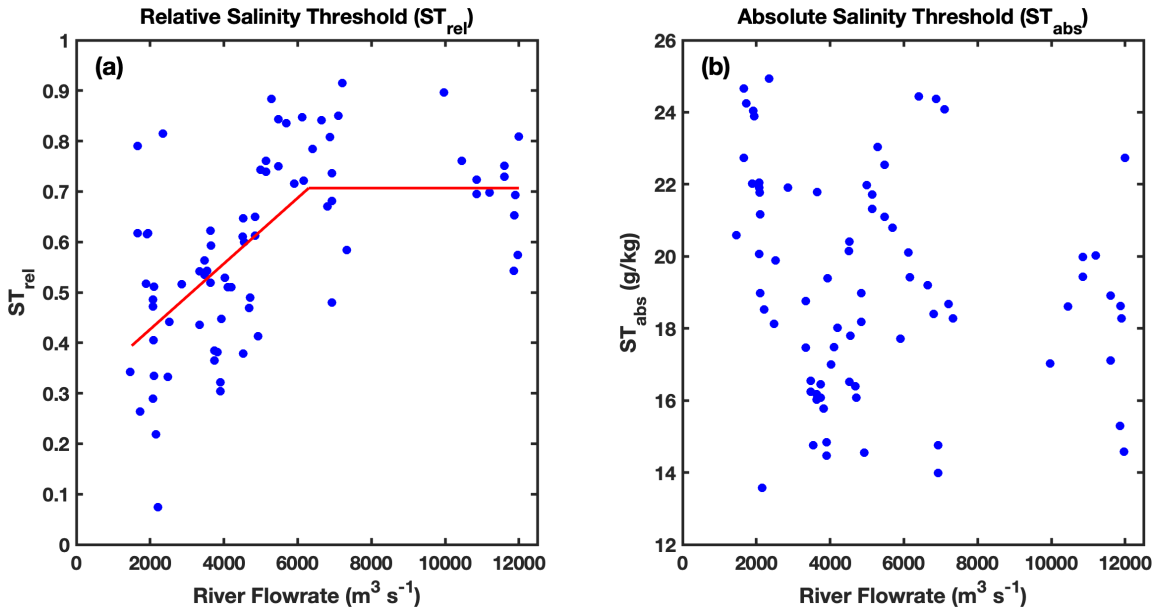

Figure 3.14: (a) relative salinity threshold (ST_{rel}, according to Eq. (3.7)) for the examined 82 examples in 2018 against river flowrate. A segmented linear correlation of ST_{rel} is shown as a thick red curve. (b) absolute salinity threshold (ST_{abs}).

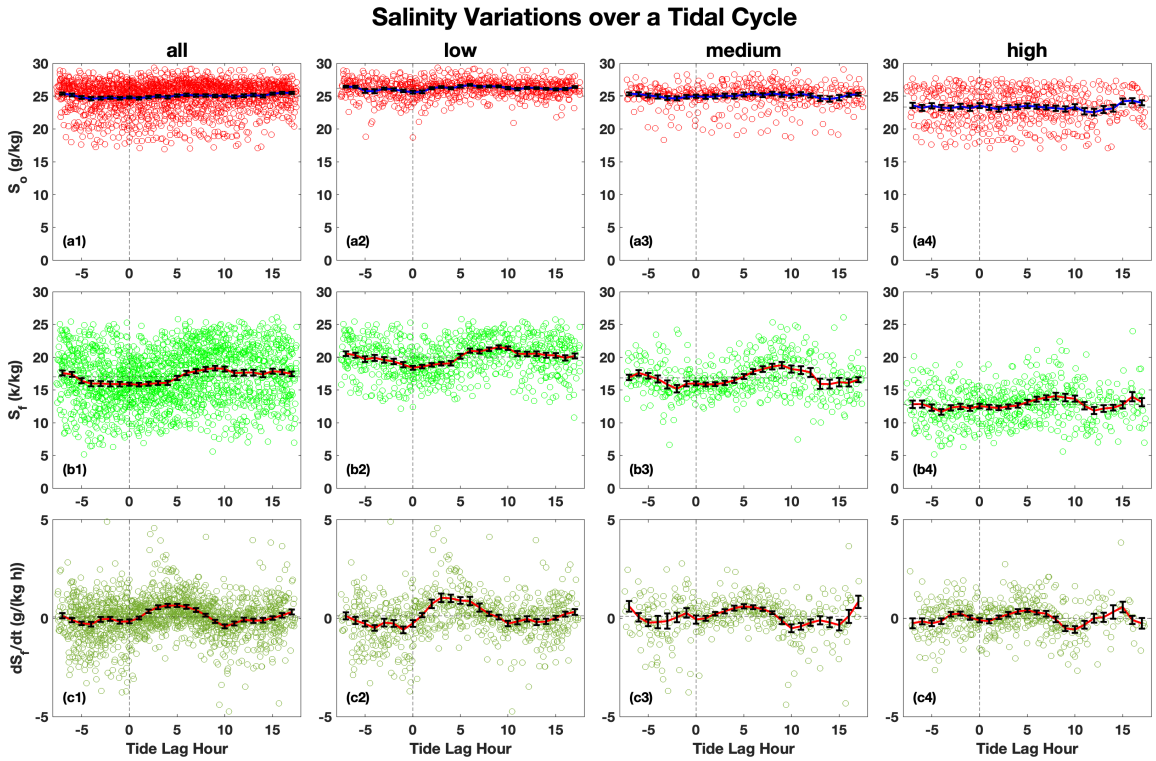

Figure 3.15: (a1-a4) tidal variations of the ambient ocean salinity (S_o) for four river flow conditions: all, low ($\bar{Q} < 2400$ m^3 s^{-1}), medium (2400 m^3 s^{-1} $< \bar{Q} <$ 5000 m^3 s^{-1}), and high ($\bar{Q} > 5000$ m^3 s^{-1}). (b1-b4) for ferry-measured plume salinity (S_f). (c1-c4) for the time derivative of S_f (dS_f/dt), calculated based on the S_f change rate between consecutive ferry tracks. Standard error of means are used as error bars on top of the hourly average salinities.

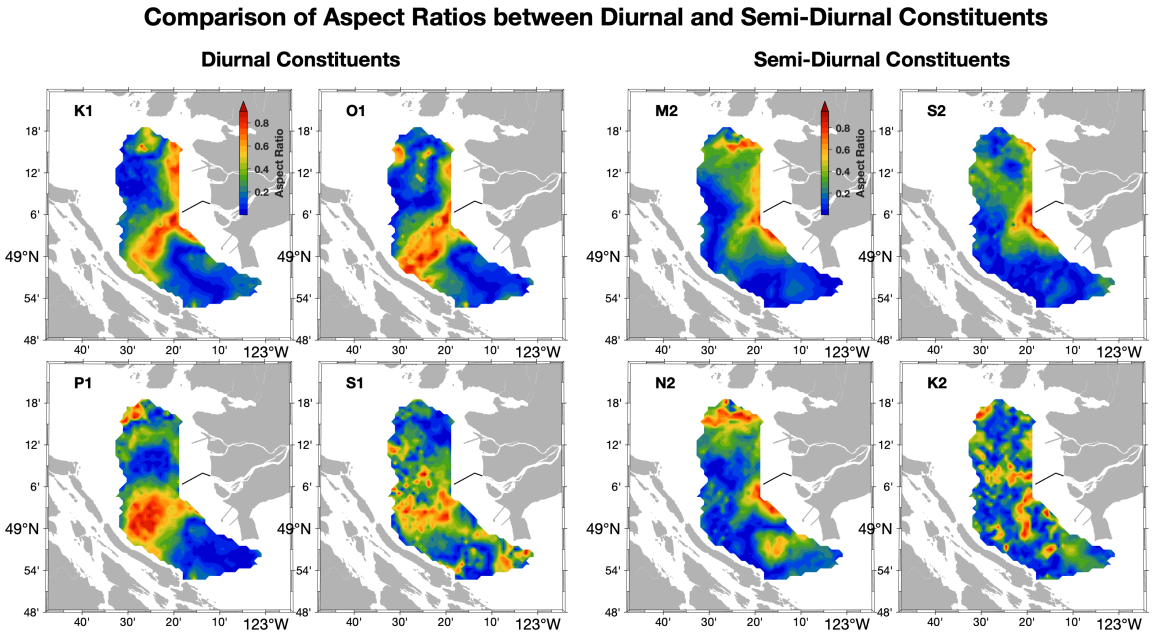

Figure 3.16: Distribution of the aspect ratio (defined as the ratio of the absolute values of the semi-major axes to the semi-minor axis of the tidal ellipses) between major diurnal constituents (K_1, O_1, P_1, and S_1) and major semi-diurnal constituents (M_2, S_2, N_2, and K_2) in the Strait.

Chapter 4

A Simple Model of Plume Dynamics

Observational results of the Fraser River plume show a variety of interesting tidal features from the plume area and salinity to the surface currents. However, the mechanism of the tidal forcing on the plume area is still unclear. To explain and reproduce the plume area variation over a tidal cycle, a simple semi-analytical diagnostic model is constructed in the following sections, and its applicability under various river flowrate conditions is investigated.

4.1 Analytical Solutions based on the Tidally Modulated Freshwater Input

Considering the Fraser River plume as a reservoir of freshwater in the Strait of Georgia, its volume is mainly controlled by the water inputs, outputs, and the fraction of freshwater in the system. From Sec. 3.5, the plume salinity is found to increase about 15-16% during the daily big flood. If the amount of freshwater is conserved in the plume system, a higher salinity will lead to a lower fraction of freshwater, which means a bigger volume of the plume. However, on the contrary, the plume area is found to decrease during flood tides. Therefore, the salinity variation alone is not able to explain the observed tidal modulation on the plume area. The volume flux of the water input/output to the plume must be an important factor.

The volume flux of a plume system generally consists three main parts: the rate of freshwater input (from the river discharge), seawater entrainment (at the bottom of the plume), and the plume water exit (by mixing into the rest of the Strait at the plume front):

$$\frac{dV_{\mathrm{p}}}{dt} = Q + w_{\mathrm{e}}A - F_{\mathrm{f}} \tag{4.1}$$

where Q is the river flowrate, $w_e A$ is the upward entrainment rate, and F_f is the rate of plume water loss at the front. A schematic diagram (Fig. 4.1) of the plume shows the relationship between these factors. From earlier introduced model outputs at Steveston (Sec. 2.3.1, Wu et al. (2022)), the fluctuation of the river flowrate is clearly modulated by tide (Fig. 2.6), with a strong correlation to the time derivative of the tidal elevation (D_T)[8]. Note that the numerical model which is the source of this information is run in a barotropic mode, and it does not take account of the salt-wedge induced friction and salinity variation at the river mouth. Therefore, this estimated hourly (or "minutely", after interpolation) river flowrate theoretically reflects the rate of freshwater input into the Strait.

In a tidal cycle, although the derived river flowrate seems to be negatively correlated to the tidal elevation (Fig. 4.2), a comparison in the time series shows that the flowrate is actually better correlated to the time derivative of the tide elevation (D_T) with a small phase delay (Fig. 2.6). This correlation with D_T means that the maximum daily outflow occurs shortly after the middle of the big ebb, at which time the southward tidal current in the Strait is about the strongest. This alignment of the maximum outflow around the midebb is also found in McCabe et al. (2009), in which the model simulated surface elevation and velocity at the Columbia River mouth are compared.

Under the low flowrate condition, the river water empties into the plume at a much higher rate during ebb tides than the daily average rate, while during flood tides, the plume water is drawn back into the river channel. In Horner-Devine et al. (2009), the estuary discharge for the ebb tides at the Columbia River mouth is found to be more than 4 times the averaged river discharge, which is similar to the model results shown here (about six times of the mean daily flowrate, Fig. 4.2a). For the medium flowrate condition, river water rarely goes upstream, but the freshwater flux can be as low as zero after the middle of the big flood. When the river flowrate is high, tidal impact on the flowrate variation is much smaller, the river water discharges into the plume at a high and stable rate.

Theoretically, in a short period of time, the bigger the river flowrate, the more freshwater is injected into the plume, therefore, the faster the plume grows. When the river flowrate is higher/lower than its daily average, the plume size tends to increase/decrease.

[8]Note that in Sec. 2.3.1, the hourly river flowrate is derived from the depth-averaged eastward velocity and meridional river transect area, the positive values are for the flux upstream (estward) into the river channel. This hourly flowrate nicely shows a positive correlation to D_T with a phase delay of about 2-3 hours in Fig. 2.6. However, in our model set-up, the freshwater input (Q) enlarges the plume size, which is an overall positive term. Thus, hereafter, we switch the sign of the flowrate data as shown in Sec. 2.3.1, with the positive values in Q to be the flowrate from the river to the plume.

From the earlier sections, an increasing/decreasing plume area under ebbing/flooding tides is found, and the rates of the plume area resizing is also negatively correlated to D_{T} with a small phase delay, both of which agree with the pattern of the river flowrate in a tidal cycle.

The overall agreement between the tidal cycle of the plume area variation and the river flowrate variation at the mouth yields a qualitative explanation of the mechanism of the plume resizing resulting from the tidal fluctuation on the freshwater input. Furthermore, we can quantitatively simulate this tidally modulated plume area variation.

First, the plume needs to be idealized. In Halverson and Pawlowicz (2011), the Fraser River plume was simplified as a cylinder-shaped single-layer slab water with a uniform thickness. However, the plume water is usually fresher near the river mouth and saltier at its peripheral. Therefore, it is reasonable to assume that the plume depth is thicker at its centre and thinner at its edge. This assumption agrees well with the field observation of the Fraser River plume depth by Kastner et al. (2018), in which the plume depth is defined as the depth of the 21 psu isohaline, and this depth is found to decrease almost linearly away from the river mouth. Therefore, in this study, the plume is re-constructed to be an upside-down semi-cone with the deepest point (D) at the river mouth and the shallowest line at the plume front (Fig. 4.1). The plume volume (V_{p}) is then characterized by the surface area (A) and its depth at the river mouth (D):

$$V_{\mathrm{p}} = \frac{1}{3} AD \tag{4.2}$$

As described by Eq. (4.1), the plume gains its volume from both the freshwater input by the Fraser River and the entrainment of seawater at the base of the plume, while it loses its volume as the plume water is entrained out of its front. At the same time, the upward entrainment of seawater brings salt into the plume, while the exiting plume water at its front takes salt away from the system. A salinity budget can then be established as:

$$\frac{d(\rho_{\mathrm{p}} S_{\mathrm{p}} V_{\mathrm{p}})}{dt} = \rho_{\mathrm{o}} w_{\mathrm{e}} A S_{\mathrm{o}} - \rho_{\mathrm{p}} F_{\mathrm{f}} S_{\mathrm{p}} \tag{4.3}$$

where S_{p} and S_{o} are the salinity for the plume water and ambient ocean water, ρ_{p} and ρ_{o} are their densities. Ignoring the very small difference in the density between the plume water and seawater, the density terms can then be dropped from Eq. (4.3). Next, Eq. (4.1) and (4.3) are combined to eliminate the loss terms associated with F_{f} (the right-most term for both equations). Finally, the l.h.s term in Eq. (4.3) is expanded using the product

rule, and Eq. (4.2) is substituted to replace V_p. The balance of the plume salinity can then be expressed as:

$$\frac{dS_p}{dt} = -\frac{3Q}{AD}S_p + \frac{3w_e}{D}(S_o - S_p) \tag{4.4}$$

Rearranging the equation above, the following formula is derived to calculate the rate of upward entrainment (w_eA):

$$w_eA = \underbrace{\frac{DA}{3(S_o - S_p)}\frac{dS_p}{dt}}_{\text{term1}} + \underbrace{\frac{QS_p}{S_o - S_p}}_{\text{term2}} \tag{4.5}$$

In this case, w_eA is determined by two terms, both of which vary with the tide. In term 2, tidal variability is dominated by Q since its daily tidal variation ($\sim \pm$ 75% on average) is much bigger than that of S_p ($\sim \pm \gamma\times$8%, where γ is slightly less than 1, see Sec. 3.5). In term 1, tidal variation brings a $\sim \pm$ 10% variability to A around $\bar{A}$. However, dS_p/dt averages to 0 and changes sign throughout a tidal cycle, which leads to a daily oscillation from about - $|\text{term 1}|_{\max}$ to + $|\text{term 1}|_{\max}$. It is clear that dS_p/dt dominates the tidal variation in the term 1, and the tidal variabilities in A and S_p are insignificant to this term. Specifically for this analytical solution, we aim to reproduce the tidal variation in A simply based the tidal variation in Q and S_p (dS_p/dt), therefore, A in the r.h.s. of Eq. (4.5) is replaced by $\bar{A}$ in further calculations.

Theoretically, during the ebb tides, Q is bigger than its daily average, which increases the magnitude of term 2. At the same time, the plume salinity tends to decrease as more freshwater is injected into the system, which leads to a negative dS_p/dt and a consequent decrease in the term 1. From this reasoning, tidal variations in the w_eA are expected to be reduced as its two components work counter to each other.

Defined as the rate at which plume waters leave through the front, F_f is theoretically proportional to the plume front length (i.e., $F_f \propto \sqrt{A}$). According the earlier reasoning, tidal variation of A is usually much smaller than that of Q, and it is also a less significant part in w_eA. Therefore, the variation of F_f over a tidal cycle is also expected to be reasonably small compared to Q and w_eA. In this study, F_f is assumed to be a constant throughout the tidal cycle, and its value is determined by the sum of $\bar{Q}$ and $\overline{w_eA}$. Then, the plume area change rate can be easily estimated from Eq. (4.1) and (4.2):

$$\frac{1}{\bar{A}}\frac{dA(t)}{dt} = \frac{1}{\bar{V}}\frac{dV_{\mathrm{p}}(t)}{dt} = \frac{3(Q(t) + w_{\mathrm{e}}A(t) - F_{\mathrm{f}})}{\bar{A}D} \tag{4.6}$$

where $Q(t)$[9] is the hourly river flowrate at the Fraser mouth, and $w_{\mathrm{e}}A(\mathrm{t})$ is the derived upward entrainment variation over a tidal cycle from Eq. (4.5). This plume area change rate from Eq. (4.6) is essentially the same as the R_{C} calculated from the same-day SPM image pairs. Furthermore, an integral of this equation yields the plume area variation over a tidal cycle to be:

$$A(t) = A_0 + \frac{3}{D}\int_{t_0}^{t}(Q(t) + w_{\mathrm{e}}A(t)) - \frac{3F_{\mathrm{f}}(t - t_0)}{D} \tag{4.7}$$

where t_0 is the start time of a tidal cycle at tide lag hour = -7.5 h, and $A_0 \sim \bar{A}$ is the initial plume area at t_0, which can be estimated according to $\bar{Q}$ using Eq. (3.3). Since a typical tidal cycle in this study starts at the lower-high tide of the day, at which time the plume area is relatively small compared to its daily average, A_0 is usually a few percent smaller than $\bar{A}$. In theory, dividing $A(t)$ from the Eq. (4.7) by $\bar{A}$ should result in a comparable time series in tidal cycles as calculated R_{AF} in Sec. 3.3.

4.2 Base Case Study: Entrainment Flux Estimations and Plume Area Simulations

In the first case study, we aim to reproduce the averaged plume area variation during the tidal cycle. For all SPM images in use, the median river flowrate ($\bar{Q}$) on the days when these images are taken is around 3,500 $\mathrm{m^3\ s^{-1}}$, which corresponds to a median plume area ($\bar{A}$) of 432 $\mathrm{km^2}$ (Eq. (3.3)).

To estimate the plume area variation using Eq. (4.6) and (4.7), the only term that is not determined is the plume depth at the Fraser mouth (D). This depth D may affect our model in two aspects. First, D determines the plume volume (V_{p}). At a fixed rate of volume input, the larger the exiting V_{p} is, the smaller percentage of variation it shows. Second, D determines the correction factor γ for the estimation of S_{p} and dS_{p}/dt ($\gamma = \bar{D}/[2(\bar{D} - z_0)]$

[9] As indicated in the List of Symbols, adding (t) after a parameter refers to the hourly or minute-by-minute-resolution ("minutely") variation of this parameter, in which tidal variability is important. When an overline bar is added on top of a parameter (e.g., $\bar{Q}$), it refers to the daily average of this parameter. In this case, it may still show seasonal variations, but no tidal variation is considered. The same notation applies to w_{e}, A, $w_{\mathrm{e}}A$, S_{p}, and S_{o}.

from Sec. 3.5, where $z_0 = 1$ m and $\bar{D} = D/3$ for our "semi-cone" plume model), which subsequently affects the both term 1 and term 2 in $w_e A$ (Eq. (4.5)). For term 1, when D is smaller, γ is larger, and then the magnitude of dS_p/dt variation is larger. For both terms, γ also affects the value of S_p, however, in terms of the tidal variation, this affect is considered to be relatively small.

As far as the scope of the equations, the value of D could affect our model results in sophisticated ways, and a correct estimation of D is important. In practice, the actual "plume depth" could be as large as 18 m in high-flow periods due to hydraulic controls and salt wedge dynamics (MacDonald and Geyer, 2004), but such depths may not provide a good model for the rest of the plume under a linear variation model. After a careful investigation, we find that D from 10 to 14 m gives good simulation in the tidal variation of the plume area.

The other difficulty is to match the phase difference between the model and observational results. Using the original hourly river flowrate from the numerical model output, our plume area simulation always shows a delay in the phase (see Appx. A, Fig. A.1). After a series of careful investigations, we find a consistent match in phase between the model and the observation when shifting the hourly river flowrate ahead by 80 minutes in a tidal cycle.

This 80 minutes of phase difference may come from two parts. First, the barotropic numerical model (FVCOM) does not simulate the salt wedge in the lower parts of the river, and hence may overestimate the effects of friction on the phase of tide at the river mouth. Earlier observational studies show that the phase of tide at Steveston is only 5 minutes later than that from Pt. Atkinson (Thomson, 1981), however, the tidal elevation output at Steveston from FVCOM results in an averaged delay of 55 minutes to that at Pt. Atkinson. This mismatch means that, in practice, the actual tidal phase of the river flowrate at Steveston should be about 50 minutes earlier than that from the FVCOM model output.

Secondly, as introduced in Sec. 1.2, the main arm of the Fraser River extends 9 km offshore from Steveston to Sand Heads through a region of mudflats. Since the shallow mudflats are partly uncovered during the low tide, Sand Heads may be a better representative of the "Fraser mouth" than Steveston. Although the tidal fluctuation of the freshwater discharge at Sand Heads is hard to derive, its phase against tide can be estimated by extrapolation. Investigations of the surface velocity along the lower Fraser from the FVCOM model (not shown in this thesis) suggest that the tidal phase of surface currents increases

roughly linearly upstream by about 3 minutes per kilometer. Similar increase of the phase delay upstream along the river channel is also found in Thomson (1981), which shows a rate ranging from 1.8 to 6.2 minutes per km from Steveston to New Westminster, depending on whether tides are in their spring or neap phases. Extrapolating this would suggest that the phase of flow at Sand Heads is about 30 minutes earlier than that at Steveston.

After the correction of the phase of $Q(t)$ by shifting it 80 minutes early in a tidal cycle, the result from our analytical simulation matches well with the R_{AF} and R_{C} curves (Fig. 4.2). In this case, daily averaged $w_{\mathrm{e}}A$ is around 1.49×10^4 m^3 s^{-1}(Eq. (4.5)), and F_{f} is around 1.79×10^4 m^3 s^{-1}. The Fraser River plume area increases 14.1% during the big ebb of the day, and the daily maximum of the plume area is about 1.5 hours later than the daily lower-low tide. Although the exact shape of the curve and the magnitude of the tidal variation are not perfectly reproduced, the phase and the general structure of plume area resizing match reasonably well with the observational results in Sec. 3.3 and 3.4 (Fig. 4.3c, d).

However, there still remain some tidal features unexplained by our model, especially during the end of the flooding tides (tide lag hour 5-11, and 15-17). Two possible reasons may account for this mismatch. First, the tidal variation in the plume salinity (i.e., S_{p}, dS_{p}/dt) that we use in the model may not be smooth and accurate enough. For example, in Fig. 4.3a and b, we see a strange drop in $w_{\mathrm{e}}A$ from h = 9-11 in the tidal cycle. This drop mainly comes from a drop at the same time from the term 1 in the model (blue curve in Fig. 4.3a), which originally comes from a relatively low dS_{f}/dt value at h = 10 (Fig. 3.15c1). Second, our model does not include the drop-off effects of SPM in the plume. In particular, during flood tides, the salinity of the plume water at the edge may still below the threshold (be considered as plume waters), but the suspended particles have been rapidly sinking down to the deeper ocean, which results in a faster decrease in the satellite observed plume area.

The daily averaged entrainment flux estimated from this study ($\overline{w_{\mathrm{e}}A} \sim 1.49 \times 10^4$ m^3 s^{-1}) is slightly smaller than the results from Halverson and Pawlowicz (2011), in which $w_{\mathrm{e}}A$ ranges from 1.7×10^4 m^3 s^{-1} to 2.7×10^4 m^3 s^{-1}. This difference may result from the methods used to estimate the plume area. In Halverson and Pawlowicz (2011), the plume area is characterized to be a function of $Q^{1/2}$: $A = \alpha Q^{1/2}$, where α is 11.1 ± 0.5 km^2 (m^3 s^{-1})$^{1/2}$. From this rough estimation, plume area at $Q = 3500$ m^3 s^{-1} is about 657 km^2, which is over 50% bigger than the area that we use for this case (432 km^2). In Sec. 3.1, the plume area is shown to be actually linearly correlated to the the river flowrate, and

a similar linear correlation is found in Pawlowicz et al. (2017). Therefore, we argue that the $w_e A$ in Halverson and Pawlowicz (2011) is overestimated because of incorrect plume area estimation. Dividing $w_e A$ by the plume area, the estimated entrainment velocity ($w_e \sim 2.9$ m d^{-1}) then falls nicely in the range proposed by Halverson and Pawlowicz (2011) (2.2 m d^{-1} to 4.5 m d^{-1}).

Over a tidal cycle, variations in both term 1 (dominated by dS_p/dt) and term 2 (dominated by $Q(t)$) of $w_e A$ (Eq. (4.5)) are significantly modulated by tide (Fig. 4.3). These terms vary at similar amplitudes but work in opposition to each other. Therefore, the tidal variation of $w_e A$ turns out be smaller than the variation of either of its components. However, there still remains a great deal of tidal variability in $w_e A$: it is generally bigger during ebb tides and smaller during flood tides, with a maximum daily entrainment flux about 4.7 times as big as its daily minimum. In Cordes et al. (1980), an entrainment coefficient k is estimated at the Fraser mouth under different stage of tides. This entrainment coefficient is defined as the ratio of upward entrainment velocity to the depth-averaged plume velocity ($k = w_e/|\mathbf{U}|$), and the entrainment velocity is estimated by the horizonal divergence of the surface velocity field measured by drogued drifters ($w_e = h\nabla \cdot \mathbf{U}$). The daily maximum entrainment coefficient at the big ebb ($k \sim 4.9 \times 10^{-4}$) is found to be about 4 times as big as its daily minimum at the small flood ($k \sim 1.3 \times 10^{-4}$), which is consistent with our results.

Assuming k is a constant in space over the whole plume, then w_e (and $w_e A$) must be positively correlated to the depth-averaged surface velocity $|\mathbf{U}|$. In other words, the near-field plume, in which the surface velocity is the strongest, must have a much bigger entrainment velocity than the plume region that is far away from the river mouth. This effect is shown by Kastner et al. (2018), in which paired-drifter separations are analyzed to estimate the salt flux ($S_e w_e$) at the bottom of the Fraser River plume across the isohaline with $S_e = 21$. $S_e w_e$ is the biggest at the river mouth (Sand Heads), and gradually decreases as the drifters move away. The value of $S_e w_e$ drops to near zero at 4 to 12 km away from the river mouth.

Halverson and Pawlowicz (2011) also argues that the entrainment in the plume predominantly occurs in the near-field plume and the estuarine salt-wedge, given the fact that the entrainment velocity estimated for the whole plume is at least one order of magnitude smaller than the results from some earlier observations around the Fraser mouth (e.g., Cordes et al., 1980; MacDonald and Geyer, 2004). Here in this thesis, the results agree with the discussions in Halverson and Pawlowicz (2011), and we can provide two more

pieces of evidence to show this dominance in the near-field mixing: (1) tidal variations in $w_e A$ are strongly semi-diurnal, which agrees with the dynamical feature of the "inner plume" (see Sec. 3.6). If the entrainment mainly occurs at the outer plume, more diurnal features in the $w_e A$ variation are expected, (2) the plume area only varies up to 20% over a tidal cycle, but the maximum daily $w_e A$ is about 4 to 5 times as big as its daily minimum. If the w_e is constant in both space and time, a much smaller daily variation in $w_e A$ would be expected.

4.3 Special Case Study: River Flowrate Impact on the Tide-plume Correlation and Entrainment

In the second case study, further investigations are made on the tide-plume correlation under different river flow conditions: medium-low flowrate ($\bar{Q} < 5000$ m^3 s^{-1}) and high flowrate ($\bar{Q} > 5000$ m^3 s^{-1}). For the medium-low river flowrate condition, median $\bar{Q}$ from 1685 relevant SPM images is found to be about 2750 m^3 s^{-1}, which corresponds to a plume area ($\bar{A}$) of 343 km^2. For the higher river flowrate condition, median $\bar{Q}$ for the remaining 781 images is about 6700 m^3 s^{-1}, and $\bar{A}$ is 880 km^2.

As discussed in Sec. 3.4, the magnitude of the daily averaged river flowrate ($\bar{Q}$) has significant influence on the tide-plume correlation, and the magnitude of the tidal variation in the plume area. From our analytical model, this feature is nicely reproduced (Fig. 4.4). For the low flowrate condition, $Q(t)$ is interpolated from two cases (1000 m^3 s^{-1} and 5000 m^3 s^{-1}, i.e., blue and green curves in Fig. 4.2) on to 2750 m^3 s^{-1}, with the same phase correction of 80 minutes. $D = 12$ m is again found to provide the best simulation to the observation.

For this "best simulation" result, the plume area variation matches even better with the observation than it does in the base case. Especially for the period from h = -7 to h = 6, the analytical simulation (green curve) is almost overlapped on top of the observed R_{AF} curve (red curve in Fig. 4.4b1). The magnitude of the plume area increase at the the big ebb increases from 14.1% in the base case simulation to 18.9%. On the contrary, when $\bar{Q}$ is relatively high, simulated plume area variation is always small. Although none of the D value can reproduce the exact shape of R_{AF} for this case, both observation and analytical simulations agree that the plume area is less affected by tide when the river discharge is high.

The reason for this stronger tide-plume correlation under low river flows may come from the following factors: (1), when $\bar{Q}$ is smaller, the tidal fluctuation on the river discharge is stronger, which results in a more dynamical plume, (2) the existing plume size is smaller, which reacts faster to the sinusoidal river input, (3) the river turbidity is lower and the mixing is stronger, which makes it easier for the surface SPM concentration to drop below the plume threshold, (4) when the river turbidity is lower, SPM = 2g m^{-3} may only capture the near-field plume and fail to capture the whole plume, which exaggerates the dynamical nature of the plume.

In the low flowrate condition, the mismatch between the model and the observations for the period of small ebb and small flood is still significant. In this case, the potential effect of the low dS_p/dt at h = 10 is less severe as it was in the earlier section, which left the drop-off effect of SPM to be a more important factor.

As discussed in Sec. 3.6, the Fraser River plume is horizontally characterized as a semi-diurnally modulated inner plume, and a diurnally driven outer plume. Assume that the suspended particles fall down from the plume body into the deeper ocean at a near constant speed. During the big flood of the day, plume water is pushed far away into the Strait, and its area rapidly grows nearly 20% in a few hours. In the next few hours when the river flowrate eases, the sediment carried by the plume continues to either drop down into the deeper ocean, or to be entrained out of the system at the front.

Since the Fraser River discharge at the small ebb is usually weaker than it is at the big ebb, it mainly replenishes the SPM to the inner plume region. Therefore, from h = 6 to 8 in the tidal cycle, although the rate of the volume gain in plume is already bigger than the rate of volume loss (plume area increases in the model), the suspended particles keep dropping down at the boundary region of the plume, which makes the plume "visually" decrease in size. Similarly in the small flood, the plume area decreases faster in R_{AF} curve than the model simulation, which could also be partly due to the speed of the suspended particle drop-off at the plume edges faster than the rate of entrainment from the plume to the ambient ocean.

Other than influencing the tide-plume correlation, $w_e A$ is also found to be a function of $\bar{Q}$ (Halverson and Pawlowicz, 2011). At a subtidal frequency, daily plume salinity variation is no longer considered to be an important part, thus, term 1 in Eq. (4.5) can be dropped out. Tidal variations in Q, S_o, and S_p can also be ignored. Therefore, after averaging, Eq. (4.5) can be written as:

$$\overline{w_e A} = \frac{\bar{Q}\bar{S}_p}{\bar{S}_o - \bar{S}_p} \tag{4.8}$$

Both $\bar{S}_p$ and $\bar{S}_o$ are function of $\bar{Q}$ (Fig. 4.5a). Substitute these linear regressions into Eq. (4.8), the $\overline{w_e A}$ can be estimated by any given $\bar{Q}$:

$$\overline{w_e A} = \frac{\bar{Q}(\alpha_1 \bar{Q} + \beta_1)}{(\alpha_2 - \alpha_1)\bar{Q} + (\beta_2 - \beta_1)} \tag{4.9}$$

where $\alpha_1 = -7.96 \times 10^{-4}$ $\frac{\text{k s}}{\text{kg m}^3}$, $\alpha_2 = -3.4 \times 10^{-4}$ $\frac{\text{k s}}{\text{kg m}^3}$, $\beta_1 = 23.37$ g/kg, and $\beta_2 = 26.46$ g/kg. These parameters are simply the slopes and intercepts of the linear regressions between S_p,S_o and $\bar{Q}$ (Fig. 4.5b). Since the daily averaged plume area ($\bar{A}$) is also a function of $\bar{Q}$ (using Eq. (3.3), but ignoring the small constant term and the 3-day phase delay), subtidal variation in the entrainment velocity ($\overline{w_e}$) can be expressed as:

$$\overline{w_e} = \frac{\overline{w_e A}}{\bar{A}} \sim \frac{\overline{w_e A}}{0.1361 \frac{\text{km}^2\text{s}}{\text{m}^3}\ \bar{\text{Q}}} = \frac{\alpha_1 \bar{Q} + \beta_1}{0.1361 \frac{\text{km}^2\text{s}}{\text{m}^3}\ [(\alpha_2 - \alpha_1)\bar{\text{Q}} + (\beta_2 - \beta_1)]} \times \frac{86400\,\text{s}}{\text{day}} \tag{4.10}$$

For $w_e A$, our results show a fast increase when $\bar{Q}$ is relatively low, and it stays at a near-constant level ($\sim 1.8 \times 10^4$ m^3 s^{-1}) when $\bar{Q}$ is high (Fig. 4.5b). This pattern is similar to the results in Halverson and Pawlowicz (2011), but the magnitude of our $w_e A$ estimation is 25% to 60% smaller. As discussed in Sec. 4.2, this difference mainly comes from the different ways in estimating the plume area at a given river flow condition.

Tidal fluctuations in the short-term $w_e A$ variation are found to be relatively independent of the rate of river discharge. From the 3 case studies carried out in this study, the daily minimum of $w_e A$ is found to be 0.3 to 0.5 times $\overline{w_e A}$, and the daily maximum is found to be 1.8 to 2 times $\overline{w_e A}$. The ratios of the daily maximum/minimum $w_e A$ to its daily average are then used as the upper/lower bounds of the tidal fluctuation, and these bounds are applied to the 1704 ferry track records in year 2018. The lower bound works very well in holding the lower-reach of the $w_e A$ scatter points based on each individual track, and the upper bound also does a fairly good job in limiting most of the higher points (Fig. 4.5b).

Considering w_e alone, the analysis shows a higher value (~ 4 m d^{-1}) with stronger tidal variation (± 2 m d^{-1}) when the $\bar{Q}$ is relatively low, and a lower value (~ 1 m d^{-1}) with weaker tidal variation (± 0.5 m d^{-1}) when $\bar{Q}$ is relatively high. The lower entrainment

velocity during high river discharge may due to the stronger stratification in the surface ocean.

To sum up, the river flowrate has a significant influence on the tide-plume correlation and the amplitude of daily plume area fluctuation. In addition, it also controls the rate of upward entrainment in the plume. Therefore, for any future studies on the tidal influence on the Fraser River plume, it is important to specify the river flowrate condition on which the study is based on, and carefully discuss the potential differences under high/low river discharges.

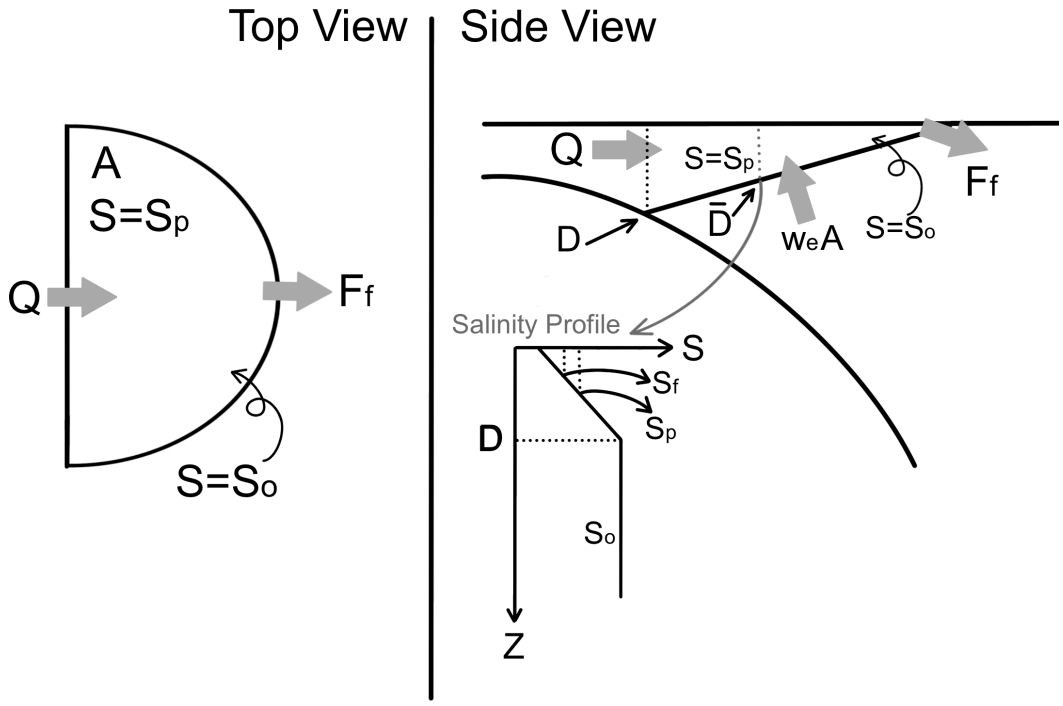

Figure 4.1: Schematic diagram of the Fraser River plume of surface area (A) and thickness at the river mouth (D). The average plume depth ($\bar{D}$) is one third of D. Q is the river flowrate, $w_e A$ is the upward entrainment rate of the bottom SoG water, and F_f is the volume flux lost at the plume front. S_f is the ferry-measured plume salinity (effective sampling depth at about 1 m), and S_p is the overall plume salinity estimated from S_f, S_o, and $\bar{D}$ (Eq. (3.12)). With respect to the salt budget, $w_e A$ brings in ambient ocean water with salinity of S_o, Q brings fresh water, and F_f exports plume water at salinity S_p.

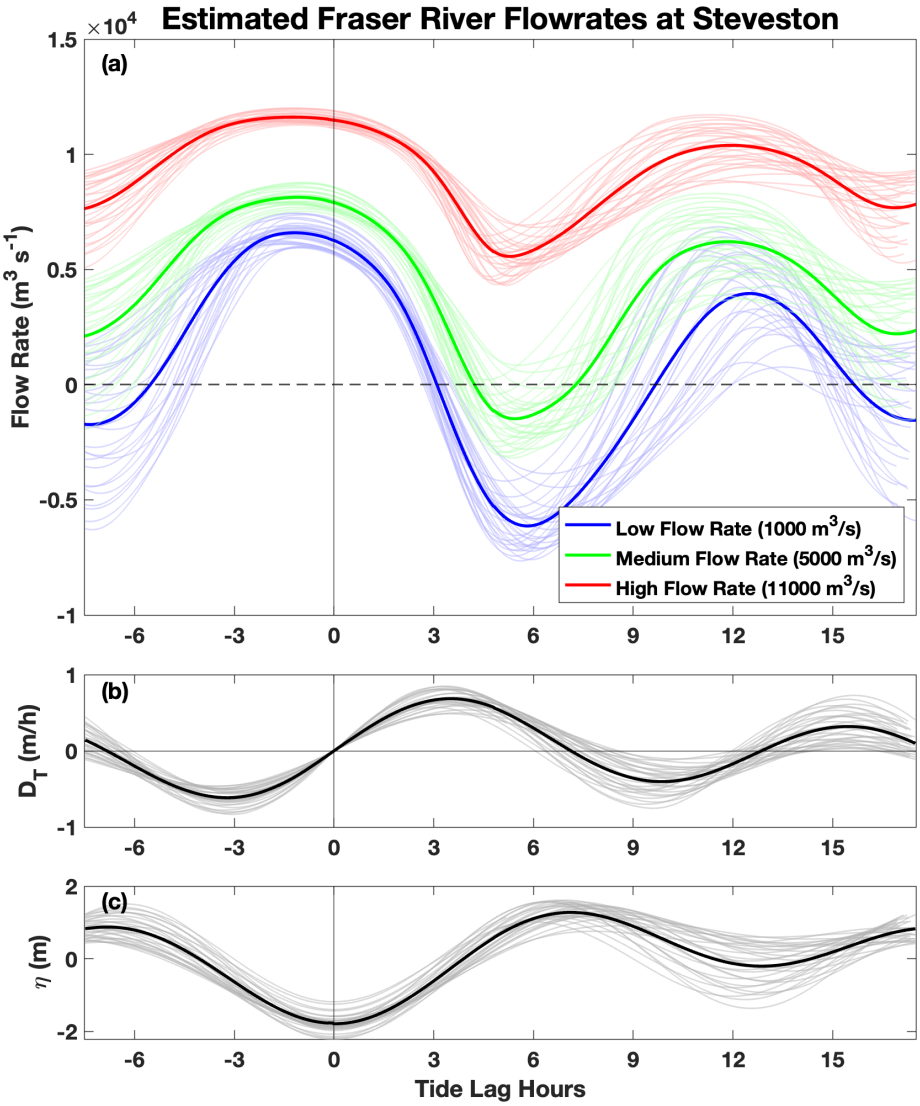

Figure 4.2: (a) River flowrate in a tidal cycle from numerical model outputs at Steveston for different river flow conditions. (b) tidal cycle of the time derivative of tidal elevation (D_{T}) at Pt. Atkinson. (c) tidal cycle of the tidal elevation (η) at Pt. Atkinson. Note that the daily averaged flowrates are not slightly smaller to the given conditions (1000, 5000, and 11000 $\mathrm{m}^3\ \mathrm{s}^{-1}$), because the main arm (at Steveston) receives about 75% to 87% of the total discharge.

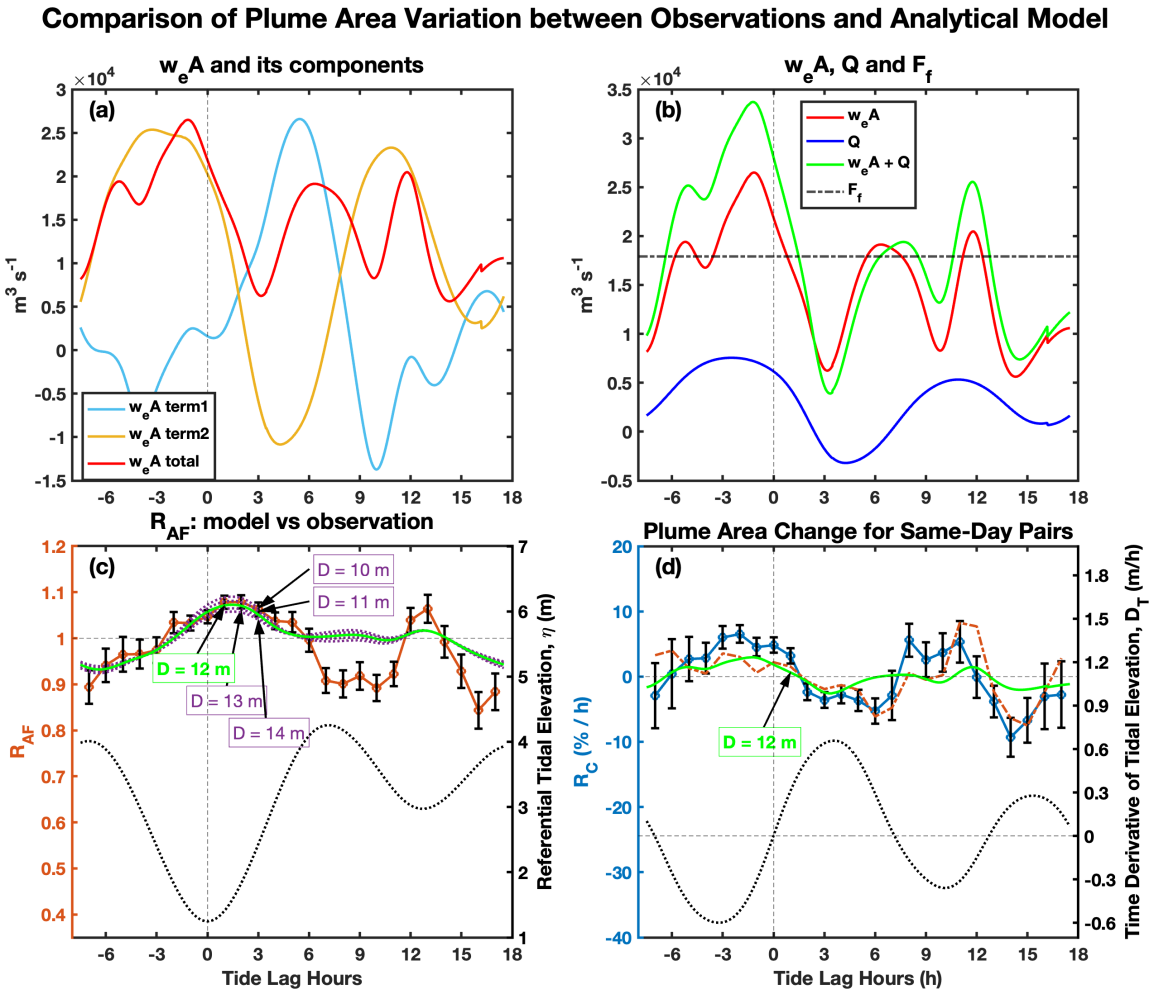

Figure 4.3: (a) tidal variation for $w_e A$ and its components (term 1 and term 2) from Eq. (4.5). (b) tidal variation for Q, $w_e A$, $Q+ w_e A$(net volume gain), and F_f (net volume loss). (c) and (d) are similar to Fig. 3.10, with the analytical solution of the plume area variation (in light green curves, at $D = 12$ m) based on Eq. (4.6) and (4.7) on top of the satellite observations. A series of sensitivity plots using $D = 10$, 11, 13, 14 m are added as dashed purple curves in (c). Note that in this case, the phase of the hourly river flowrate ($Q(t)$) is corrected by shifting 80 minutes advance in the tidal cycle.

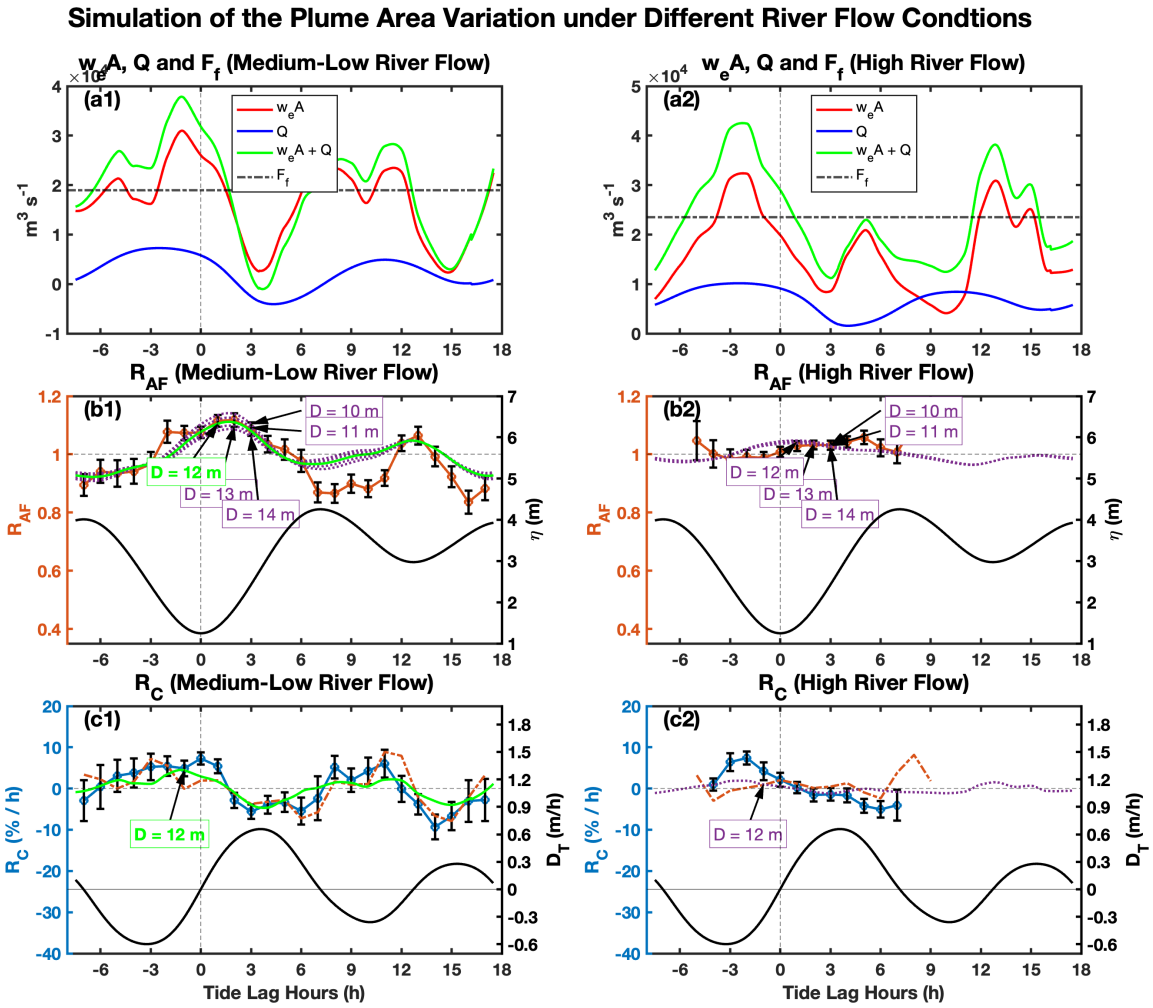

Figure 4.4: (a1) and (a2) are similar to Fig. 4.3b, but for the medium-low river flow condition ($\bar{Q} < 5000$ m^3 s^{-1}) and high river flow condition ($\bar{Q} < 5000$ m^3 s^{-1}). (b1), (b2) are similar to Fig. 4.3c, and (c1), (c2) are similar to Fig. 4.3d. In (b2) and (c2), hourly R_{AF} with less than 10 valid SPM images and hourly R_{C} with less than 3 valid same-day pairs are not shown. Solid green curves in (b1) and (c1) show the best model simulation of the plume area variation at $D = 12$ m. Dashed purple curves in (b1), (b2) and (c2) provide a series of sensitivity plots for the results from a different choice of D. Specifically in (b2) and (c2), since none of the results match with the observation, all model simulations are shown in dashed purple curves. The phase of $Q(t)$ is corrected by shifting 80 minutes advance in a tidal cycle, same as used in Fig. 4.3.

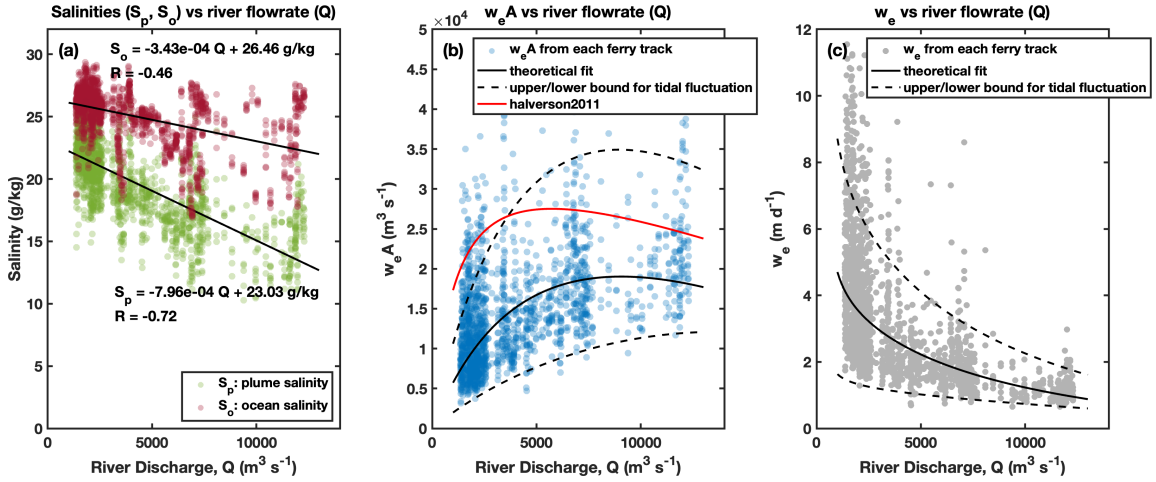

Figure 4.5: (a) linear correlations between river flowrate with plume salinity (S_p) and ambient ocean salinity (S_o). (b) Entrainment flux ($w_\mathrm{e}A$) as a function of river discharge, theoretical fit is derived in Eq. (4.9). (c) Entrainment velocity (w_e) as a function of river discharge, theoretical fit is derived in Eq. (4.10).

Chapter 5

Conclusions

Tidal influence on the Fraser River plume was investigated using two independent methods applied to a 17-year satellite observation dataset. The results consistently show a negative correlation between the tidal elevation and the plume area with a phase lag of about one hour. The plume size on average increases up to 20% during ebb tides, and decreases by a similar magnitude during flood tides. A simple analytical model based on the volume conservation and salinity balance equations was built to analyze the dynamics of the tidal influence on the Fraser River plume. Using a tidally modulated river flux and plume salinity with a correction in phase by shifting the time series 80 minutes in advance, the observed tidal variation in the plume area is partly reproduced. Tidal fluctuations in both the freshwater input and the plume salinity are important to the rapid plume resizing in tidal cycles. The rate of upward entrainment at the bottom of the plume and its tidal variations are found to be consistent with earlier studies. In addition, the horizontal structure of the plume is characterized by a semi-diurnally dominated inner plume and a diurnally controlled outer plume based on a tidal harmonic analysis on the surface currents in the southern Strait. This horizontal plume structure helps to explain some subtle variabilities in the plume salinity, and the mismatch between analytical simulation and observation at the flood tides. Lastly, river flowrate is found to be important in the tide-plume correlations. Stronger correlations and bigger amplitudes (23%) are seen in the daily tidal cycles of the plume area when the river flowrate is medium to low, while a significant correlation can not be established when the river flowrate is higher than 6000 m^3 s^{-1}.

For the first time, the magnitude of the tidal variation in a river plume area is quantitatively investigated. This 20% of the daily variation in the Fraser River plume extent can be used to characterize some high-frequency variability of the surface nutrients and productivity in the southern Strait. For monitoring purposes, this result can also be used to separate the tidal and non-tidal variations of the plume. The results can also be used to evaluate and improve numerical models (e.g., SalishSeaCast (Soontiens et al., 2016, https://salishsea.eos.ubc.ca/nemo/)), which sometimes do not accurately represent

the surface currents in the plume. Such currents are important in tracking, e.g., debris and oil spills. In particular, a similar tidal harmonic analysis in Sec. 3.5 can be applied to the model derived surface currents to see if the model can correctly represent the difference in the diurnal and semi-diurnal extents of the plume. Furthermore, a salinity threshold can be developed to define the boundary the Fraser River plume in the model outputs, and investigate the tidal variation on the plume volume, salinity, bottom entrainments, and the river flux.

This study fills in the missing gap of knowledge in the tidal variation of the Fraser River plume, and the same technique can be applied to other plume systems worldwide. As long as the plume contains sufficient amount of SPM, a threshold for the plume boundary can be easily established by a linear correlation between the SPM concentration and the surface salinity. Then, tidal variability in the plume area can then be characterized.

One important thing to be aware of for such analysis on the tidal variation is the bias in the highly aliased sampling scheme. In the case of SoG, more satellite images are taken in summer time when the sky is clear and the plume is big. At the same time, the lower-low tide also occurs in the middle of the day. Without careful debias, it will result in a false big plume during the "big ebb cycle" of the day. Not only for satellite observations, but for any observation of tidal variability, if the sampling time is at a fixed time of the day, care should be taken to investigate the potential biases.

In this study, we also show that analyzing the plume variation through the same-day image pairs is a useful and powerful technique. For research on the short-term behaviour of a dynamic water mass (i.e., the river plume), comparing these same-day images is usually a good start. In recent days, other than Aqua and Terra missions, satellites like Suomi NPP and NOAA-20 with a Visible Infrared Imaging Radiometer Suite (VIIRS) instrument, and the high-resolution Sentinel-2 products can also be used to expand the data collection and provide more same-day observations. Although the subtle differences between the images from different satellites should be carefully calibrated, observations can be dramatically improved through the inter-comparison of these satellite images.

However, there is still room for improvement to this study. First of all, SPM = 2 g m^{-3} may not be a threshold that clearly separates the plume water from the ambient ocean in all conditions. In some special cases, especially when the river flowrate and turbidity are relatively low, SPM = 1 to 1.5 g m^{-3} might be a better choice. Further investigations are needed to develop a better SPM threshold that is time dependent and can effectively capture the plume under all possible conditions.

Second, the use of the correction factor γ to adjust the ferry-measured salinity to represent the overall plume salinity may need further justification. A sufficient number of CTD profiles throughout the plume area is needed to measure the spatial distribution of the plume depth and the surface stratification to provide a better estimation of γ.

In addition, the tidal variation of the ferry-measured plume salinity and its time derivatives are not smooth, which may indicate a degree of non-tidal variation in the results. To improve the estimation of the tidal variability in the plume salinity, more advanced time series analysis tools should be applied. For example, the Lomb–Scargle periodogram can be used for this analysis, and the magnitude of diurnal/semi-diurnal influences in the plume salinity for different river flowrate conditions can be quantitatively characterized.

Other than the level of river discharge, wind direction and speed may also influence the tide-plume correlation. Theoretically, stronger winds tend to trigger stronger surface mixing, and wind-driven currents may actively change the plume shape and positions, both of which may directly or indirectly increase the short-term variability in the plume size.

At last, in this study, we recognize that the mixing and entrainment of the plume primarily occurs in the near-field plume and the estuarine salt wedge, however, it is still not known which portion is more important. To quantitatively analyze the percentage of salt-wedge entrainment to the whole plume entrainment, a long-term high-resolution time series of the river salinity is crucial. Ideally, a water buoy at Sand Heads with temperature and conductivity sensors could offer enough data to answer this question.

Bibliography

Able, K. W., M. P. Fahay, et al. (1998). *The first year in the life of estuarine fishes in the Middle Atlantic Bight*, Volume 342. Rutgers University Press New Brunswick, New Jersey.

Chant, R. (2012). Interactions between estuaries and coasts: River plumes-their formation, transport, and dispersal. In *Water and Fine Sediment Circulation*, pp. 213–235. Elsevier Inc.

Chen, S.-N. (2014). Enhancement of alongshore freshwater transport in surface-advected river plumes by tides. *Journal of Physical Oceanography 44*(11), 2951–2971.

Chen, Z., W. Gong, H. Cai, Y. Chen, and H. Zhang (2017). Dispersal of the Pearl River plume over continental shelf in summer. *Estuarine, Coastal and Shelf Science 194*, 252–262.

Chen, Z., C. Hu, and F. Muller-Karger (2007). Monitoring turbidity in Tampa Bay using MODIS/Aqua 250-m imagery. *Remote sensing of Environment 109*(2), 207–220.

Cordes, R., S. Pond, B. de Lange Boom, P. LeBlond, and P. Crean (1980). Estimates of entrainment in the Fraser River plume, British Columbia. *Atmosphere-Ocean 18*(1), 15–26.

Crean, P., T. S. Murty, and J. Stronach (1988). *Mathematical modelling of tides and estuarine circulation: The coastal seas of southern British Columbia and Washington state*, Volume 30. John Wiley & Sons, Incorporated.

Doxaran, D., J.-M. Froidefond, P. Castaing, and M. Babin (2009). Dynamics of the turbidity maximum zone in a macrotidal estuary (the Gironde, France): Observations from field and MODIS satellite data. *Estuarine, Coastal and Shelf Science 81*(3), 321–332.

Fennel, K., R. Hetland, Y. Feng, and S. DiMarco (2011). A coupled physical-biological model of the Northern Gulf of Mexico shelf: model description, validation and analysis of phytoplankton variability. *Biogeosciences 8*(7), 1881–1899.

Fofonova, V., S. Danilov, A. Androsov, M. Janout, M. Bauer, P. Overduin, P. Itkin, and K. H. Wiltshire (2015). Impact of wind and tides on the Lena River freshwater plume dynamics in the summer season. *Ocean Dynamics 65*(7), 951–968.

Fong, D. A. and W. R. Geyer (2002). The alongshore transport of freshwater in a surface-trapped river plume. *Journal of Physical Oceanography 32*(3), 957–972.

Franks, P. and D. Anderson (1992). Alongshore transport of a toxic phytoplankton bloom in a buoyancy current: Alexandrium tamarense in the gulf of maine. *Marine Biology 112*(1), 153–164.

Gan, J., L. Li, D. Wang, and X. Guo (2009). Interaction of a river plume with coastal upwelling in the northeastern South China Sea. *Continental Shelf Research 29*(4), 728–740.

Garvine, R. W. (1995). A dynamical system for classifying buoyant coastal discharges. *Continental Shelf Research 15*(13), 1585–1596.

Gower, J. and S. King (2016). 13. coastal monitoring by buoys and satellites. *State of the physical, biological and selected fishery resources of Pacific Canadian marine ecosystems in*, 53.

Halverson, M., J. Gower, and R. Pawlowicz (2018). *Comparison of drifting buoy velocities to HF radar radial velocities from the Ocean Networks Canada Strait of Georgia 25 MHz CODAR array*. Fisheries and Oceans Canada= Pêches et océans Canada.

Halverson, M. and R. Pawlowicz (2011). Entrainment and flushing time in the Fraser River estuary and plume from a steady salt balance analysis. *Journal of Geophysical Research: Oceans 116*(C8).

Halverson, M. and R. Pawlowicz (2016). Tide, wind, and river forcing of the surface currents in the Fraser River plume. *Atmosphere-Ocean 54*(2), 131–152.

Halverson, M., R. Pawlowicz, and C. Chavanne (2017). Dependence of 25-MHz HF radar working range on near-surface conductivity, sea state, and tides. *Journal of Atmospheric and Oceanic Technology 34*(2), 447–462.

Halverson, M. J. and R. Pawlowicz (2008). Estuarine forcing of a river plume by river flow and tides. *Journal of Geophysical Research: Oceans 113*(C9).

Hedges, J. I. and R. G. Keil (1995). Sedimentary organic matter preservation: an assessment and speculative synthesis. *Marine chemistry 49*(2-3), 81–115.

Hetland, R. and T. Hsu (2013). Freshwater and sediment dispersal in large river plumes. *Biogeochemical Dynamics at Large River-Coastal Interfaces: Linkages with Global Climate Change, edited by: Bianchi, TS, Allison, MA, and Cai, W.-J., Springer, New York, USA*, 55–85.

Hetland, R. D. (2005). Relating river plume structure to vertical mixing. *Journal of Physical Oceanography 35*(9), 1667–1688.

Hinatsu, M., Y. Tsukada, H. Tomita, and A. Harashima (2003). Study on estimation of original location of water sampled through inlet set on volunteer observing ship. *Journal of Advanced Marine Science and Technology Society 9*(1), 37–46.

Horner-Devine, A. R. (2009). The bulge circulation in the Columbia River plume. *Continental Shelf Research 29*(1), 234–251.

Horner-Devine, A. R., R. D. Hetland, and D. G. MacDonald (2015). Mixing and transport in coastal river plumes. *Annual Review of Fluid Mechanics 47*, 569–594.

Horner-Devine, A. R., D. A. Jay, P. M. Orton, and E. Y. Spahn (2009). A conceptual model of the strongly tidal columbia river plume. *Journal of Marine Systems 78*(3), 460–475.

Johannessen, S., R. Macdonald, and D. Paton (2003). A sediment and organic carbon budget for the greater Strait of Georgia. *Estuarine, Coastal and Shelf Science 56*(3-4), 845–860.

Kastner, S. E., A. R. Horner-Devine, and J. Thomson (2018). The influence of wind and waves on spreading and mixing in the Fraser River plume. *Journal of Geophysical Research: Oceans 123*(9), 6818–6840.

Khlopenkov, K. V. and A. P. Trishchenko (2008). Implementation and evaluation of concurrent gradient search method for reprojection of MODIS level 1b imagery. *IEEE Transactions on Geoscience and Remote Sensing 46*(7), 2016–2027.

Kilcher, L. F. and J. D. Nash (2010). Structure and dynamics of the Columbia River tidal plume front. *Journal of Geophysical Research: Oceans 115*(C5).

Lahet, F. and D. Stramski (2010). MODIS imagery of turbid plumes in San Diego coastal waters during rainstorm events. *Remote Sensing of Environment 114*(2), 332–344.

Li, M. and Z. Rong (2012). Effects of tides on freshwater and volume transports in the Changjiang River plume. *Journal of Geophysical Research: Oceans 117*(C6).

MacDonald, D. G. and W. R. Geyer (2004). Turbulent energy production and entrainment at a highly stratified estuarine front. *Journal of Geophysical Research: Oceans 109*(C5).

McCabe, R. M., P. MacCready, and B. M. Hickey (2009). Ebb-tide dynamics and spreading of a large river plume. *Journal of Physical Oceanography 39*(11), 2839–2856.

Miller, R. L. and B. A. McKee (2004). Using MODIS Terra 250 m imagery to map concentrations of total suspended matter in coastal waters. *Remote sensing of Environment 93*(1-2), 259–266.

Morel, A. and B. Gentili (1996). Diffuse reflectance of oceanic waters. III. Implication of bidirectionality for the remote-sensing problem. *Applied optics 35*(24), 4850–4862.

Münchow, A. and R. W. Garvine (1993). Dynamical properties of a buoyancy-driven coastal current. *Journal of Geophysical Research: Oceans 98*(C11), 20063–20077.

Nechad, B., K. G. Ruddick, and Y. Park (2010). Calibration and validation of a generic multisensor algorithm for mapping of total suspended matter in turbid waters. *Remote Sensing of Environment 114*(4), 854–866.

Nehama, F. and C. Reason (2015). Modelling the Zambezi river plume. *African Journal of Marine Science 37*(4), 593–604.

O'Donnell, J. (2010). The dynamics of estuary plumes and fronts. *Contemporary issues in estuarine physics 186*, 246.

Pawlowicz, R., R. Di Costanzo, M. Halverson, E. Devred, and S. Johannessen (2017). Advection, surface area, and sediment load of the Fraser River plume under variable wind and river forcing. *Atmosphere-Ocean 55*(4-5), 293–313.

Pawlowicz, R., R. Francois, and M. Maldonado (2020). Contaminant dispersion and removal in the strait of georgia (2019). *Report on 2019 work prepared for Metro Vancouver*.

Pawlowicz, R., O. Riche, and M. Halverson (2007). The circulation and residence time of the Strait of Georgia using a simple mixing-box approach. *Atmosphere-Ocean 45*(4), 173–193.

Petus, C., G. Chust, F. Gohin, D. Doxaran, J.-M. Froidefond, and Y. Sagarminaga (2010). Estimating turbidity and total suspended matter in the Adour River plume (South Bay of Biscay) using MODIS 250-m imagery. *Continental Shelf Research 30*(5), 379–392.

Rabalais, N. N., R. E. Turner, and W. J. Wiseman Jr (2002). Gulf of Mexico hypoxia, aka "the dead zone". *Annual Review of ecology and Systematics 33*(1), 235–263.

Rijnsburger, S., R. P. Flores, J. D. Pietrzak, A. R. Horner-Devine, and A. J. Souza (2018). The influence of tide and wind on the propagation of fronts in a shallow river plume. *Journal of Geophysical Research: Oceans 123*(8), 5426–5442.

Schiller, R., V. Kourafalou, P. Hogan, and N. Walker (2011). The dynamics of the Mississippi River plume: Impact of topography, wind and offshore forcing on the fate of plume waters. *Journal of Geophysical Research: Oceans 116*(C6).

Simpson, J. H. (1997). Physical processes in the ROFI regime. *Journal of marine systems 12*(1-4), 3–15.

Soontiens, N., S. Allen, D. Latornell, K. Le Souef, I. Machuca, J.-P. Paquin, Y. Lu, K. Thompson, and V. Korabel (2016). Storm surges in the strait of georgia simulated with a regional model. *Atmosphere-Ocean 54*(1), 1–21.

Stommel, H. and H. G. Farmer (1952). On the nature of estuarine circulation. part i (chapters 3 and 4). Technical report, WOODS HOLE OCEANOGRAPHIC INSTITUTION MA.

Thomson, R. E. (1981). *Oceanography of the British Columbia coast*, Volume 56 of *Can. Spec. Publ. Fish. Aquat. Sci.* Ottawa, Ont.: Can. Dept. of Fisheries and Oceans.

Wang, C., R. Pawlowicz, and A. R. Sastri (2019). Diurnal and seasonal variability of near-surface oxygen in the Strait of Georgia. *Journal of Geophysical Research: Oceans 124*(4), 2418–2439.

Wang, F., B. Zhou, J. Xu, L. Song, and X. Wang (2009). Application of neural network and MODIS 250m imagery for estimating suspended sediments concentration in Hangzhou Bay, China. *Environmental Geology 56*(6), 1093–1101.

Warrick, J. A., P. M. DiGiacomo, S. B. Weisberg, N. P. Nezlin, M. Mengel, B. H. Jones, J. C. Ohlmann, L. Washburn, E. J. Terrill, and K. L. Farnsworth (2007). River plume patterns and dynamics within the Southern California Bight. *Continental Shelf Research 27*(19), 2427–2448.

Warrick, J. A. and K. L. Farnsworth (2017). Coastal river plumes: collisions and coalescence. *Progress in oceanography 151*, 245–260.

Wu, Y., C. Hannah, P. Matte, M. O'Flaherty-Sproul, R. Mo, X. Wang, and P. MacAulay (2022). Tidal propagation in the lower Fraser River, British Columbia, Canada. *Estuarine, Coastal and Shelf Science 264*, 107695.

Yankovsky, A. E. and D. C. Chapman (1997). A simple theory for the fate of buoyant coastal discharges. *Journal of Physical oceanography 27*(7), 1386–1401.

Appendix A

Simulation of the plume area variation without correction in the phase of the river flowrate

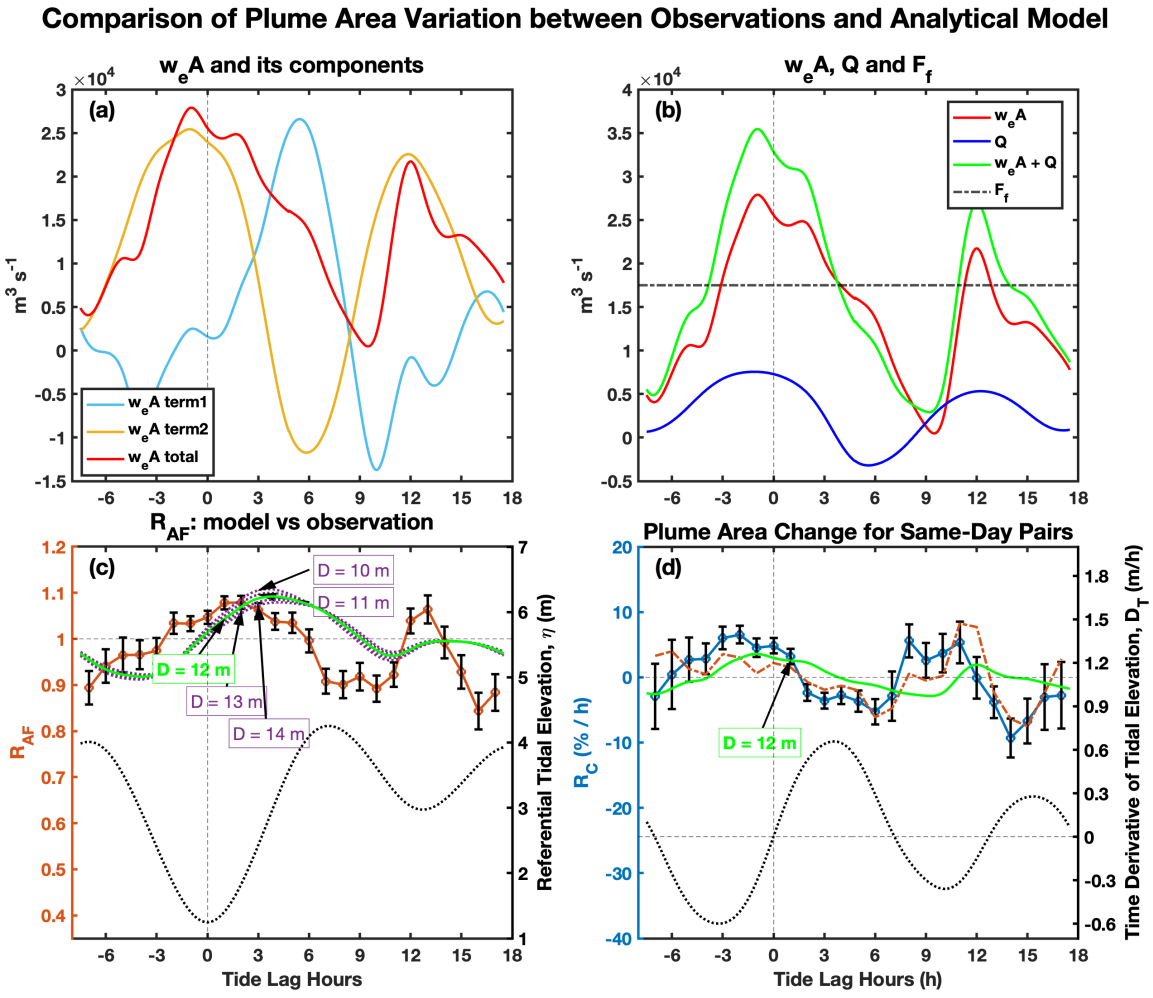

Figure A.1: Similar to Fig. 4.3 but without phase correction in $Q(t)$